Karlsruhe Institute of Technology

Korrosions- und Sorptionsprozesse an Stahloberflächen bei hohen Temperaturen und Drücken im anaeroben salinaren Milieu (KORSO)

Abschlussbericht Teilprojekt B, KIT–INE

Nicolas Finck, Nikoleta Morelová, Pelin Cakir-Wuttke, Robert Polly, Dieter Schild

INE SCIENTIFIC WORKING DOCUMENTS 03

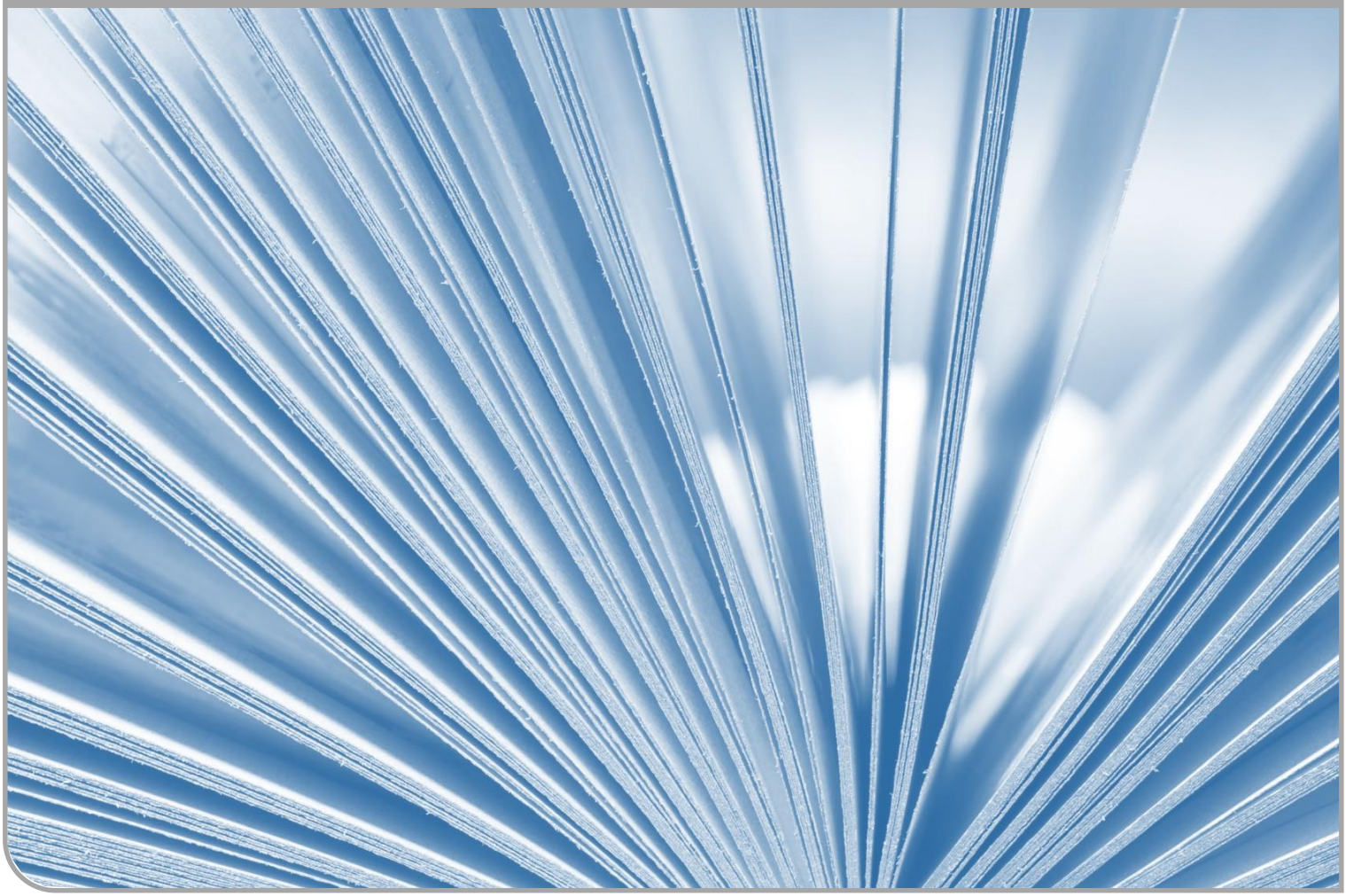

Institut für Nuklear Entsorgung (INE)

Das diesem Bericht zugrundliegende Vorhaben wurde mit Mitteln des Bundesministeriums für Wirtschaft und Energie (BMWi) unter dem Förderkennzeichen 02E11496B gefördert. Die Verantwortung für den Inhalt dieser Veröffentlichung liegt bei den Autoren.

Gefördert durch:

aufgrund eines Beschlusses
des Deutschen Bundestages

Institut für Nukleare Entsorgung (INE)

Hermann-von-Helmholtz-Platz 1
76344 Eggenstein-Leopoldshafen
www.ine.kit.edu

Impressum

Karlsruher Institut für Technologie (KIT)
www.kit.edu

2021

URL: http://www.ine.kit.edu/53.php
ISSN: 2701-262X
DOI: 10.5445/IR/1000130282

Im Rahmen dieses Abschlussberichts werden die Arbeiten zusammengefasst, die von KIT-INE unter dem Förderkennzeichen 02 E 11496B im Rahmen des Verbundprojekts KORSO (inklusive der einjährigen Verlängerungsphase) durchgeführt wurden.

Der Bericht beinhaltet:

(A) je eine deutsch- und englischsprachige Kurzzusammenfassung,

(B) den englischsprachigen Hauptteil, in dem die die Aufgabenstellung sowie der im Rahmen des Projekts erzielte wissenschaftlich/technische Fortschritt ausführlich dargestellt wird, sowie,

(C) eine Aufstellung der im Rahmen von KORSO von KIT-INE realisierten Fachpublikationen und Fachvorträge.

Inhaltsverzeichnis

A. Deutschsprachige Kurzzusammenfassung

Die von KIT-INE innerhalb des Verbundprojekts KORSO durchgeführten Arbeiten liefern ein verbessertes wissenschaftliches Verständnis des Korrosionsverhaltens von Kanistermaterialien, die in Deutschland im Rahmen der Endlagerung von radioaktivem Abfall in Salzformationen potentiell relevant sind. Der Schwerpunkt der Studie liegt auf anoxischen, hochsalinaren Bedingungen und erhöhten Temperaturen, für welche bislang kein detailliertes mechanistisches Verständnis der Korrosionsprozesse verfügbar war, schließen jedoch auch Systeme bei niedrigeren Ionenstärken ein. Die Ergebnisse bezüglich der Korrosionsmechanismen und der Korrosionsraten tragen zu einem verbesserten wissenschaftlichen Verständnis der Stabilität der Abfallkanister im Kontext der Endlagerung von radioaktiven Abfällen bei. Sie liefern grundlegende Informationen, die potentiell auch für andere Forschungsfelder, in denen eine quantitative Beschreibung der metallischen Korrosion notwendig ist, von Interesse sein können. Die Arbeiten beinhalten zudem Untersuchungen zur Rückhaltung dreiwertiger Actiniden durch Wechselwirkung mit Korrosionsprodukten (Eisen und Chrom(hydr)oxide). Die gewählten experimentellen (geo)chemischen Randbedingungen in den Arbeiten von KIT-INE umfassen wiederum verdünnte bis hochkonzentrierte wässrige Salzlösungen. Die Arbeiten wurden im Kontrollbereich des KIT-INE durchgeführt und nutzen die dort vorhandenen vielfältigen analytischen, mikroskopischen und spektroskopischen Möglichkeiten.

Im Rahmen der Arbeiten wurde eine **Literaturstudie** durchgeführt. Hierdurch ist ein Überblick über frühere Korrosionstudien, Materialien und relevante (geo)chemische Randbedingungen gegeben. Verschiedene detaillierte Studien fokussierten auf die Korrosion von Stählen in Tongesteinen, während sehr viel weniger Informationen über Korrosionsmechanismen unter den spezifischen salinaren Bedingungen verfügbar sind, die für die Endlagerung in Salzgestein potentiell relevant sind. Die Literaturstudie bestätigte, dass das Verständnis des Korrosionsverhaltens von Kanistermaterialien in salinaren Lösungen weiterer experimenteller Untersuchzungen bedurfte.

In dem Teilprojekt von KIT-INE wurden ein **Sphäroguss (SGI, GGG40)** und ein **Edelstahl (309S)**, die im deutschen Konzept der Endlagerung von radioaktivem Abfall relevant sein können, ausgewählt. Für die Korrosionsuntersuchungen wurden polierte Proben unter

anoxischen Bedingungen in verdünnte bis konzentrierte Salzlösungen eingebracht. Elektrochemische Methoden wurden verwendet, um das Korrosionspotential und Korrosionsverhalten bei Raumtemperatur in Abhängigkeit von der Ionenstärke zu bestimmen. Parallel hierzu wurden statische Experimente in geschlossenen Gefäßen, die es erlauben auch die Gasphase zu beproben, bei erhöhter Temperatur und ohne einem angelegten externen Potential oder Druck durchgeführt.

Für den **Edelstahl** zeigen die Polarisationskurven bei Raumtemperatur eine Abnahme des Korrosionspotentials mit zunehmender Konzentration der Salzlösung, sowie, bei allen Proben, die Bildung einer Passivierungsschicht. Zudem ist dieser Werkstoff anfällig für Lochfraßkorrosion, deren Wahrscheinlichkeit mit dem Salzgehalt der Lösung zunimmt. Bei Autoklavexperimenten in NaCl Lösungen konnte lediglich die Bildung einer dünnen Chrom(hydr)oxid Korrosionsschicht an der Oberfläche nachgewiesen werden. Untersuchungen mittels synchrotronbasierter Methoden an einem Probenquerschnitt konnten die Bildung einer dünnen Innenschicht aus Cr-haltigen Grünem Rost, und einer externen Trevoritschicht nachweisen. Interessanterweise bilden sich Cr haltige Phasen separat und sind nicht homogen in der Korrosionsschicht verteilt. Im Gegenteil hierzu konnte kein signifikanter Korrosionsangriff auf die untersuchten Oberflächen in 5 M NaCl Lösung festgestellt werden. In allen Experimenten, von verdünnten bis hochkonzentrierten $MgCl_2$ Lösungen, war die Oberfläche kaum angegriffen und es wurde nur eine sehr dünne Chrom(hydr)oxid Schicht festgestellt. Aus der Bestimmung des Massenverlusts der Proben in den Untersuchungen resultieren dementsprechend sehr geringe Korrosionsraten von <0.1 µm/a. Dieser Effekt erfolgte selbst über vergleichsweise lange Kontaktzeiten von fast einem Jahr hinweg, was auf einen sehr effizienten Schutz des Stahls durch die Passivierungsschicht hindeutet. In allen Experimenten lag der pH_M der Lösung zwischen 5.6 und 7.3. Das Redoxpotential lag immer oberhalb des in Polarisationsexperimenten bestimmten Korrosionspotentials, wodurch die sehr niedrige Korrosionsrate erklärt werden kann. Interessanterweise wurde in diesen statisch durchgeführten Experimenten keine Lochfraßkorrosion nachgewiesen - entweder da der Lochfraß zu gering ist, oder noch längere Kontaktzeiten für den Nachweis notwendig wären.

Der **Sphäroguss** korrodiert gleichmäßig ohne Bildung einer Passivierungsschicht. Die mittels potentiodynamischen Polarisationstests bestimmten Korrosionspotentiale bei Raumtemperatur sind niedriger als die für den Edelstahl bestimmten Werte. In allen statischen Experimenten bei

90°C fand Graphitkorrosion statt. Das Eisen in Nachbarschaft zu den Inklusionen wurde aufgrund der Positionierung der anodischen (Eisen) und kathodischen (Graphit) Stellen bevorzugt korrodiert. Die Art der gebildeten Sekundärphasen hängt sehr von der Zusammensetzung der kontaktierenden Lösung ab. In 5 M NaCl und 90°C bildet sich aufgrund des im Stahl enthaltenen Siliziums zuerst Cronstedtit (Schichtsilikat). Nach Erschöpfung des Siliziums im Material bildet sich Magnetit, während sich Eisenhydroxychlorid nahe an der korrodierenden Oberfläche bildet. In derselben Lösung aber bei 25°C bildet sich Grüner Rost mit geringen Mengen an Eisenhydroxychlorid. In 0.1 M NaCl bilden sich bei 90°C sowohl Cronstedtit als auch Magnetit, jedoch kein Eisenhydroxychlorid. In hochkonzentrierten $MgCl_2$ Lösungen und 90°C bildet sich an der korrodierenden Oberfläche FeO, welches von Eisenhydroxychlorid überdeckt wird, wogegen sich bei 25°C nur Eisenhydroxychlorid bildet. In verdünnter (0.033 M) $MgCl_2$ Lösung und 25°C bilden sich Cronstedtit und Magnetit, was dem Verhalten in verdünnter NaCl Lösung entspricht. Der Umfang der beobachteten gleichmäßigen Korrosion wird höchstwahrscheinlich über den pH_M gesteuert. In 5 M NaCl stieg bei 90°C der pH_M auf ~9 und bei 25°C auf pH_M ~7. Die Korrosionsraten betrugen nach 42 Wochen (90°C) ~1 µm bzw. nach 49 Wochen (25°C). In Systemen, in denen der pH_M lediglich im Bereich 5-6 lag (z.B. 0.1 M NaCl bei 90°C), ist die Korrosionsrate entsprechend höher (10 µm/a). In $MgCl_2$-Systemen bei 90°C und $pH_M < 7$ sind hohe Raten gefunden worden. In 3.4 M $MgCl_2$ bei 90°C und pH_M ~8.6 liegt die Rate bei ~1 µm/a. In allen Experimenten mit diesem Stahl haben sich reduzierende Bedingungen in Lösung als Folge der Stahlkorrosion entwickelt. Der Korrosionsmechanismus korreliert mit der Zusammensetzung der Lösung während die Korrosionrate primär mit dem pH_M-Wert zusammenhängt.

Die **Rückhaltung dreiwertiger Actiniden durch relevante Eisenkorrosionsproduckte** unter anoxischen Bedingungen und bei Raumtemperatur wurde in Batchexperimenten für verdünnte bis hochkonzentrierte Salzlösungen untersucht. Auf Basis der Modellierung der experimentellen Daten konnten thermodynamische Sorptionskonstanten abgeleitet werden. Die meisten Untersuchungen fokussierten auf Magnetit. Die Modellierung der potentiometrischen Titrationsdaten für diese Phase haben Information zum Ladungsverhalten an der Grenzfläche mit der Flüssigkeit geliefert. Anhand der Ergebnisse von spektroskopischen Experimenten konnten Eu Sorptionsdaten modelliert, und ein Modell für die Rückhaltung dreiwertiger Actiniden an Magnetit in verdünnten bis hochkonzentrierten NaCl Lösungen entwickelt werden. Unter endlagerrelevanten Bedingungen ist die Sorption nahezu quantitativ und wird

kaum von der Ionenstärke beeinflusst. Es bildet sich ein tridentater Eu Oberflächenkomplex an der Magnetit (111) Ebene. Der Rückhaltung von Eu an Trevorit ($NiFe_2O_4$) ist ähnlich wie an Magnetit, was auf einen begrenzten Effekt der Anwesenheit von Ni(II) gegenüber Fe(II) hindeutet. Die Rückhaltung durch Cr_2O_3 is pH-abhängig und bei $pH_M > 7.5$ nahezu quantitativ. Aufgrund begrenzter Informationen zu Effekten der Oberflächenladung und der Struktur des Oberflächenkomplexes konnte für diese beiden Phasen lediglich ein vorläufiges Modell entwickelt werden. Adsorptionsexperimente mit grünem Rost und Eisenhydroxychlorid zeigen ebenfalls eine starke Rückhaltung von dreiwertigen Actiniden, wobei hierfür keine Modellbeschreibung entwickelt werden konnte. Dreiwertige Actiniden konnten auch in Kopräzipitationsexperimenten im Magnetitsystem in verdünnten bis hochkonzentrierten Lösungen nahezu quantitativ zurückgehalten werden. Alle im Projekt gewonnenen Ergebnisse aus Rückhaltungsexperimenten zeigen, dass die untersuchten Eisenkorrosionsprodukte für die untersuchten Radionuklide stark sorbierende Festphasen darstellen, deren Anwesenheit im Endlagernahfelds die Radionuklidmobilität deutlich beeinflussen können.

In komplementären Studien des KIT-INE wurden **theoretische Rechnungen** mit Hilfe der Dichtfunktionaltheorie (DFT) an verschiedenen Systemen durchgeführt um die experimentellen Arbeiten im Labor zu ergänzen. In einer früheren Arbeit wurde Ferrihydrit in Anwesenheit von dreiwertigem Lutetium in einer Mischung aus Goethit und Hämatit (durch Alterung) umgewandelt. Die Daten deuten auf einen bevorzugten Einbau des Lutetiums in Goethit hin. Mit DFT Rechnungen konnten im Rahmen dieses Projekts zudem strukturelle Parameter von reinen Eisen(hydr)oxiden erstmals sehr genau reproduziert werden, was die Qualität der Rechnungen bestätigt. In einem weiteren Schritt wurden Parameter für Festphasenstrukturen erhalten in denen ein dreiwertiges Eisenatom durch ein dreiwertiges Lanthanid/Actinid ersetzt ist. Wiederum stimmen die theoretischen Rechnungen sehr gut mit den experimentellen Daten überein. In einem weiteren untersuchten System konnte DFT zeigen, dass der gekoppelte Ersatz von Fe(II) und Fe(III) in Magnetit durch U(V) und eine Leerstelle für lokalen Ladungsausgleich realisiert werden kann. Die entsprechenden spektroskopischen Daten konnten sehr gut reproduziert werden. Auf Basis der Arbeiten von KIT-INE konnte DFT als zuverlässiges Werkzeug zur Ergänzung experimentelle Daten in den untersuchten Eisensystemen etabliert werden, insbesondere um weitere Einblicke in die mit den Rückhaltungsprozessen assoziierten Energien zu bekommen.

Stahl in Kontakt mit Bentonit wurde unter anoxischen Bedingungen und erhöhter Temperatur kontaktiert und korrodiert, um Effekte des umgebenden geochemischen Mediums auf die Korrosionsprozesse für beide in diesem Projekt analysierten Stähle zu untersuchen. Die Oberfläche des Edelstahls war nach den Experimenten kaum angegriffen, lediglich eine sehr dünne Passivierungsschicht wurde ausgebildet. Hingegen wurde die Oberfläche des Sphärogusses eindeutig angegriffen, wobei jedoch keine signifikanten Mengen an Korrosionsprodukten detektiert werden konnte. Dieses Verhalten ist möglicherweise dadurch zu erklären, dass das Eisen in den Bentonit hineindiffundiert. In keinem der durchgeführten Experimente konnte mittels Infrarotspektroskopie eine signifikante Änderung des Bentonits festgestellt werden. Allerdings zeigten XRD Diffraktogramme eine Abnahme des Schichtabstands des Smektits, was auf eine Zunahme der Schichtladung hindeutet. Die Ergebnisse deuten auf eine ähnliche Korrosionstendenz der Stähle unter diesen Bedingungen hin wie im Kontakt mit Salzlösungen. Eine weiterführende Analyse der Korrosionsprozesse bedarf zusätzlicher Studien.

B. Executive summary

The work performed by KIT-INE within KORSO is providing improved scientific understanding on the corrosion behavior of steels relevant for the disposal of nuclear waste under highly saline conditions. Studies focused on anoxic conditions, elevated temperature and concentrated brine systems, conditions for which no detailed corrosion mechanism is available, but also included systems at lower ionic strength. The provided information on corrosion rate and mechanism contributes to an improve scientific understanding of the stability of waste containers in the context of the nuclear waste disposal Safety Case, and other fields of environmental concerns where a quantitative description of the corrosion behavior of steel is required. The work also includes investigations on the retention of trivalent actinides by secondary phases detected in corrosion experiments (iron and chromium (hydr)oxides). Geochemical conditions again cover from dilute solutions to concentrated salt brine systems and are representative of different potential repository concepts (e.g. crystalline, clay or salt rock). Outcomes provide relevant direct input to specific application oriented topics in the context of nuclear waste disposal.

A short **literature review** was first conducted to get insight into reported studies for various repository concepts in terms of steel type and corroding medium. Most reported detailed studies are for corrosion in clay rock, whereas much less effort has been devoted to decipher the steel corrosion behavior under highly saline conditions. This confirmed the existence of a knowledge gap regarding the corrosion behavior of steel under conditions relevant to disposal of nuclear waste in salt rock.

In the studies of KIT-INE, **spheroidal graphite iron (SGI)** and **stainless steel (309S)**, which could be relevant in the German concept of nuclear waste disposal, were selected. Experiments were performed under anoxic conditions using polished specimens to apply electrochemical techniques at room temperature and hanging experiments at 90°C in closed vessels allowing to probe the gas phase in dilute to concentrated NaCl and $MgCl_2$ brines without applying an external potential.

Polarization curves recorded for the **stainless steel** at room temperature from dilute to concentrated NaCl solutions show that a passivation layer forms at the surface of 309S and that the corrosion potential decreases with an increase in NaCl content of the brine. Furthermore, this material is susceptible to pitting corrosion, whose occurrence becomes more likely with increasing ionic strength of the brine. In autoclaves in NaCl brines, only a very thin corrosion layer consisting of chromium (hydr)oxide could be detected at the surface. Analysis of a cross cut by synchrotron-based techniques revealed the presence an inner-layer close to the surface made of green rust containing Fe and Cr, and trevorite ($NiFe_2O_4$) further away from the surface. Interestingly, Cr-bearing compounds form separately and are non-homogeneously distributed within the corrosion layer. In contrast, no significant surface attack could be detected for experiments performed in 5 M NaCl at 25°C. In dilute to concentrated $MgCl_2$ brines the surface was hardly attacked and only a thin layer of chromium (hydr)oxide could be detected. Accordingly, very low corrosion rates of <0.1 µm/a were obtained in all experiments, even for contact times up to 49 weeks, suggesting an efficient protection by the passivation layer. The pH_M of the contacting brine was in the same range in all experiments, between 5.6 and 7.3. The redox potential was always above the corrosion potential determined by electrochemistry, thereby explaining the low corrosion rates. Interestingly, no pitting corrosion could be detected in static experiments, either because pits were too small to be detected or because longer contact times would be needed to observe them.

The **spheroidal graphite iron** corrodes uniformly without formation of passivation layer or pitting. Corrosion potentials determined at room temperature by potentiodynamic polarization tests are lower than for 309S. In all experiments performed in closed vessels at 90°C, graphitic corrosion took place and iron close to inclusions was preferentially corroded due to the positioning of anodic site (iron) and cathodic site (graphite). The nature of the formed secondary phases is strongly dependent on the composition of the brine. In 5 M NaCl at 90°C, cronstedtite (sheet silicate) forms first owing to the presence of silicon within the steel then magnetite crystallizes once all silicon is consumed, while iron hydroxychloride forms close to the surface. In 0.1 M NaCl at 90°C, cronstedtite and magnetite form, but no iron hydroxychloride. In 5 M NaCl at 25°C, green rust formed with minor amounts of iron hydroxychloride. In concentrated $MgCl_2$ brine at 90°C, the corrosion layer contains FeO close to the surface, which is covered by iron hydroxychloride. Interestingly, in 0.033 M $MgCl_2$ at 25°C, cronstedtite and magnetite formed, which is similar to results obtained in dilute NaCl solution. In 3.4 M $MgCl_2$ at 25°C,

only iron hydroxychloride could be detected. Overall, the extent of uniform corrosion was likely governed by the pH_M. In 5 M NaCl, the pH_M increased to ~9 at 90°C and to ~7.1 at 25°C, and obtained corrosion rates were ~1 µm/a after 42 weeks (90°C) or 49 weeks (25°C). In contrast, in systems where pH_M was in the range 5-6 (e.g., 0.1 M NaCl at 90°C), the corrosion rate was significantly higher (10 µm/a). In $MgCl_2$ systems at 90°C where pH_M was < 7, high corrosion rates were obtained (10-26 µm/a), whereas in 3.4 M $MgCl_2$ at 90°C the corrosion rate was only ~1 µm/a at pH_M 8.6. In all experiments performed with this steel, reducing conditions developed in solution as a consequence of steel corrosion. The corrosion mechanism is sensitive to the nature of the contacting brine, and the corrosion rate to the pH_M of the system.

The **uptake of trivalent actinides** by relevant iron corrosion products under anoxic conditions at 25°C, for dilute to concentrate NaCl brines, was investigated by wet chemistry in batch type experiments and data modeling provided thermodynamic sorption constants. Most effort was devoted to the retention by magnetite. For this solid phase, modeling of potentiometric titrations provided information on the surface charging at the interface with the contacting liquid. Modeling of Eu(III) sorption data using results from spectroscopic experiments allowed to develop a model for the retention of trivalent actinides by magnetite from dilute to concentrated NaCl solutions. Under repository relevant conditions, the sorption is nearly quantitative and hardly affected by the ionic strength, and a tridentate surface complex forms at the magnetite (111) plane. The uptake by trevorite ($NiFe_2O_4$) is comparable to that by magnetite, suggesting a limited effect of presence of Ni(II) compared to Fe(II). The retention by Cr_2O_3 is pH dependent, and is nearly quantitative at pH_M > 7.5. For these two compounds, only a preliminary model could be developed due to the limited available information on the surface charging behavior and on the structure of the surface complex. Uptake experiments were also performed with green rust and iron hydroxychloride, showing strong retention of trivalent radionuclides, but no model could be derived for these systems. Furthermore, coprecipitation experiments showed that the retention is also quantitative when trivalent actinides are present during the formation of magnetite, from dilute to concentrated NaCl brines. Overall, results suggest that the investigated corrosion products are strongly sorbing solids, providing beneficial retention properties in the repository near-field.

Theoretical calculations were performed at the DFT level to complement the experimental work for various investigated systems. In an earlier study, ferrihydrite was converted in the

presence of lutetium into a mixture of hematite and goethite upon aging, and data hinted at an incorporation of Lu(III) into goethite. Using DFT calculations within this project, structural parameters obtained for pure iron (hydr)oxides (goethite, hematite) could be well reproduced, underpinning the high quality of the calculations. In a second step, structural parameters obtained for structures where one iron atom was replaced by one trivalent lanthanide/actinide in ferric compounds agree with reported experimental data. Furthermore, the corresponding energetics suggested that the incorporation in either phase occurs likewise, suggesting that the reaction pathway may be determining when both phases form concomitantly. DFT also showed that the coupled replacement of Fe(II) and Fe(III) in magnetite by U(V) and a vacancy for local charge balance operates and reported spectroscopic data could be well reproduced. Consequently, DFT has been established as a reliable tool complementing experimental data to get insight into energetics associated with the investigated retention processes.

Corrosion experiments where **steel was contacted with bentonite** under anoxic and elevated temperature conditions were performed to allow comparison of the medium on the corrosion behavior of both steels used in the project. The surface of 309S was hardly attacked, only a thin passivation layer formed. In contrast, the surface of SGI was attacked but no significant amount of corrosion products could be detected, possibly because of iron diffusion within the contacting bentonite. In all experiments, no significant change in the composition of the contacting bentonite could be detected by FTIR spectroscopy. However, XRD results revealed a decrease in basal spacing of the smectite, suggesting an increase in layer charge. Results suggest that the tendency of both steels to corrode may be comparable to that in the presence of only salt, but more effort would be needed to decipher the actual corrosion mechanisms.

C. Beschreibung der durchgeführten Arbeiten von KIT-INE innerhalb KORSO

1. Introduction and scope of the work

Deep geological disposal is considered a prime solution for the safe management of high-level nuclear waste (HLW). In such facilities, HLW confined in steel canisters is foreseen to be surrounded by various barriers. However, during the long-term evolution of the repository system, groundwater may move through the barriers and contact the canisters, which will start corroding. For a robust modelling of the corrosion of containers under repository relevant conditions, a detailed description of individual processes is required. The corrosion behavior of steels under conditions representative of disposal in clay rock has been reported in the literature. Unfortunately, only limited detailed information on metallic corrosion under conditions representative of a repository in salt rock is available so far. Yet, corrosion rates for various materials under high saline conditions have been reported, but the nature of the formed corrosion products and the nature of the reactions leading to their formation is poorly documented. Part of reported work was performed in the controlled area of KIT-INE, making use of the excellent analytical, microscopic and spectroscopic tools available at this facility.

After canister failure, the groundwater will reach the waste matrix, which will start altering or corroding and thereby mobilize radionuclides, such as the long-lived and radiotoxic actinides. Fortunately, canister corrosion results in the generation of hydrogen, which poises reducing conditions, and the formation of iron corrosion products, which may act as a chemical barrier and possibly retain radionuclides in the near-field. Iron-bearing phases such as oxides and hydroxides are strongly sorbing solids, able to efficiently scavenge actinides. However, the presence of high salt content may result in screening of the exposed mineral surfaces and thereby lower the affinity for actinides. Uptake studies need to be conducted under corresponding relevant conditions to decipher whether the ionic strength plays a role in the retention.

The first goal of this project is to perform corrosion experiments using steels relevant for the disposal of nuclear waste in Germany and to apply either electrochemical techniques at room temperature or hanging experiments in closed vessels at elevated temperature and for various contact times. An extensive characterization of corroded specimens using complementary techniques is applied to detect any evolution of the surface morphology at the steel/brine interface and to identify the nature of the neoformed product. Results obtained in this project

allowed to develop for the first time a model accounting for steel corrosion under anoxic and high saline conditions. In a second stage, the identified corrosion products are used in retention studies. Because reducing conditions may develop in a repository near-field, the uptake of trivalent actinides by surface sorption in dilute to concentrated salt solutions is investigated batch wise and the nature of the binding mode elucidated by spectroscopy. Separately, the charging behavior of the exposed surface as a function of ionic strength is determined. Macroscopic and microscopic scale information is combined to develop a model accounting for the retention of actinides by these phases under low to high salt contents. Separately, the uptake by coprecipitation is also briefly investigated. Thermodynamic data generated in this project will be made available for use in geochemical calculations of relevance in the framework of the nuclear waste Safety Case.

Finally, dedicated corrosion experiments are performed using the same materials but contacting bentonite in a short study. A detailed characterization is performed to highlight the effect of the medium on the corrosion processes.

2. State of the art

a. Basic corrosion chemistry

Corrosion is an irreversible interfacial reaction of a material with its environment, which results in consumption of the material or in dissolution into the material of a component of the environment [Heusler, 1989]. In the context of this project, corrosion involves two half-cell redox reactions at the solid (i.e., container) / liquid interface: oxidation of metallic iron (Eq. 1, anodic reaction) and reduction of water (Eq. 2, cathodic reaction). Because of local high pH, a fraction of ferrous ion can precipitate as ferrous hydroxide. Alternatively, it can migrate away from the interface, be taken up by surrounding mineral phases or can be complexed by other ligands such as for example carbonate or silicate.

$$Fe^0 \leftrightarrow Fe^{2+}_{aq} + 2e^- \quad \text{(Eq. 1)}$$

$$2H_2O + 2e^- \leftrightarrow 2(OH)^- + H_2 \quad \text{(Eq. 2)}$$

$$Fe^0 + 2H_2O \leftrightarrow Fe(OH)_2 + 2H_2 \quad \text{(Eq. 3)}$$

Both reactions must proceed at the same time and rate, but are spatially separated. This is caused by a difference in voltage at the anode and at the cathode, and this difference in potentials gives rise to electron migration. The equilibrium potential between these half-cell reactions is called *corrosion potential*. In real systems, the electrolyte usually contains various dissolved ions affecting the value of this equilibrium potential.

Various forms of corrosion can occur, depending on environmental factors. *Uniform* corrosion is characterized by an attack over the entire surface, and the locations of anode and cathode tend to move randomly. If corrosion products precipitate and are electric insulators, the corrosion rate will decrease. *Pitting* corrosion is an extremely localized attack resulting in holes in the material. It is considered to be more dangerous than uniform corrosion because it is difficult to detect and predict. Another form of localized attack is *crevice* corrosion and is usually associated with a stagnant solution on the micro-environmental level. It can occur within narrow and confined clearances such as seals, within screw threads or under deposits. Another form of attack is *intergranular* corrosion, located at grain boundaries, i.e., between grains making up the microstructure of metals and alloys. This form of corrosion is usually associated with chemical segregation effects or specific phases precipitated at boundaries. *Galvanic* corrosion refers to damage induced when two dissimilar materials are coupled in a corrosive electrolyte. In that case, one metal becomes the anode and corrodes faster, while the

second becomes the cathode and corrodes slower. When a tensile stress and a corrosive environment are combined, cracking can occur and this damage is called *stress corrosion cracking*.

In the context of this project, localized corrosion is the most undesirable attack, potentially causing failure of the canister even though most of the steel surface remains intact. Such attacks are more common for alloyed steel, but may also be observed for non-alloyed steel (carbon steel) if the formed oxide layer is thick enough to act as an insulator with the formation of cracks giving ways for pitting attack.

Redox reactions are the core of corrosion processes, with the potential playing a key role in the corrosion type and the stability of the formed phases. The Nernst equation (Eq. 4) defines the relationship between the half-cell or full-cell potential of a redox couple and the standard electrode potential, temperature and activity of involved species:

$$E = E^0 + \frac{2.303 \times RT}{nF} log\left(\frac{a_{red}}{a_{ox}}\right) \quad \text{(Eq. 4)}$$

Where E is the redox potential of the given medium, E^0 is the redox potential under standard conditions, n is the number of transferred electrons, T is the absolute temperature in Kelvin, R is the ideal gas constant, F is the Faraday constant, and a_{red} and a_{ox} are the activities of the reduced and oxidized species, respectively. This equation shows that temperature plays a role in potentials and thus affects corrosion processes. Similarly, iron corrosion results in the formation of hydrogen, which poises reducing conditions and thus affects the proportions of oxidized and reduced species present in the surrounding.

b. Corrosion of steel under anaerobic and saline conditions

A lot of research has been devoted to investigate the corrosion behavior of candidate canister materials. Materials can be classified either as *corrosion allowance* or as *corrosion resistant* materials. Corrosion allowance materials comprise low-alloyed steels (e.g., fine-grained steels), spheroidal graphite iron and copper. These materials corrode uniformly with predictable rates [Kursten et al., 2004]. Copper is also know to achieve thermodynamic stability under reducing conditions [Shoesmith, 2006]. Nickel (e.g., hastelloy C4, stainless steel) and titanium (Ti) alloys are corrosion resistant materials. Under disposal conditions, they corrode at very low rate owing to the instantaneous formation of a protective adherent oxide layer, a passive surface film. Such

materials should prove the absence of localized corrosion or at least its propagation resistance [van Iseghem, 2012].

i. Clay rock

The corrosion behavior of fine grained and carbon steel under conditions representative of clay-based repositories has been extensively studied [El Mendili et al., 2014; King et al., 2012; Necib et al., 2016; Schlegel et al., 2008, 2018], and earlier works have been summarized [Kursten et al., 2004; King, 2008]. Results showed a significant influence of the type of clay, the backfill material and the presence or not of oxygen. Interestingly, the corrosion rate decreases with time owing to the formation of a protective surface film. Typical corrosion rates are around 1-2 µm/a, while the long-term rate is significantly lower at around 0.1 µm/a [King, 2008]. Kursten et al. [2004] reported an increase in the corrosion rate of carbon steel in Boom Clay from ~2 µm/a at 16°C to ~8.5 µm/a at 170°C. Schlegel et al. [2010] reported studies using anodic activation, and observed unequally distributed corrosion compared to free corrosion, with a larger corrosion rate, but structurally similar interfaces formed in both cases.

The presence of dissolved carbonate and silicates usually resulted in the neoformation of siderite ($FeCO_3$) and "7 Å" sheet silicates (greenalite ($Fe_{2-3}Si_2O_5(OH)_4$), berthierine ($(Fe,Al,Mg)_3(Si,Al)_2O_5(OH)_4$), cronstedtite ($Fe_3(Si,Fe)_2O_5(OH)_4$)), along with magnetite. Interestingly, despite low chloride content in the contacting groundwater, the Cl-bearing phase β-$Fe_2(OH)_3Cl$ was frequently detected in *in situ* corrosion experiments, along with iron sulfide (FeS) because of the presence of pyrite in the clay rock [Schlegel et al., 2016, 2018; Necib et al., 2017]. Overall, the steel/bentonite interface is usually composed of various mineral phases forming various layers of more or less dense products. The application of complementary microscopic and spectroscopic techniques has proven to be determining in analyzing such systems using cross cut specimens. In contrast, stainless steel and Ni- and Ti-based alloys remain unaffected under comparable conditions [Gaudin et al., 2009; Kursten et al., 2004].

ii. Crystalline rock

The corrosion behavior of various materials under conditions representative of a disposal site in crystalline rock has also been investigated [e.g., Marsch et al., 1985; Kursten et al., 2004; Hung et al., 2017]. Among them, low-alloyed steels have low corrosion rates, and iron smectite and magnetite form as alteration products. However, such steel types require the use of a buffer to avoid likely microbial induced corrosion [King et al., 2016]. Countries choosing to dispose

of their waste in crystalline rock plan to cover their canister with a copper coating (e.g., Sweden) [Shoesmith, 2006; Van Iseghem, 2012]. Copper is thermodynamically stable under oxygen-free aqueous environment. However, studies showed the formation of Cu_2O during the initial aerobic period. Unfortunately, it is no longer immune in the presence of dissolved chloride or sulfide, forming corrosion products such as atacamite ($CuCl_2 \cdot 3Cu(OH)_2$) or Cu_2S, while in the presence of carbonate (e.g. present in bentonite) malachite ($Cu_2CO_3(OH)_2$) may also form. *In situ* corrosion experiments yielded a Cu corrosion rate of 3 µm/a when exposed to bentonite, while values as high as 30 to 50 µm/a have been reported for laboratory experiments when exposed to compacted bentonite/sand mixture saturated with synthetic groundwater [Kursten et al., 2004]. For carbon steel, long-term corrosion rates of 10 µm/a under elevated temperature conditions have been reported [Kursten et al., 2004], with siderite and magnetite as typical corrosion products. Under comparable geochemical conditions, corrosion rates of 0.1 µm/a were found for stainless steel 316L, which was also found resistant to stress corrosion cracking and localized corrosion.

iii. Salt rock

Because salt has a relatively high thermal conductivity, temperatures in such a repository could be higher than in crystalline or clay rock. However, the resulting thermal gradient may cause brines, present as fluid pockets, to migrate towards the containers. The extent of corrosion would then be determined by the volume and composition of the brine, and the container material [Winterle et al., 2012]. The composition of fluid inclusions in salt rock essentially varies from pure NaCl brine to $MgCl_2$ and $CaCl_2$ dominated brines. Countries such as Germany and United States of America (USA) have decades of expertise in corrosion in environment representative of salt rock [e.g., Hansen and Leigh, 2011; Kienzler, 2017a,b]. Extensive research has been performed since the early 1980s at KIT-INE (previously Kernforschungszentrum Karlsruhe), however focusing primarily on corrosion rates. Experiments were performed in the laboratory and in the field, very often at elevated temperatures and for durations up to several years [e.g., Kienzler, 2017a,b; Kursten et al., 2004; Smailos and Fiehn, 1995].

The *fine-grained steel* TStE 355 showed a strong temperature dependence and the nature of the brine on the corrosion rate was determined in the laboratory. Identified secondary phases in NaCl brines were hematite (possibly formed by oxidation during sample analysis) and magnetite, whereas in Mg-rich brines $(Fe,Mg)(OH)_2$ / $Fe(OH)_3Cl$ with traces of magnetite were

detected at 90°C and 150°C [Grambow et al., 1996]. The presence of sulfides did not significantly influence the corrosion behavior. At 90°C, determined corrosion rates reached 25 µm/a in NaCl and 56 µm/a in Mg-rich brines. At 150°C in Solution 3 (NaCl-rich, see composition below), a corrosion rate of 36 µm/a was reported and the non-uniform general corrosion resulted in the formation of magnetite and maghemite [Smailos, 1993]. In the additional presence of sulfide (6×10^{-4} M Na_2S) the corrosion rate increased to 44 µm/a. In Solution 1 ($MgCl_2$-rich, see composition below), a much higher corrosion rate was obtained (227 µm/a) and the formation of amakinite and akaganeite were detected and may be explained by the presence of limited amount of oxygen. In field studies, corrosion rates of 17 µm/a (DEBORA experiment) and <2 µm/a (BAMBUS II experiments) have been reported. These lower values determined in field experiments are likely due to the presence of lower amounts of brines contacting the specimens [Kursten et al., 2004].

Using a *low-alloyed* steel A36 (comparable to TStE 355) and WIPP brines (not too different from the ones used in experiments performed at INE) at 25°C and at pH 9.5, Wang et al. [2001] identified the formation of a non-homogeneous film of magnetite and sulfate- and chloride-bearing green rust compounds. Experiments performed in the context of the WIPP showed a strong temperature dependence on the corrosion rate for low carbon steel in Mg-rich brines, with the formation of mixed magnesium and iron hydroxychloride [Winterle at al., 2012].

The corrosion rate of *spheroidal graphite iron* (GGG 40.3) also significantly increases with temperature and depends on brine composition. It reached 25 µm/a at 150°C in NaCl, and 46 µm/a at 90°C and 91 µm/a at 170°C in $MgCl_2$. Interestingly, pits of 1.3 mm have been reported after 496 days of exposure to $MgCl_2$–rich brines at 90°C [Smailos et al., 1987]. This result can be explained by the presence of cathodic graphite inclusions promoting localized dissolution of adjacent ferrite [Hsu and Chen, 2010; King et al., 2016]. Corrosion rates of <1 µm/a were determined after 10 years of exposure at 90°C and 10°C in the Asse salt mine. These low rates can be explained by the low amount of brines contacting the specimens. The higher corrosion rate determined in Mg-rich brines can be attributed to replacement of Fe^{2+} by Mg^{2+} in ferrous hydroxide precipitating first upon iron oxidation. The presence of magnesium likely hinders the subsequent conversion to magnetite (Eq. 5), and $Fe(OH)_2$ or $(Fe,Mg)(OH)_2$ do not passivate steel as does magnetite.

$$3Fe(OH)_2 \rightarrow Fe_3O_4 + H_2 + 2H_2O \qquad \text{(Eq. 5)}$$

The *stainless steel* 309S showed high susceptibility to stress corrosion cracking and pitting, and corrosion rates lower in NaCl than in $MgCl_2$ [Kienzler, 2017b]. A similar behavior was also

observed in field experiments [Kursten et al., 2004]. This steel has a high chromium content (22-24 %), and the formation of a protective Cr_2O_3 film is the reason for the observed low corrosion rate [Ramya et al., 2010]. Iron can also be present in the passive film, and the Fe/Cr ratio increases with the applied potential [Zhang et al., 2017]. This steel additionally contains significant amounts of nickel (12-14 %), but only marginal amounts are present in the film.

The corrosion properties of other, *non-iron based alloys* were also investigated. The Ni-based Hastelloy C4 showed low corrosion rates in the range 0.05-1.2 µm/a in laboratory experiments, dependent on temperature and brine composition [Kienzler, 2017b; Kursten et al., 2004; Smailos and Fiehn, 1995]. Interestingly, this rate increased to 5-6 µm/a for surface welded Hastelloy C4 in experiments conducted for 18 months at 150°C [Smailos, 1993]. In Solution 3, the material corroded uniformly, whereas it suffered from severe pitting corrosion in Solution 1. The addition of sulfide to Solution 3 increased slightly the corrosion rate and pitting corrosion. It showed high corrosion resistance in field studies with rates below detection limit and the formation of small pits. Ti99.8-Pd is another material showing high resistance to corrosion due to the formation of protective TiO_2 [Kursten et al., 2004; Smailos and Fiehn, 1995]. However, it may be affected by hydrogen embrittlement [Winterle et al., 2012] and would be expensive to use even as only coating material.

iv. Effect of irradiation on corrosion

Non-alloyed materials are severely affected by the presence gamma rays [Kursten et al., 2004; Shoesmith and King, 1999]. Experiments were performed in the spent fuel storage pool at the KFA Jülich to investigate the effect on corrosion processes of radiolytic products formed in salt brines (e.g., H_2O_2, ClO^-). A dose rate of 1000 Gy/h corresponds to the gamma dose rate at the surface of a HLW canister while much lower rates of 10 Gy/h are relevant for thick unalloyed containers. The corrosion rate of spheroidal graphite iron at 90°C in $MgCl_2$ brines increased from 46 µm/a to 165 µm/a under a dose rate of 1000 Gy/h. Under similar field of gammy rays, the corrosion rate of the fine-grained steel TStE 355 reached 464 µm/a, while the corrosion rate of Hastelloy C4 increased to 3.5 µm/a and pits of 1 mm formed after 1 year at 90°C. In contrast, the effect on Ti99.8-Pd corrosion is negligible. Under a lower dose rate of 1-10 Gy/h, the effect on steel corrosion seems negligible.

v. Steels selected in this project

High-level waste to be disposed of in deep geological repositories (DGR) is either vitrified waste or the spent fuel itself, and each of these types has specific containers [Tholen, 2009]. Vitrified waste is typically contained in stainless steel containers, as this type of steel is required for withstanding temperature during pouring of the glass melt. In case of direct disposal of spent fuel without reprocessing, fuel assemblies are encapsulated in a non-alloyed or low-alloyed inner cask with outer spheroidal graphite iron. In this project, the corrosion properties of stainless steel ***309S*** and spheroidal graphite iron (***SGI***, GGG 40.3) were investigated. The goal was to determine the corrosion rate and mechanisms of these steels under high saline conditions.

c. Sorption processes at the mineral/water interface

Sorption processes at the mineral/water interface contribute to the retardation and retention of dissolved species. Processes can go from outer- and inner-sphere surface complexation to surface precipitation and colloid attachment, and ultimately to entrapment within the mineral phase by formation of a solid solution [Geckeis et al., 2013; Payne et al., 2013]. Surface induced redox reactions can also contribute to immobilization. Sorption processes are typically quantified by the distribution coefficient.

Spent nuclear fuel is mostly made of uranium, and minor actinides, plutonium and fission products. Plutonium is the main source of heat and radioactivity in the spent fuel, and its main isotope ^{239}Pu is long-lived ($t_{1/2}$ = 24,000 a). It can occur in various oxidation states, from highly soluble and mobile pentavalent under oxidizing conditions to poorly soluble trivalent cation under reducing conditions. Because after repository closure anoxic corrosion of metallic iron is expect to produce strongly reducing conditions and high hydrogen gas pressures, the most important long-term stable oxidation states of Pu in salt rock will be trivalent and tetravalent [Schramke et al., 2020]. Among minor actinides, americium is strongly contributing to the heat generation and radiotoxicity, and is expect to prevail as trivalent cation. Consequently, this work concentrated on the retention of trivalent actinides under anoxic and high saline conditions by relevant corrosion products identified in the corrosion experiments.

The retention of actinides by clay minerals has been investigated for decades (e.g., review in [Geckeis et al., 2013]), owing to the selection by some countries of clay rock to host a DGR. However, most studies focused on low ionic strength (*I*) conditions. Yet, since clay rock pore waters in northern Germany and in Canada may have salt content up to 4.9 *m* [Brewitz, 1980],

few studies also investigated the uptake of trivalent actinides by clay minerals in high NaCl concentrations [Schnurr et al., 2015; Vilks and Yang, 2018]. In these studies, the sorption decreased with increasing ionic strength in the low pH region. Few studies reported surface complexation modelling of experimental sorption data. For example, Schnurr et al. [2015] evaluated and modeled Eu(III) sorption by clay minerals under high NaCl concentrations. Scholze et al. [2019] and Banik et al. [2017] investigated the sorption of neptunium and Marsac et al. [2017] investigated the sorption of plutonium to clay minerals at ionic strengths up to 3 M. In these studies, a non-electrostatic surface complexation model was sufficient to describe the experimental data when applying the SIT and Pitzer approaches to calculate activity coefficients in solution. More recently, Garcia et al. [2019] used a basic Stern model combined with the Pitzer approach to describe the Eu(III) uptake by quartz up to high *I*.

Many data describing the retention of trivalent cations by iron (hydr)oxides have been reported. Possible retention mechanisms and approaches to geochemical modelling of actinides sorption with data obtained by various complexation models available in the HZDR database [HZDR, 2018] have been summarized [Geckeis et al., 2013]. Li and Kaplan [2012] have also reported an overview of sorption coefficients for actinides. Under oxic and low *I* conditions, trivalent cations sorb strongly to iron (hydr)oxides [Estes et al., 2013; Naveau et al., 2005; Stumpf et al., 2006]. Sorption of trivalent actinides to relevant corrosion phases under anoxic and high saline conditions has only been poorly investigated.

Many groups identified magnetite as potential sink for many pollutants due to its ability to reduce higher valent and usually mobile species, to lower valent and poorly mobile species. This property can be attributed to the presence of ferrous iron, which undergoes concomitant oxidation. The affinity and redox behavior of uranium in the presence of magnetite is well documented (e.g., [Huber et al., 2012; Ilton et al., 2010; Latta et al., 2011; Pidchenko et al., 2017; Yuan et al., 2015]). The retention upon interaction with magnetite of pentavalent neptunium [Nakata et al., 2002] or tetravalent thorium [Rojo et al., 2009] have also been reported. Furthermore, trivalent plutonium is strongly retained upon interaction with magnetite [Kirsch et al., 2011], while the synthesis of magnetite in the presence of pentavalent plutonium results in its reduction into trivalent oxidation state with a fraction being sorbed as tridentate surface complex and another fraction being structurally incorporated within the bulk structure [Dumas et al., 2019]. Unfortunately, only limited literature is available for the trivalent cations sorption to magnetite. In an earlier work by Catalette et al. [1998], quantitative sorption was achieved at pH > 7 for [Eu] = 2×10^{-4} M, while in a more recent study by Singh et al. [2009] it

was already achieved at pH 5.5 for a lower starting Eu concentration (2×10^{-9} M) at I = 0.1 M. Finally, Am(III) can also be structurally incorporated within magnetite by coprecipitation [Finck et al., 2016]. All these studies focused on low ionic strength, only Grambow et al. [1996] reported the interaction of uranium with magnetite under reducing and saline conditions.

Green rust (GR) compounds are members of the layered double hydroxide (LDH) family and are frequently detected in carbon steel corrosion experiments (e.g., [Refait et al., 1998; Usman et al., 2018]). Like magnetite, they are able to reduce radionuclides from higher valent to lower valent oxidation state (e.g., [Latta et al., 2015]). For example, the reduction of pentavalent to tetravalent neptunium at platelet edges upon interaction with green rust has been reported by several groups [Bach et al., 2014; Christiansen et al., 2011; Roberts et al., 2019]. Finally, the incorporation of Am(III) within green rust seems possible but the extent limited [Finck et al., 2016]. All these studies also focused on low ionic strength.

Besides the above-mentioned phases, other Fe phases frequently detected in corrosion experiments may be of interest. Ferrous hydroxychloride is one of such phases [Necib et al., 2017; Reguer et al., 2015; Schlegel et al., 2018], but hardly any sorption data for this phase has been reported. Similarly, corrosion phases may not all form as pure iron phases, but may contain other elements substituting for Fe, such as Mg or Ni. Interestingly, the sorption of Tc by nickel ferrite ($NiFe_2O_3$) has been reported by Wang et al. [2019], but no sorption data for actinides are available. Finally, Cr_2O_3 is another phase of interest as it forms instantaneously at the surface of stainless steel. Unfortunately, no sorption data for trivalent cations on this phase have been reported.

This review highlights the lack of sorption data for trivalent cations by relevant corrosion products under anoxic saline conditions. The goal of this project is to fill this gap.

d. Modelling

Pourbaix diagrams were systematically used in the corrosion part of this project to determine if the identified corrosion products are thermodynamically stable under the given experimental conditions (pH, E_h, T, I, [M]). Such diagrams are crucial to conclude whether these compounds are stable in the long-term, and may be of interest for the radionuclide sorption studies. Furthermore, the measured potentials will be compared to passivation/pitting potentials of the steels in given brines to establish the possible corrosion type and relate this to the observed corrosion damage.

i. Solubility

The thermodynamic stability of a solid phase in aqueous environment is determined by its solubility. Detailed information on solubility of a solid phase and on its calculation can found elsewhere [Morelová, 2020; Guillaumont et al., 2003].

ii. Surface complexation modeling

Surface complexation modelling was used in this project to obtain equilibrium constants for the relevant sorption reactions. The choice of the appropriate model depends on the complexity of the system and the objective of the study. In this project, the sorption of cations to mineral surfaces under high saline conditions was investigated. Since for these conditions surface charge and surface electrostatics play a significant role, an electrostatic model was selected [Lützenkirchen, 2006]. Various electrostatic models are available and differ in the treatment of the surface charge, or the number of planes and sites. In this project, charge distribution generic site or multi-site complexation triple layer models [Davies et al., 1978] were used depending on the information available on the solid phase. The general approach developed by Hiemstra and Van Riemsdijk [1996] treats the surface complexes as having a spatial charge distribution in the interfacial region over two electrostatic planes. A mineral phase (e.g., iron (hydr)oxides) in suspension usually has more than one exposed surface plane, with each having a different surface charge, and the model needs to take this into account. In this project, the Charge Distribution MUlti SIte Complexation (CD-MUSIC) model was used as it is best suited to address known complex crystal structures.

iii. Activity models

At high ionic strengths, activity coefficients must be taken into account because interactions between ions in solution are non-negligible. One method for the treatment of such interactions is the SIT (Specific Interaction Theory) approach [Ciavatta, 1980]. This method is based on the Debye-Hückel method, which is able to express the activity coefficient in dilute solutions and account for long-range electrostatic interactions. However, short-range non-electrostatic interactions also need to be taken into account at high salt contents. This is commonly done by

adding a further ionic strength dependence term [Guillaumont et al., 2003]. The validity of this model is usually limited to $I_m < 3.5\ m$ [Grenthe at al., 2013].

In concentrated salt brine solutions, the use of Pitzer formalism is recommended for thermodynamic calculations and geochemical modeling [Pitzer, 1991]. This approach identifies the effect of ionic strength depending on short-range binary interactions and interactions between ions of same charge, between charged ions and neutral species, and triple interactions. This results in a more realistic modelling of mean activity coefficients at high *I* at the cost of having a significantly larger number of parameters for calculating the activity of a given ion.

iv. Databases and software

Speciation and solubility of europium and americium species were calculated using the PhreeqC software [Parkhurst and Appelo, 1999]. Equilibrium constants for Eu and Am species were taken from Hummel et al. [2002] and Guillaumont et al. [2003], respectively. SIT and Pitzer approaches were used for activity corrections. The ThermoChimie database [Grivé et al., 2015] provided data in the SIT approach, while the Harvie-Møller-Weare database [Harvie et al., 1984] was chosen for the Pitzer approach. The ThermoChimie database provided ion interaction parameters for ionic strengths up to SIT capabilities, being constrained to low and intermediate *I*. When used, it will be referenced as [TC]. SIT parameters for Eu and Am species were provided by Neck et al. [2009]. The THEREDA database [Moog et al., 2015] was used for solubility and speciation calculations at high ionic strength in sorption studies and in surface complexation modelling. When used, it will be referenced as [TPA].

The PhreeqC software was used for temperature correction calculations on pH values and to obtain activities for all aqueous species in corrosion experiments in closed vessels, which further served as input for the Geochemist's Workbench (GWB) software (version 8.0) [Bethke, 1996; Bethke and Yeakel, 2018]. Pourbaix diagrams were obtained using the Act2 module of GWB. For low and intermediate *I*, the ThermoChimie database was used. At higher *I*, databases of PhreeqC and GWB were used, with Pitzer parameters for iron taken from various literature sources [Appelo, 2015; Millero et al., 1995; Pitzer and Mayorga, 1973; Plummer et al., 1988]. This database will be referred to as [PI]. Surface complexation modelling of titration and sorption data was done using the FITEQL2 software [Westall, 1982]. The Pitzer database [Harvie et al., 1984] with parameters from Neck et al. [2009] were used for calculations at $I >$ 0.1 M, and the Davies approach [Davies, 1962] at $I < 0.1$ M.

3. Steel corrosion under anoxic and low to high saline conditions

a. Materials and methods

i. Materials and chemicals

Two steel types which are relevant in the German concept for disposal of HLW were selected for this project. The first is a stainless steel (309S) already in use as a material to construct containers for vitrified HLW. The second is a spheroidal graphite iron (SGI) used to construct Pollux containers. The stainless steel was purchased from ThyssenKrupp, acciali Speciali Terni S.p.A. Torino (Italy). The second was purchased from Mittelrheinische Metallgießerei Heinrich Beyer GmbH & Co. KG Andernach (Germany). The composition of both steels, according to inspection certificates EN 10204 / 3.1, are shown in Table 1.

Table 1. *Chemical composition of both steel types used in the project (Bal.: balance).*

Wt%	**C**	**Mn**	**Si**	**P**	**Mg**	**Cr**	**Ni**	**Mo**	**N**	**Cu**	**Fe**
309S	0.06	1.15	0.35	0.02	-	22.45	13.17	.023	0.03	0.23	Bal.
SGI	3.46	0.29	3.39	0.04	0.05	0.04	-	-	-	0.04	Bal.

Several brines were selected to test the corrosion behavior of the steels. Saturated NaCl or $MgCl_2$ brines were first chosen. However, brines that may contact canisters in a repository in salt domes may have a more complex composition with admixed calcium, potassium and sulfate. Following recommendation of Kienzler and Loida [2001], two additional brines were selected. The list and composition of brines used in this project are indicated in Table 2. Experiments were also performed with 0.1 M NaCl and 0.033 M $MgCl_2$.

The goal of the project was a precise determination of the corrosion mechanism and rate for the selected steels. The first approach was to use electrochemical methods under anoxic and room temperature conditions. This approach allowed investigating the evolution of oxidation properties and the observation of corrosion products within relatively short times. Experiments were performed using a Gamry Interface 1010E potentiostat, and steels were cut into disc and polished with carbide paper and diamond paste. Experiments were performed under anoxic conditions in a three-electrode cell using an Ag/AgCl (sat. KCl) reference electrode and a Pt counter-electrode, while the steel disc was the working electrode. Electrolytes were deaerated

before starting the experiments and samples were cathodically cleaned at -1.2 V for 5 min. Two types of methods have been used to determine the corrosion behavior of the steels. The first method is called *potentiodynamic polarization test* allowing to determine the corrosion rate of steel in a given environment alongside with its tendency to pitting and to active dissolution [McCafferty, 2010]. The second method is *cyclic voltammetry* (CV) and was applied to follow the mechanism causing steel corrosion and the evolution of oxide formation and conversion [Elgrishi et al., 2018]. After the electrochemical applications, surface analytics such as XPS, XRD and SEM/EDX were used to determine the changes occurred at the surface as a consequence of corrosion.

Table 2. *Composition of the brines (molarities) used in corrosion experiments.*

Salt	Saturated NaCl	Solution 3	Saturated $MgCl_2$	Solution 1
NaCl	5	5	-	0.31
KCl	-	-	-	0.8
$MgCl_2 \cdot 6H_2O$	-	-	3.4	3.4
$CaCl_2 \cdot 2H_2O$	-	0.0188	-	-
Na_2SO_4	-	0.0188	-	-
K_2SO_4	-	0.015	-	-
$MgSO_4 \cdot 7H_2O$	-	0.015	-	0.15

In a second approach, autoclaves (Figure 1) were designed and constructed allowing to corrode steel specimens in contact with brines and to probe the gas phase at the end of the contact time. Reactors consisted of stainless steel body with a tantalum inner liner and underlid so that only tantalum was in contact with the liquid or gas phase during the corrosion experiments. The tightness was ensured by a fluorocarbon rubber O-ring. Tantalum was chosen as it is highly corrosion resistant and it allowed welding tubes to the lid. These tantalum tubes were fitted either with an overpressure valve to avoid excessive pressure build-up, with a manometer to follow the pressure build-up, or to a valve and a connector for sampling the gas phase. The inner volume of the autoclave was 90 mL. Each autoclave was tested for tightness before use in corrosion experiments. For corrosion experiments, two steel coupons (total exposed surface of 9.50 cm^2) per experiment were hung on Teflon stands and completely immerged in brine (48 mL). For experiments performed at 90°C, autoclaves were placed on heating plates using a design allowing to heat homogeneously from all sides.

Before use in corrosion experiments, coupons were polished as described above to have a defined starting surface roughness. Prior to filling the autoclaves, coupons were also weighted. In the Ar box, the coupons hanging on the stand were placed in the autoclave before adding the brine. No overpressure was applied.

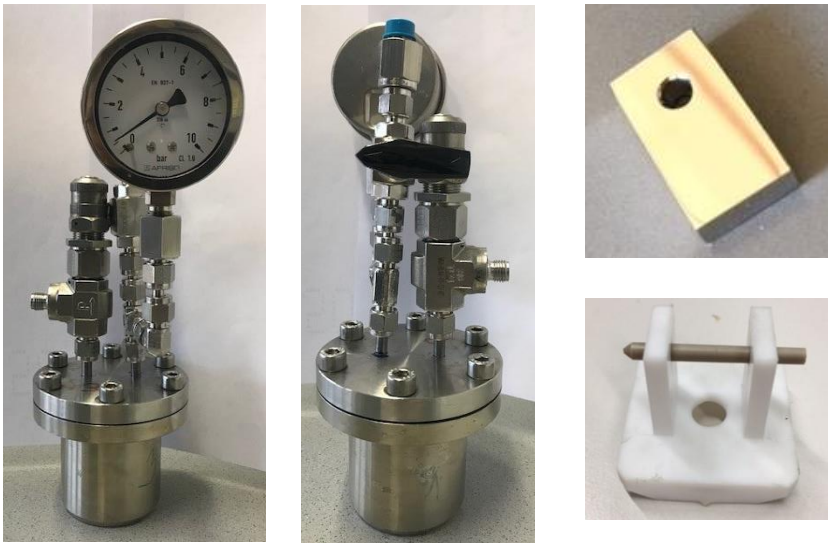

Figure 1. *Autoclave (left: front view, middle: back view) used in corrosion experiments for hanging polished steel coupons (top right) in brine using a stand (bottom right).*

pH and E_h were measured before closing the autoclaves. Because of the high salt content of the brines, experimentally measured pH values had to be corrected using an empirical correction factor [Altmaier et al., 2003, 2008] accounting for the liquid junction potential and activity coefficient of protons. In this work, indicated pH_M values refer to the measured experimental pH values, which were corrected using published empirical factors, and refer to molar proton concentrations. The value of pH_M at 90°C was recalculated using the PhreeqC software and the contents of dissolved metal ions in the brine. Depending on the system, either the [TC] database with SIT approach was used, or the [PI] database with Pitzer approach. Uncertainties on pH measured at room temperature are ± 0.05 unit, for the recalculated pH_M at 90°C the maximum uncertainty can be estimated to amount ± 0.5 unit. Finally, all E_h values reported in this work are with respect to the standard hydrogen electrode (S.H.E.). No useable empirical correction factors accounting for effects due to the high ionic strength or temperature on E_h are available. Throughout this work in autoclaves, in no cases was the potential externally forced to defined values by addition of buffer.

ii. Gas and liquid phases analysis in closed reactors

At the end of the contact time, autoclaves were allowed to cool down to room temperature before starting the analyses. In an Ar-filled glovebox a gas-sampling cylinder, which was previously evacuated to vacuum, was connected to the autoclave in order to sample the gas phase. The composition of the gas phase was determined by connecting the cylinder to a quadrupole gas mass spectrometer. The mass spectrometer was regularly calibrated using known gas mixtures. The oxygen content informed on the tightness of the setup, while the hydrogen content informed on the extent of corrosion.

After sampling the gas phase, autoclaves were opened to measure pH and E_h using appropriate electrodes at room temperature. The liquid phase was ultracentrifuged (Beckman Coulter XL-90 K) for 30 minutes at 90,000 rpm and the composition of supernatant was determined by (HR) ICP-MS (Thermo Element XR).

iii. Solid phase analysis

Prior to analysis, the corroded steel specimens were quickly washed with deionized water and blown dry to get rid of salt at the surface. Complementary microscopic and spectroscopic techniques were applied under anoxic conditions using dedicated samples holders and transfer chambers. The average surface roughness of the polished coupons before use in corrosion experiments was determined by atomic force microscopy (AFM). One coupon per steel type was analyzed exemplarily. Information on the nature of the formed corrosion phases was obtained by X-ray diffraction (XRD) using a D8 Advance (Bruker) diffractometer equipped with a Cu anode and a Sol-X or LynxExe XE-T detector. Further information was obtained by electron microscopy using an environmental scanning microscope (ESEM, Quanta 650 FEG, FEI) equipped with an energy dispersive X-ray spectroscopy detector (EDX, Thermo Scientific NORAN System 7). Complementary information was obtained by Raman spectroscopy using a Senterra Raman microscope (Bruker Optics). Information on elemental composition and chemical status was obtained by X-ray photoelectron spectroscopy (XPS, VersaProbe II, ULVAC-Phi, Al Kα). The corrosion rate was estimated using the experimentally determined weight loss following the ASTM G1-03 standard [2003]. Selected samples were embedded in resin (Buehler), cross cut and polished to allow better examination of the corrosion front.

Detailed information on the corrosion front was obtained by application of synchrotron-based techniques. Polished and cross cut samples were pre-characterized in the laboratory before

analysis by X-ray fluorescence (XRF), XRD and X-ray absorption spectroscopy (XAS) using a beam of small footprint. Steel coupons were corroded and embedded in resin as described above, then transported under anoxic conditions to CEA Saclay (Commissariat à l'Energie Atomique et aux Energies Alternatives), SEARS laboratory (Service d'Etudes Analytiques et de Reactivité des Surfaces), in France (Dr. Michel Schlegel). In an Ar box, samples were transversally cut (Minitom, Struers) with a diamond blade, and the cut was polished using a diamond containing paste. Samples were characterized by optical microscopy and selected areas were further characterized by µRaman spectroscopy and SEM-EDX. Samples were subsequently encapsulated in airtight holders (Figure 2) allowing data collection under the required geometry. Data were recorded at the DiffAbs beamline at synchrotron SOLEIL [Reguer et al., 2016]. The incoming X-ray beam had a size of approximately 5×9 µm^2 and was calibrated by assigning the first inflection point of the Fe *K*-edge XANES recorded on a Fe foil to 7112 eV. XRF maps showing the spatial distribution of Cr, Fe or Ni were obtained by selecting an excitation energy just above the *K*-edge of the element of interest: 6.2 keV for Cr, 7.2 keV for Fe and 8.4 keV for Ni. XRD patterns were recorded using a beam energy of 8.4 keV.

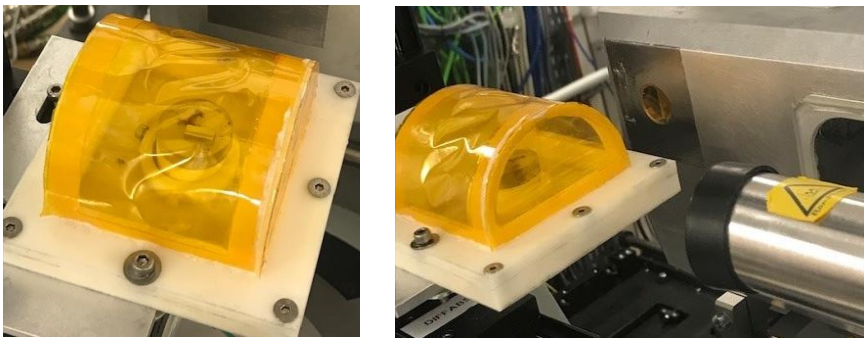

Figure 2*. Sample encapsulated in airtight holder for measurements at the synchrotron light source SOLEIL.*

b. Iron granules corrosion under anoxic, high ionic strength and elevated temperature conditions in closed vessels

Prior to investigating the corrosion behavior of steels, the corrosion behavior of iron was investigated in a preliminary set of experiments. Iron granules (fraction 2 mm in size) were contacted with brines at 60°C for periods ranging from 2 to 18 weeks. Screw capped containers

were closed in the Ar box, but they had no O-ring and were likely not completely airtight. However, outcomes provided interesting insights into iron corrosion.

The amounts of dissolved iron in NaCl brines are higher than in $MgCl_2$ brines, and in all systems they increased with the ionic strength and the contact time (Table 3). Values of dissolved iron were used to recalculate the *in situ* pH_M corrected for ionic strength effects and temperature, in the software PhreeqC with the Pitzer approach. In 1 M NaCl brine the pH_M slightly increased over 18 weeks, while in 3 M NaCl it decreased first and then increased (Figure 3). In both $MgCl_2$ brines, the pH_M deceased by 1 unit within 6 weeks before plateauing, and in 1 M $MgCl_2$ it subsequently increased. Interestingly, values recorded in $MgCl_2$ systems are lower than in NaCl systems. In all systems, the E_h decreased first then increased, except in 3 M $MgCl_2$ where it remained at ~-40 mV. These increases in second stage may be explained by a possible air intrusion with increasing contact time.

Table 3. *Dissolved amounts of Fe in granules corrosion experiments performed at 60°C. Numbers in parentheses correspond to the relative standard deviation in %.*

Contact time (weeks)	***I* = 1 M NaCl**	***I* = 3 M NaCl**	***I* = 1 M $MgCl_2$**	***I* = 9 M $MgCl_2$**
0	0	0	0	0
2	-	<0.09	-	8.76 (0.73)
6	0.137 (5.88)	0.169 (3.52)	28.33 (2.03)	33.6 (0.72)
12	<0.09	1.017 (11.55)	60.64 (0.56)	67.88 (3.31)
18	<0.09	-	82.47 (1.30)	-

In 1 M NaCl, only octahedral crystals were observed after 6 weeks of contact time (Figure 4). XPS analysis evidenced the presence of Fe(II) and Fe(III) after 6 and 12 weeks, and with EDX data findings point at the presence of magnetite. After 18 weeks, only solids of platy morphology could be seen, while EDX and XPS showed the presence of Fe(III) and an Fe:O atomic ratio of 2:3. This would suggest the presence of maghemite (γ-Fe_2O_3) or hematite (α-Fe_2O_3) as oxidation product of magnetite. Hematite crystallizes in hexagonal crystal system and is thus more likely to develop as platy crystals than cubic maghemite. The presence of pure Fe(III) compounds is consistent with the observed increase in E_h. In 3 M NaCl, octahedral and platy crystals were observed after 6 weeks of contact time and after 12 weeks, crystals of only platy morphology were seen and XPS analysis evidenced an increase in Fe(III) proportion. Results reveal a behavior comparable to that in 1 M NaCl. Interestingly, XRD analysis of the

precipitate showed the presence of maghemite as oxidation product of magnetite alongside hematite.

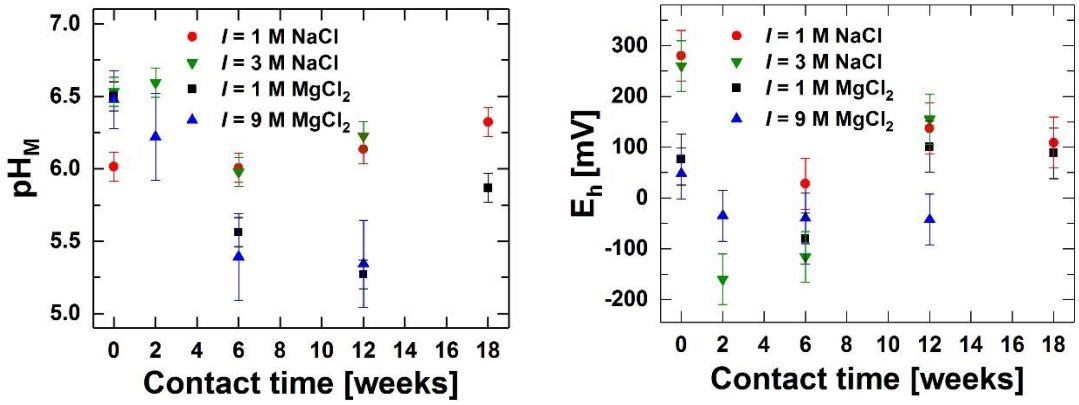

Figure 3. *pH_M (left) and E_h (right) evolutions in the granule corrosion experiments. pH_M are values corrected for ionic strength and temperature as indicated in the text.*

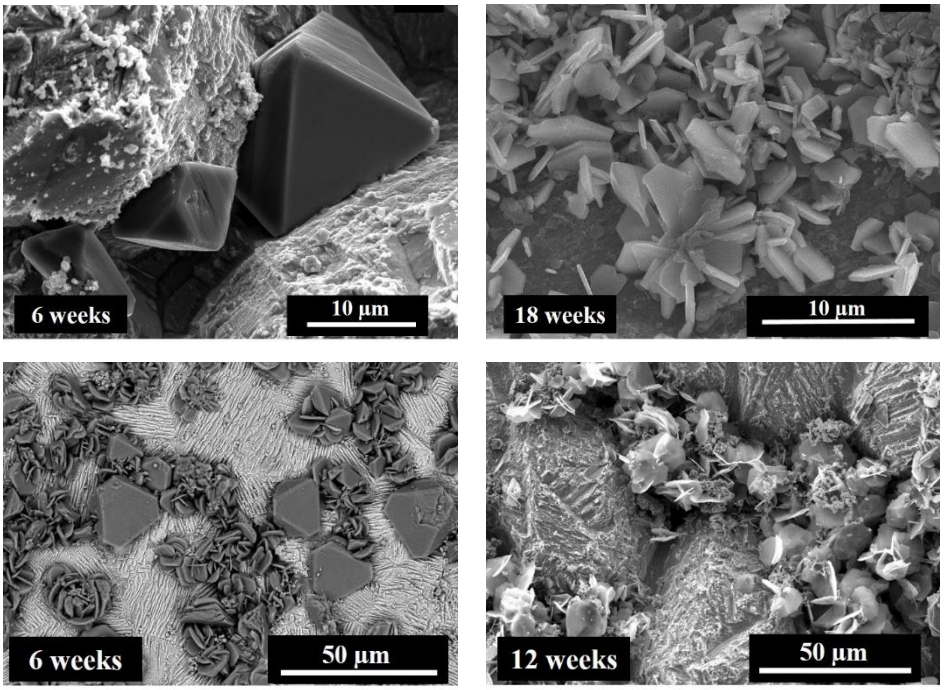

Figure 4. *Electron micrographs of granules corroded in I = 1 M NaCl (top) and in I = 3 M NaCl (bottom).*

In 1 M $MgCl_2$, octahedral crystals and compounds of platy morphology free from chloride are present (Figure 5) and XPS analysis showed the presence of Fe(II) and Fe(III). These results hint at the presence of magnetite and $Fe(OH)_2$ after 6 and 12 weeks. SEM-EDX further indicated that a fraction of Fe is substituted by Mg in platy compounds, certainly facilitated by comparable ionic sizes. For longer contact times, only compounds of platy morphology could

be seen, and XPS showed a dominant contribution of Fe(III). These findings suggest that $Fe(OH)_2$ formed first, converting into magnetite (Eq. 5), which ultimately oxidized very likely into hematite. This sequence would be consistent with observed variations in E_h. At I = 9 M $MgCl_2$ only very few crystals of platy morphology could be seen and XPS analysis showed the presence of Fe(0) and Fe(III) after 6 and 12 weeks. Unfortunately, no additional information on corrosion products could be obtained because of their low amounts. The presence of ~1 mM of dissolved Fe can be explained by the solubility of a Fe(III) solid phase, with dissolved Fe being Fe(II). In this system, the Pourbaix diagram [Morelová, 2020] suggests the presence of only $FeCl_2$ under the given experimental conditions, which is in line with experimental results.

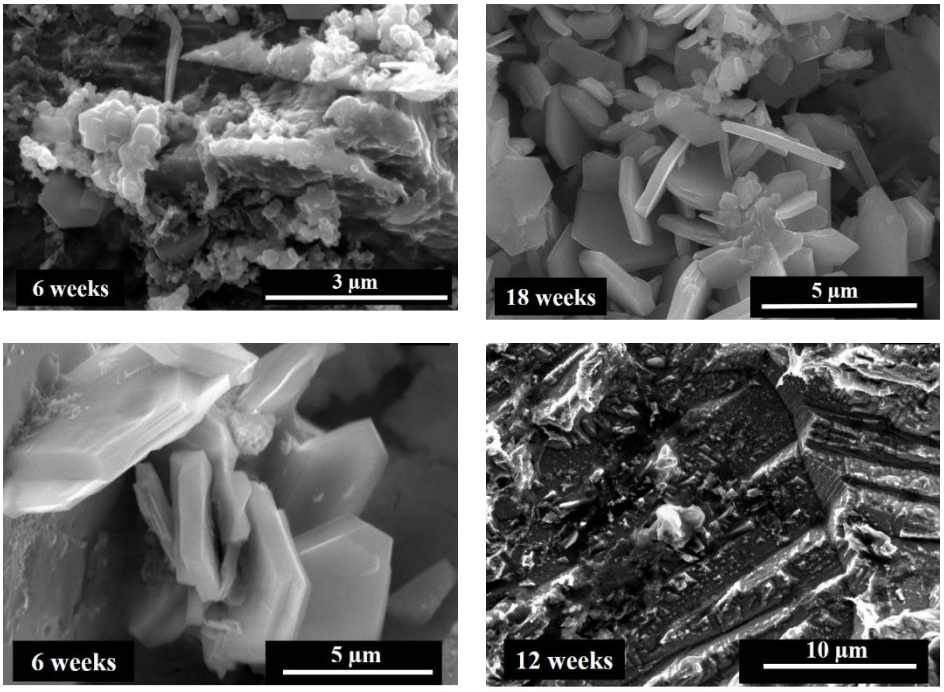

Figure 5. *Electron micrographs of granules corroded in I = 1 M $MgCl_2$ (top) and in I = 9 M $MgCl_2$ (bottom).*

This set of experiments enabled obtaining information on the corrosion mechanism of pure iron in brines at 60°C. Iron is first oxidized to ferrous ions, which in turn precipitate as $Fe(OH)_2$. This compound subsequently converts into magnetite, if pH_M and E_h are favorable ($pH_M > 5.2$; $E_h < 30$ mV). For longer contact times, air intrusion resulted in oxidation of magnetite into maghemite and hematite and E_h increased. Results further showed that under similar ionic strength (e.g., I = 1 M), the nature of the salt plays no significant role on the mechanisms.

Interestingly, no Cl-bearing phase was detected under high ionic strength conditions, only pure iron (hydr)oxides compounds.

c. Electrochemical study of steel corrosion under anoxic, high saline and room temperature conditions

i. Potentiodynamic polarization tests

Corrosion potentials (E_{corr}) were determined for both steels in NaCl and $MgCl_2$ brines by applying a potential and recording the current density. On polarization curves (Figure 6), the corrosion potential is reached when there is no current flow. If the potential is further increased, the anodic dissolution reaction takes over and positive currents are recorded. When the electrode has a tendency for passivity, the current density slows down due to the formation of an oxide film. Beyond this line, the passive film breaks down locally forming pits, and is evidenced by a horizontal line. When the passive film is thin, metastable pitting can occur.

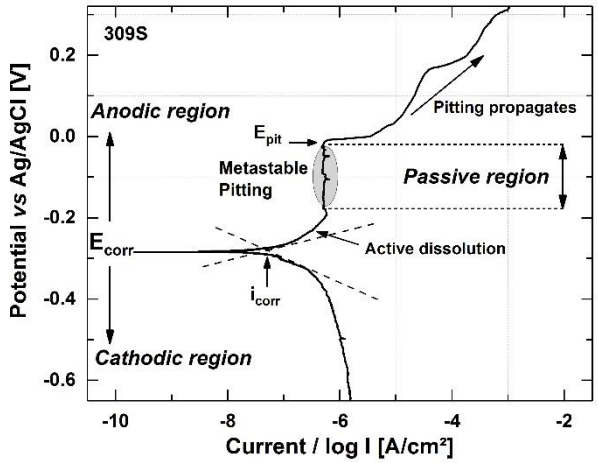

Figure 6. *Polarization curves showing the current density as a function of the applied potential for 309S in 5 M NaCl.*

For 309S, the thickness of the passivation layer increases with the ionic strength, the most stable and thick layer was obtained for 3.4 M $MgCl_2$, and no metastable pitting occurred. The pitting potential decreased with an increase in ionic strength for 309S (Figure 7), meaning that pitting occurrence is likelier, due to the high chloride content attacking the surface [Roy et al., 1996].

For SGI the corrosion potentials are lower and less affected by a change in ionic strength than for 309S. This can be explained by the absence of elements such as Cr or Ni able to form a protective oxide layer on SGI, resulting in a more uniform corrosion. XPS analysis of 309S in 5 M NaCl shows that the surface contains Fe(0), Fe(II) and Fe(III), while only trace amounts of Fe were detected inside the pit (Figure 8). This was corroborated by EDX analysis indicating an increase of chromium inside the pit (56 at. % Cr, 44 at. % Fe) compared to the surface (28 at % Cr, 72 at. % Fe).

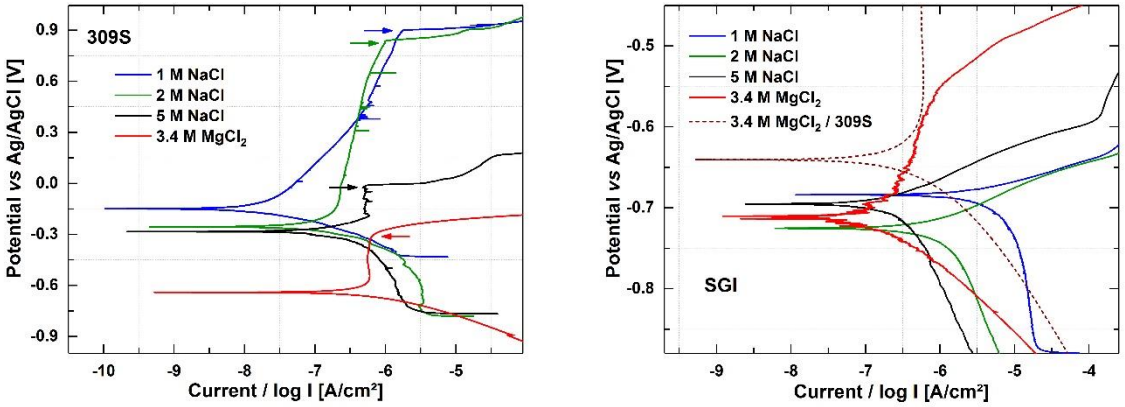

***Figure 7**. Polarization curved for 309S (left) and SGI (right) in various concentrations of NaCl and in 3.4 M NaCl. For 309S, arrows indicate pitting potentials.*

The steel corrosion resulted in the formation of a precipitate. SEM analysis revealed a layered structure, identified as $Fe(OH)_2$ by XRD. This compound is the product resulting from iron oxidation coupled to water reduction (Eq. 3). XPS analysis of the same precipitate also hinted at the presence of Fe(III). XPS is more surface sensitive than e.g. XRD, and results hint at a sensitivity of $Fe(OH)_2$ towards residual oxygen, triggering oxidation. This transformation was also noticeable on the O 1*s* narrow line showing the presence of an oxide component.

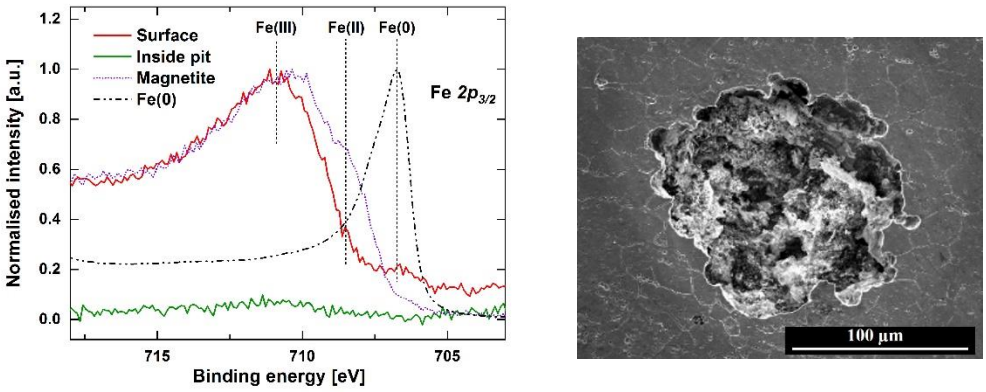

Figure 8. *Fe $2p_{3/2}$ X-ray photoelectron spectrum recorded inside and outside a pit for 309S in 5 M NaCl, and electron micrograph of the pit.*

ii. Cyclic voltammetry

Cyclic voltammetry (CV) experiments were carried out for 309S in 5 M NaCl and in 3.4 M $MgCl_2$. It can identify re-passivity and the conversion of the oxide formed on anodic scans. In the first cycle in 5 M NaCl (Figure 9), the current did first not change with increasing potential because of surface passivation, but then a strong current was observed followed by a hysteresis loop, which can be attributed to pitting. On the way back toward negative potentials, the hysteresis loop ends and the current starts to become negative. Re-passivation (E_r) occurs first at point C and the area D at lower potentials indicates the reduction of products formed during pitting.

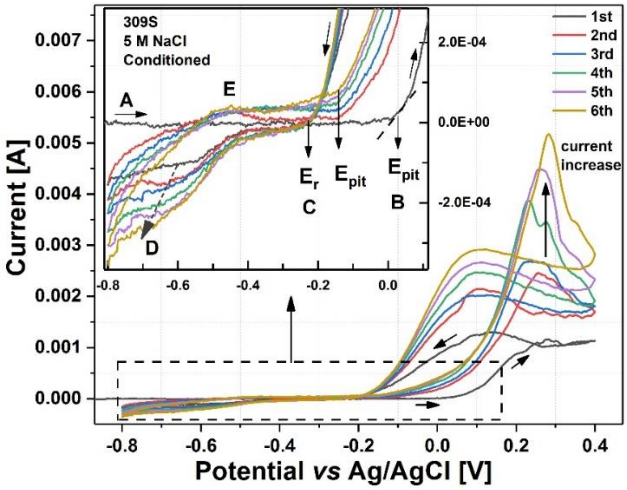

Figure 9. *Cyclic voltamogram for 309S in 5 M NaCl under anoxic and room temperature conditions.*

On the second and all following cycles, the first shallow peak appears at point E, which announces the oxidation of secondary phases produced by pitting initiated at first cycle. From this point on, each cycle D* increases in current density due to the number and sizes of pits, and consequently D on the cathodic region because of increased amount of pit products formed at point D*. Pitting starts earlier in following cycles than in the first cycle, indicating a thinner passive oxide formation at the surface and that surface defects allow a better current flow.

The same characteristics were observed in 3.4 M $MgCl_2$ (Figure 10), except the higher current density and the pit formation starting at lower potentials than in 5 M NaCl. In this brine, a thicker passive layer formed as can be observed from the very low current readings thus when pits formed, sudden high current readings were observed. This can be assumed to arise from changes in currents due to the exposure of non-passivated surface of the pits.

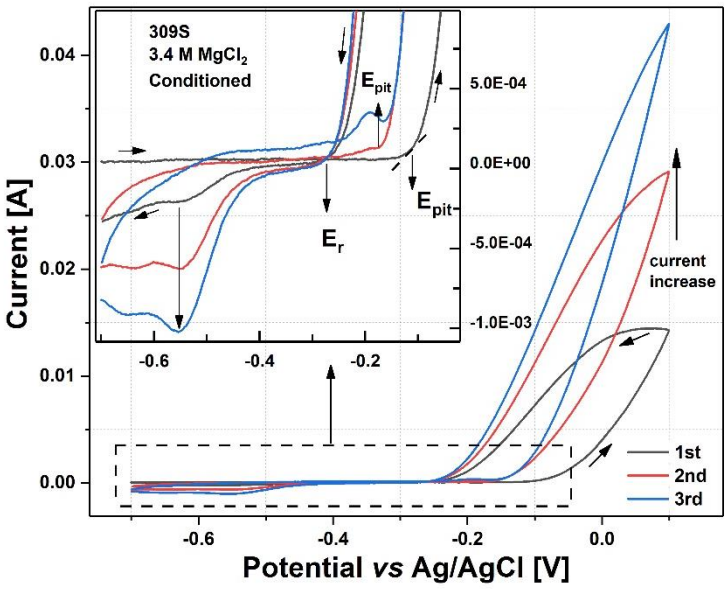

Figure 10. *Cyclic voltamogram for 309S in 3.4 M $MgCl_2$ under anoxic and room temperature conditions.*

iii. Corrosion behavior of 309S and SGI

Both steels differ in their corrosion behavior: SGI tends for active dissolution and uniform corrosion, while 309S tends for passivation and pit formation. The formation of a passive layer at the surface plays an important role as it initially slows down the corrosion rate. Even though the formation of a passive film at the surface is preferable, localized corrosion is hard to predict

[Soltis, 2015; Pradhan et al., 2019]. The occurrence of localized corrosion depends on many factors including grain size and surface roughness [Pradhan et al., 2019], and the concentration of aggressive species, such as Cl^- [Baroux, 1988; Olsson and Landolt, 2003]. Because of its small size compared to other halides it can better penetrate the oxide layer. Furthermore, increasing the chloride content decreases the time needed for a pit to form [Stolica, 1969; Broli et al., 1973; Frankel, 1998].

Potentiodynamic polarization curves for 309S showed that $\Delta E = E_{corr}-E_{pit}$ decreased with increasing Cl^- concentrations, indicating the aggressive nature of chloride anions on the localized corrosion. In lower Cl^- concentrations, metastable pits were evidenced by current fluctuations in the passive region. These metastable pits showed a sudden increase followed by a sudden decrease in current, indicating that the surface was initially passivated [Pradhan et al., 2019]. This could mean the passive layer is quite thin and cannot hold the protection initially but repairs itself and/or the Cl^- concentration is not high enough to sustain pit propagation. This explains the observation of metastable pits for lower chloride concentrations. The occurrence of re-passivation after pit formation indicates the self-repair nature of the surface. Furthermore, the re-passivation potential (E_r) is independent from the degree of pit propagation and shows reproducible values on each cycle. E_r values are within the passive potential window ($E_{corr}<E_r<E_{pit}$) and because of this, higher chromium percentages were found inside the pit than outside, as so called newly formed naked-unpolished pit areas act as anodic site and passivate immediately.

In contrast, SGI corrodes uniformly without forming a thick passive layer. In this project, E_{corr} values were not much affected by the chloride concentration, whereas Song et al. [2017] suggested that the chloride content influences the nature of formed corrosion products in soil environments.

d. Spheroidal graphite iron corrosion in dilute to concentrated NaCl and $MgCl_2$ solutions in closed reactors

The starting polished coupons were analyzed prior to use in corrosion experiments. Chemical analysis by XPS yielded an elemental composition comparable to that of the certificate, while SEM images showed the presence of carbon inclusions of ~50 µm in size. The surface roughness determined by AFM had a value of ~15 nm.

i. pH_M and E_h evolutions

pH_M values either remained stable or increased, only a slight decrease was observed for Solution 3 at 90°C (Figure 11). It is worth mentioning that an increase of ~2.5 units was observed for 5 M NaCl at 90°C, which is not surprising considering it is an unbuffered system. In all systems, the E_h decreased and reached values around -200 mV, except for the experiment performed in Solution 1. For corroding iron, the E_h of the systems should be on the lower stability line of water (~-400 mV). However, potentials could not reach such low values, and this may possibly be attributed to the escape of hydrogen. Corrosion potentials (E_{corr}) were determined by potentiodynamic polarization experiments at room temperature (see above): at pH 7 and in 5 M NaCl and in 3.4 M $MgCl_2$, values of E_{corr} in the range from -400 mV to -450 mV were obtained, respectively, close to the stability line of water. These values are significantly lower than those obtained in autoclave experiments at 90°C.

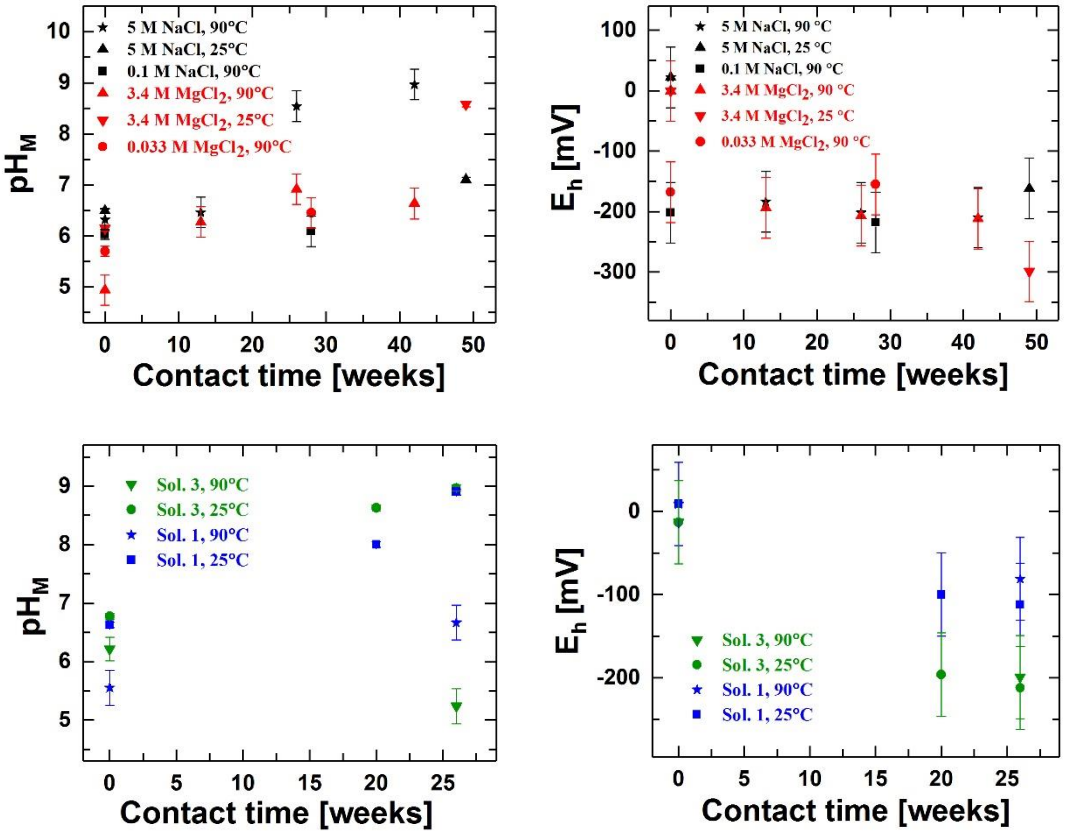

Figure 11. *pH_M (left) and E_h (right) evolutions for SGI corroded in different brines as a function of contact time.*

ii. Amounts of dissolved elements

At the end of the contact time, the amount of dissolved iron (Table 4) in solution was quantified by HR-ICP-MS. The amounts of dissolved iron were usually higher in $MgCl_2$ systems than in NaCl systems, and higher amounts of dissolved iron were obtained for experiments performed in dilute solutions. The amount of dissolved silicon was not quantified, but could be calculated using weight loss values [Morelová 2020]. However, these values overestimate the actual dissolved silicon concentration as they also include the amount of silicon present in corrosion products. The amount of carbon was not determined. Values of dissolved elements are very likely to dependent on the pH_M of the system and the nature of the formed corrosion product(s).

Table 4. *Amounts of dissolved iron (in µg/L) in SGI corrosion experiments. Numbers in parentheses correspond to the relative standard deviation in %.*

Systems	13 weeks	26 weeks	28 weeks	42 weeks	49 weeks
5 M NaCl, 90°C	103 (24)	131 (7.6)	-	151 (5.6)	-
5 M NaCl, 25°C	-	-	-	-	300 (2.6)
0.1 M NaCl, 90°C	-	-	16500 (0.2)	-	-
3.4 M $MgCl_2$, 90°C	216946 (2.2)	61875 (0.7)	-	105000 (2.1)	-
3.4 M $MgCl_2$, 25°C	-	-	-	-	42730 (2.3)
0.033 M $MgCl_2$, 90°C	-	-	11800 (0.9)	-	-
Solution 3, 90°C	-	4868 (1.5)	-	-	-
Solution 3, 25°C	-	<10	-	-	-
Solution 1, 90°C	-	360992 (1.2)	-	-	-
Solution 1, 25°C	-	63238 (0.3)	-	-	-

iii. Corrosion rates

Corrosion rates (Table 5) were calculated from the weight loss. In concentrated salt solutions at 90°C, the corrosion rate usually decreased with time, and values in $MgCl_2$ solutions are higher than in NaCl. The decrease with time can be explained by the presence of a layer of corrosion products at the surface protecting the steel. A further decrease for longer contact times may still occur. In dilute solutions, the nature of the salt seems to have no significant effect on the corrosion rate. In all systems, the corrosion rate is lower at 25°C than at 90°C, hinting at an effect of temperature on the corrosion rate. The effect of temperature is particularly clear for Solutions 1 and 3.

Interestingly, corrosion rates can be correlated with pH_M values (Figure 11): for higher pH_M values lower corrosion rates were observed. For example, in 5 M NaCl at 90°C a corrosion rate of 1.2 µm/a was obtained after 42 weeks of contact time at pH_M ~9.0, whereas in 3.4 M $MgCl_2$ under identical contact time and temperature the corrosion rate was 16.9 µm/a at pH_M ~6.6.

The effect of sulfate on corrosion rate can be estimated by comparing 3.4 M $MgCl_2$ and Solution 1 at 90°C after 26 weeks. Very comparable rates were obtained for both systems and they had very comparable pH_M values. The presence of sulfate seems not to affect the corrosion rate. Consequently, observed differences in corrosion rates may best be explained by differences in pH_M and ionic strength.

Table 5. *Corrosion rates (in µm/a) from SGI corrosion experiments based on weight loss.*

Systems	13 weeks	20 weeks	26 weeks	28 weeks	42 weeks	49 weeks
5 M NaCl, 90°C	2.89±0.05	-	1.01±0.05	-	1.22±0.05	-
5 M NaCl, 25°C	-	-	-	-	-	1.11±0.05
0.1 M NaCl, 90°C	-	-	-	10.0±1.0	-	-
3.4 M $MgCl_2$, 90°C	38.1±2.0	-	23.1±1.5	-	16.9±1.5	-
3.4 M $MgCl_2$, 25°C	-	-	-	-	-	1.22±0.05
0.033 M $MgCl_2$, 90°C	-	-	-	10.0±1.0	-	-
Solution 3, 90°C	-	-	9.6±1.0	-	-	-
Solution 3, 25°C	-	1.26±0.05	0.79±0.05	-	-	-
Solution 1, 90°C	-	-	26.3±1.5	-	-	-
Solution 1, 25°C	-	2.07±0.05	3.65±0.05	-	-	-

Corrosion rates for SGI in Solutions 1 and 3 at elevated temperature have been reported. Smailos et al. [1987] reported a corrosion rate of 46 µm/a in Solution 1 at pH ~4.0 whereas in this project the rate was ~26 µm/a at pH_M = 6.7, showing the importance of pH on corrosion. In Solution 3 at 150°C, they reported 25 µm/a at pH 6.0-7.0 while in this project it was ~10 µm/a at 90°C and pH_M = 5.2. The value obtained in this project in Solution 3 at 90°C is comparable to that reported for cast steel contacting Ar-purged synthetic seawater at pH ~8 of 6-8 µm/a [King, 2008]. These values are larger than typical values of ~1-2 µm/a reported for carbon steel and cast steel exposed to clayey groundwaters [King, 2008].

iv. Secondary phases and evolutions

1. Corrosion in 5 M NaCl at 90°C

In 5 M NaCl at 90°C, the amounts of formed corrosion products increased with contact time (Figure 12). After 13 weeks, particles had platelet-like morphology, which then evolved into clustered platelets and octahedral morphology. After 42 weeks, particles of octahedral morphology dominated, with sizes of ~20 µm, while platelet-like structures were present in lower amounts. XPS analysis [Morelová, 2020] revealed comparable Fe speciation from 13 to 42 weeks with the presence of Fe(II) and Fe(III), while O 1*s* spectra indicated the presence of oxide and hydroxide evolving into only oxide after 42 weeks.

Chemical analysis by EDX [Morelová, 2020] suggested that particles of platelet-like morphology are iron silicates and particles of octahedral shape are magnetite. Typical iron silicates may be greenalite ($Fe_{2-3}Si_2O_5(OH)_4$) or cronstedtite ($Fe_3(Si,Fe)O_5(OH)_4$), but Si/Fe atomic ratios rather suggest the later compound. XRD analysis corroborated the presence of magnetite and iron silicate, but both sheet silicates cannot be distinguished by XRD (Figure 12). At shorter contact time, only steel was detected. With increasing contact time, the intensity of reflexes associated with magnetite increased, while the presence of iron silicate was also clearly evidenced.

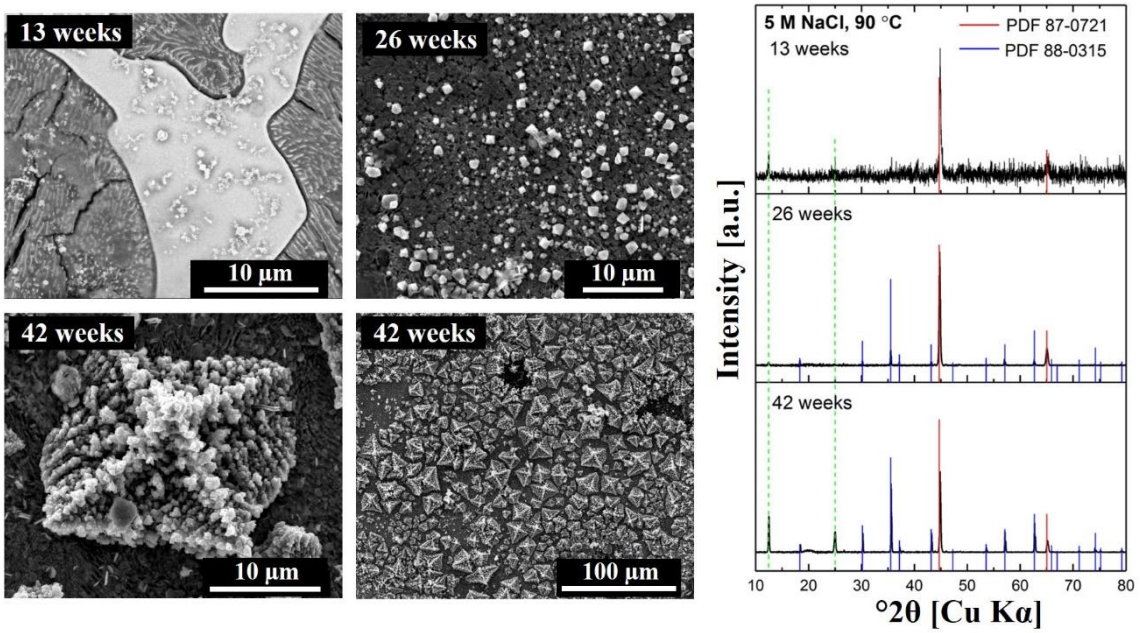

Figure 12. *Electron micrographs (left and middle) and X-ray diffractograms (right) for SGI corroded in 5 M NaCl at 90°C for various contact times (PDF 87-0721 refers to the initial steel, PDF 88-0315 to magnetite and vertical green dotted lines to greenalite/cronstedtite).*

Pourbaix diagrams were calculated (Figure 13) to determine if the identified phases would be thermodynamically stable under the given pH_M and E_h conditions. Points in the diagram correspond to pH (in activity) and E_h measured after 13, 26 and 42 weeks of contact time. The Pourbaix diagram suggests hematite is the long-term stable phase, without precipitation after 13 weeks, with minnesotaite (talc in which Mg^{2+} is replaced by Fe^{2+}) present under more reducing conditions. Lowering the silicon activity shows that magnetite and greenalite (instead of minnesotaite) would be stable, highlighting the importance of dissolved silicon. Crystalline hematite has a very high thermodynamic stability but its formation can be kinetically hindered so that other Fe-phases can form, such as for example cronstedtite. However, this sheet silicate is not appearing on the diagram because magnetite is more stable. The dissimilarities in the nature of the prevailing corrosion phases between experiment and modeling is an indication for locally different conditions favoring one phase over the other and of the role of kinetics on phase formation. Nevertheless, given the uncertainty on the amount of dissolved silicon and on the measured E_h value, the detected phases may very likely be of relevance in the long-term of a repository system. Note that diagrams show that points are not at the stability line of water, suggesting either insufficient tightness of the autoclaves or difficulties with the used redox electrodes.

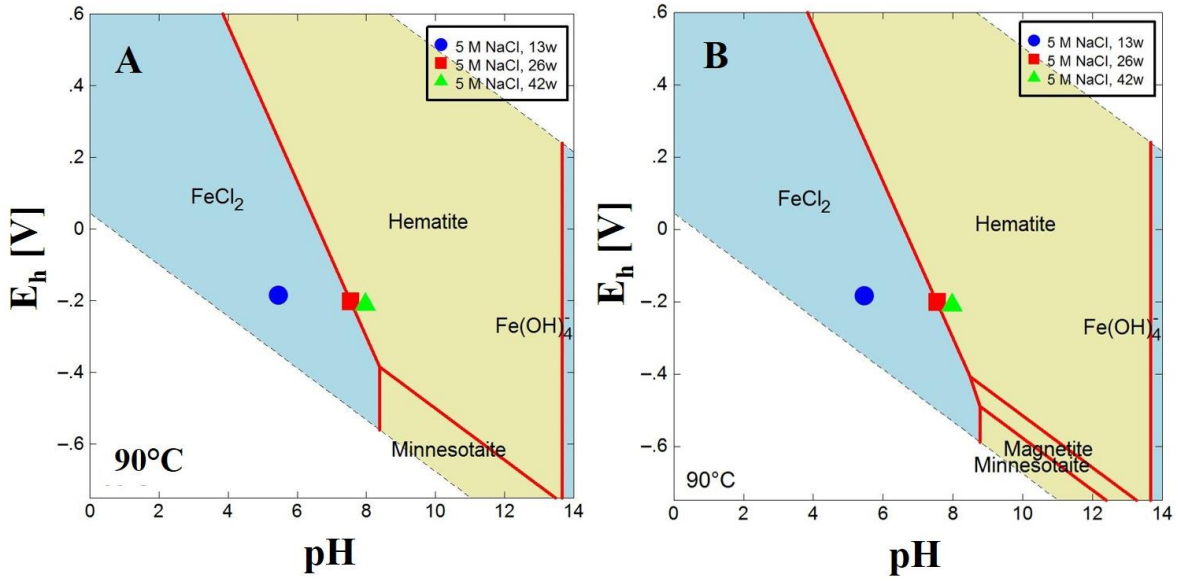

Figure 13. *Pourbaix diagrams corresponding to SGI corrosion experiments in 5 M NaCl at 90°C calculated with the [PI] database and the Pitzer approach. $SiO_{2,aq}$ activity obtained from weight loss, log a = -2.9 (A) and reduced $SiO_{2,aq}$ activity of log a = -3.5 (B).*

A sample was prepared by contacting SGI with 5 M NaCl at 90°C for 31 weeks for analysis of the corrosion profile using synchrotron-based methods. Before application of synchrotron radiation, the crosscut sample was characterized in the laboratory. Optical microscopy enabled first to select one region of interest. Subsequently, SEM-EDX and µRaman spectroscopy (Figure 14) hinted at the presence of various phases, such as cronstedtite at the former place of graphite inclusions (spots 3, 4), magnetite close to the non-corroded steel (spots 5, 6, 8, A) and iron hydroxychloride close to steel/corrosion layer interface (spots 1, 2, 7, 9, 10, B). Results of EDX analysis are reported elsewhere [Morelová 2020].

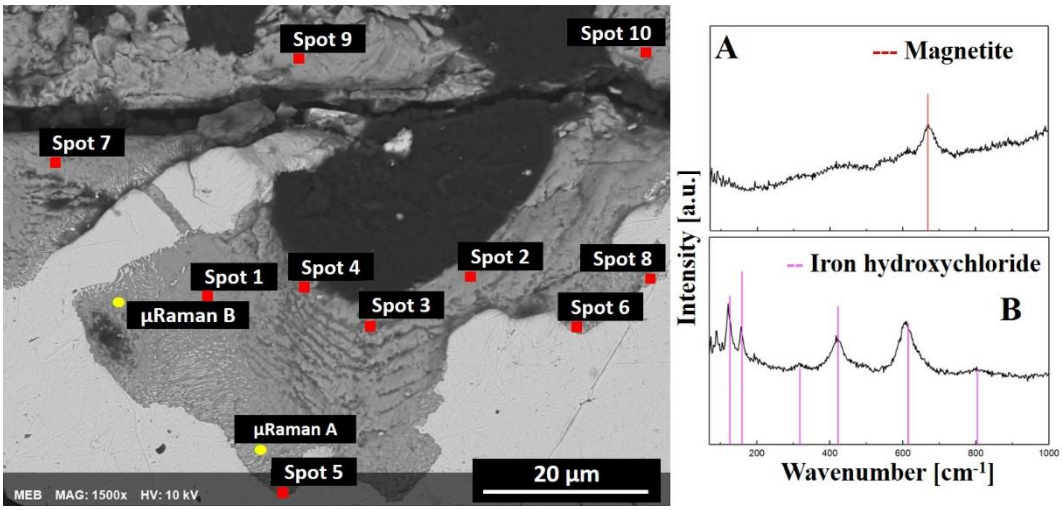

Figure 14. *Electron micrograph (left) of the corroded interface for SGI in contact with 5 M NaCl at 90°C for 31 weeks. Spots show location for EDX and µRaman analyses. Raman spectra (right) recorded at locations A and B.*

Using synchrotron radiation, a µXRF map (Figure 15) was recorded from the non-corroded steel through the corrosion layer and to the resin. The map representing the intensity of iron fluorescence shows a decrease in intensity at the corroding interface, hinting at the presence of secondary phases. Information on Fe speciation was obtained by probing the *K*-edge by XAS at several positions. Linear combination fitting of experimental spectra using reference compounds indicated the presence of cronstedtite and iron hydroxychloride, but not homogeneously distributed. Outcomes suggest that cronstedtite forms first followed by magnetite. Cracks form subsequently in this layer, and the diffusion of chloride at the steel/corrosion layer interface leads to the formation of iron hydroxychloride. This sequence

would be consistent with the presence of that later compound in thickest areas of the corrosion layer, close to the steel surface. This finding is in line with SEM-EDX and μRaman analyses.

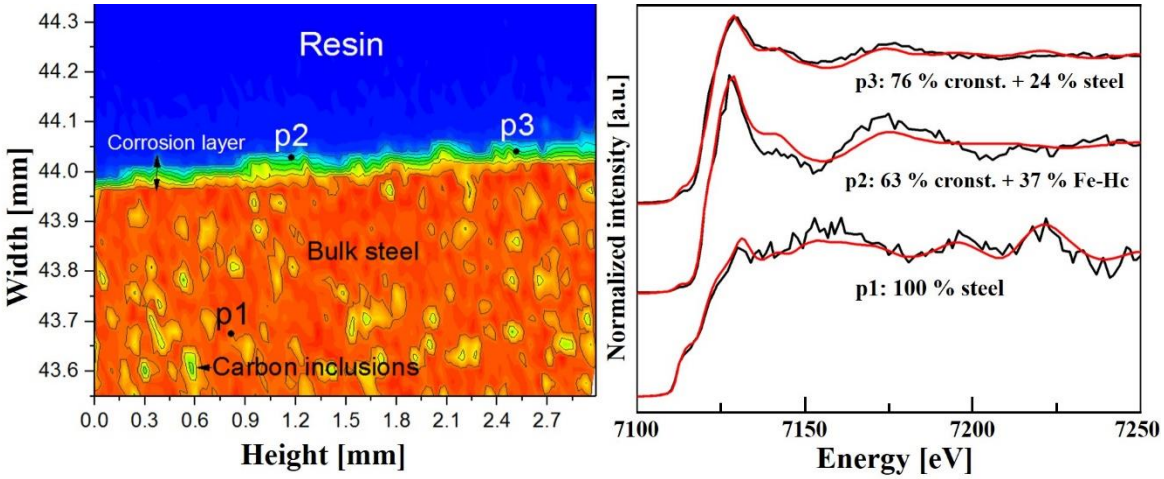

Figure 15. *Fe Kα intensity map (left) across the corroding interface for SGI contacted with 5 M NaCl for 31 weeks at 90°C. The map indicates the position of points of interest for probing the Fe K-edge by XAS (right). Black lines are experimental spectra, red lines are fit to experimental data using spectra recorded for the pristine steel, cronstedtite (cronst.) and iron hydroxychloride (Fe-Hc).*

2. Corrosion in 5 M NaCl at 25°C

SGI was contacted with 5 M NaCl for 49 weeks at room temperature in order to test the effect of temperature on corrosion. In this experiment, the surface was completely covered with crystals of hexagonal morphology, and additional hexagonal crystals sitting on platelets (Figure 16). XPS analysis of the platelets showed the presence of Fe(II) and Fe(III), along with chloride, hinting at the presence of chloride green rust. EDX analysis [Morelová 2020] showed that hexagonal structures do not contain sodium, and Fe:O:Cl ratios suggest it is iron hydroxychloride. XRD analysis corroborated the presence of green rust as corrosion product, but the amount of iron hydroxychloride was too low to be detected.

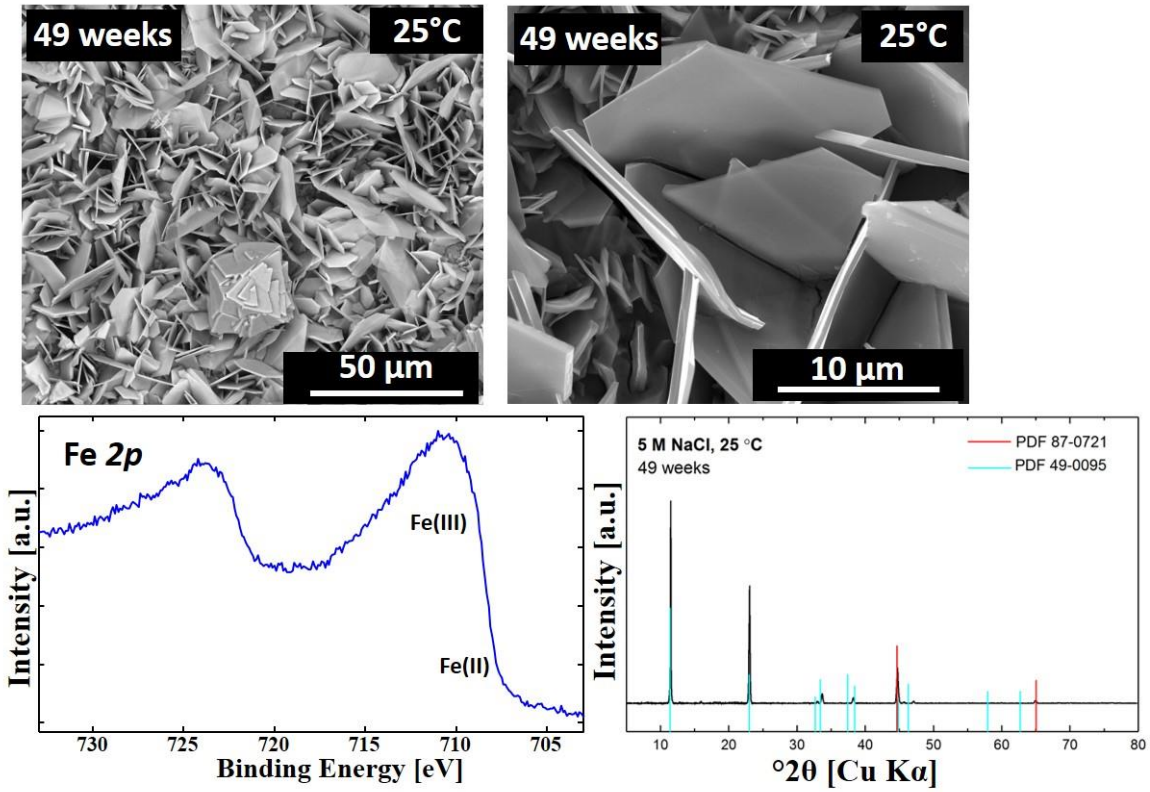

Figure 16. *Electron micrographs (top), XPS 2p narrow line (lower left) and XRD pattern (lower right) for SGI contacted with 5 M NaCl for 49 weeks at 25°C. XRD analysis identified the presence of steel (PDF 87-0721) and chloride green rust (PDF 49-0095).*

At room temperature, the pH increased less during the course of the experiments than at 90°C. It stayed close to neutral (Figure 11) where it favored the formation of chloride green rust [Refait et al., 1998], while the presence of high chloride content also renders the formation of iron hydroxychloride possible. Green rust is generally not a thermodynamically stable phase [Usman et al., 2018], but experimental conditions place this experiment within the stability field of green rust on Pourbaix diagram reported by Refait et al. [1998].

3. Corrosion in 0.1 M NaCl at 90°C

The nature of the corrosion products observed for SGI in contact with 0.1 M NaCl at 90°C for 28 weeks is the same as those for 5 M NaCl at 90°C. Electron micrographs showed the presence of crystallites of octahedral morphology and stacks of hexagonal platelets (Figure 17). EDX analysis [Morelová, 2020] identified these crystals as being magnetite and cronstedtite, which was corroborated by XRD analysis. For this experiment, the Pourbaix diagram is comparable

to that at higher ionic strength, but the $FeCl^+$ ($FeCl_2$)/ solid phase borderline moves to lower pH values [Morelová, 2020].

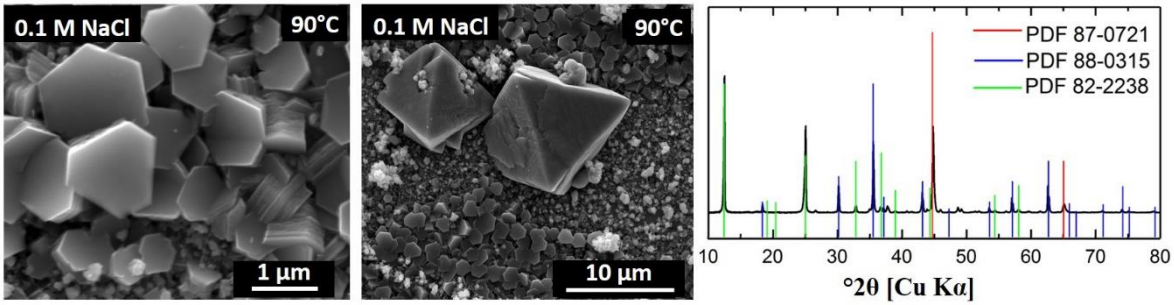

Figure 17. *Electron micrographs (left, middle) and XRD pattern (right) for SGI contacted with 0.1 M NaCl for 28 weeks at 90°C. XRD analysis identified the presence of steel (PDF 87-0721), magnetite (PDF 88-0315) and cronstedtite (PDF 82-2238).*

4. Corrosion in Solution 3 at 90°C and at 25°C

SGI was also contacted with Solution 3 at 90°C for 26 weeks to see whether the presence of minor amounts of sulfate has an effect on the corrosion. The obtained surface coverage (Figure 18) was lower than in pure NaCl brine, which may be explained by the lower pH_M value (5.2). Unfortunately, the amount of corrosion products was too low for XRD analysis. However, XPS analysis [Morelová, 2020] showed the presence of Fe(II) and Fe(III) while EDX analysis hinted at the presence of iron silicates with a fraction of Fe(II) replaced by Mg(II) from the brine.

Low corrosion damage was also observed for the same system at 25°C (Figure 18). After 20 weeks of contact time, electron micrographs showed a small but preferential attack in the vicinity of graphite inclusions, likely due to positioning of cathode (graphite) and anode (steel). Only Fe(0) could be detected by XPS at the surface [Morelová, 2020], except at the damage close to the graphite inclusion where a low contribution of Fe(II) could be detected. After 26 weeks, no corrosion product can still be seen at the surface. However, zooming into the hole used to hang the coupon showed the presence of hexagonal platelets, certainly caused by crevice corrosion. XPS analysis evidenced the presence of Fe(II), with low contribution from Fe(III), sulfate and hydroxide. The chemical analysis (EDX) suggested the presence of precipitated sodium sulfate and possibly $Fe(OH)_2$. The presence of this latter compound would agree with the morphology of observed particles.

According to the Pourbaix diagram calculated for conditions representative of these experiments [Morelová, 2020], pyrite would be the thermodynamically stable phase to expect. However, sulfate reduction leading to the formation of pyrite is mostly likely to happen in the presence of microbes and not in experiments performed in autoclaves.

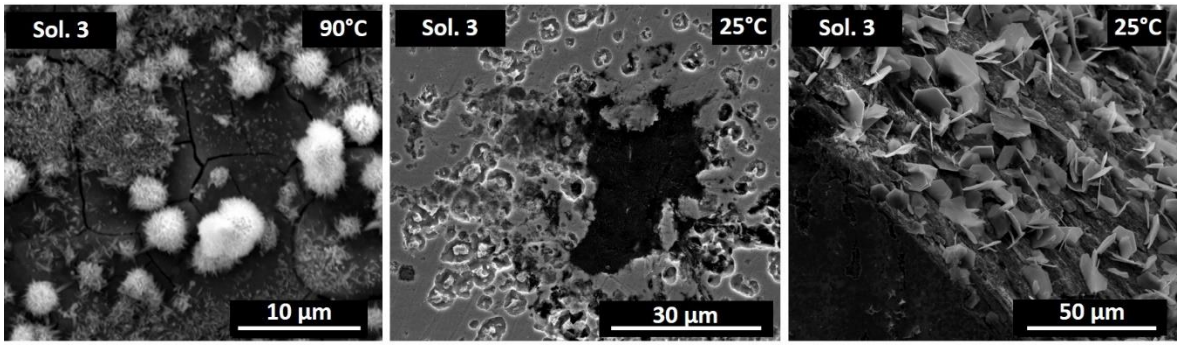

Figure 18*. Electron micrographs for SGI contacted with Solution 3 at 90°C for 26 weeks (left), at 25°C for 20 weeks (middle) and at 25°C for 26 weeks (right).*

5. Corrosion in 3.4 M $MgCl_2$ at 90°C

Contacting the SGI with 3.4 M $MgCl_2$ at 90°C resulted in a surface coverage differing from that of contacting NaCl brines. Particles were of pyramidal shape about 50 µm in size already after 13 weeks of contact time (Figure 19). XPS Fe 2*p* and O1*s* narrow spectra [Morelová, 2020] were consistent with a Fe(II) hydrous phase. Additionally, analysis by EDX indicated that particles are made of Cl, Fe, O and Mg, and are free from Si. X-ray diffraction identified the main corrosion product as iron hydroxychloride ($Fe_2(OH)_3Cl$). Lower amounts of amakinite ($(Mg,Fe)(OH)_2$) were also detected in that sample. Note that the substitution of Fe(II) by Mg(II) in iron hydroxychloride is possible, owing to very similar atomic radii [Shannon, 1976]. The nature of the corrosion products significantly differed from that detected in NaCl brines.

The sample with 13 weeks of contact time was embedded in resin, crosscut and polished for SEM-EDX analysis. Images [Morelová, 2020] showed the presence of a rather uniform 14-18 µm thick 1ayer of corrosion products, and graphite inclusion at the interface being removed certainly upon polishing. The distribution of elements showed correlations between O, Cl and Mg, corroborating the presence of iron hydroxychloride.

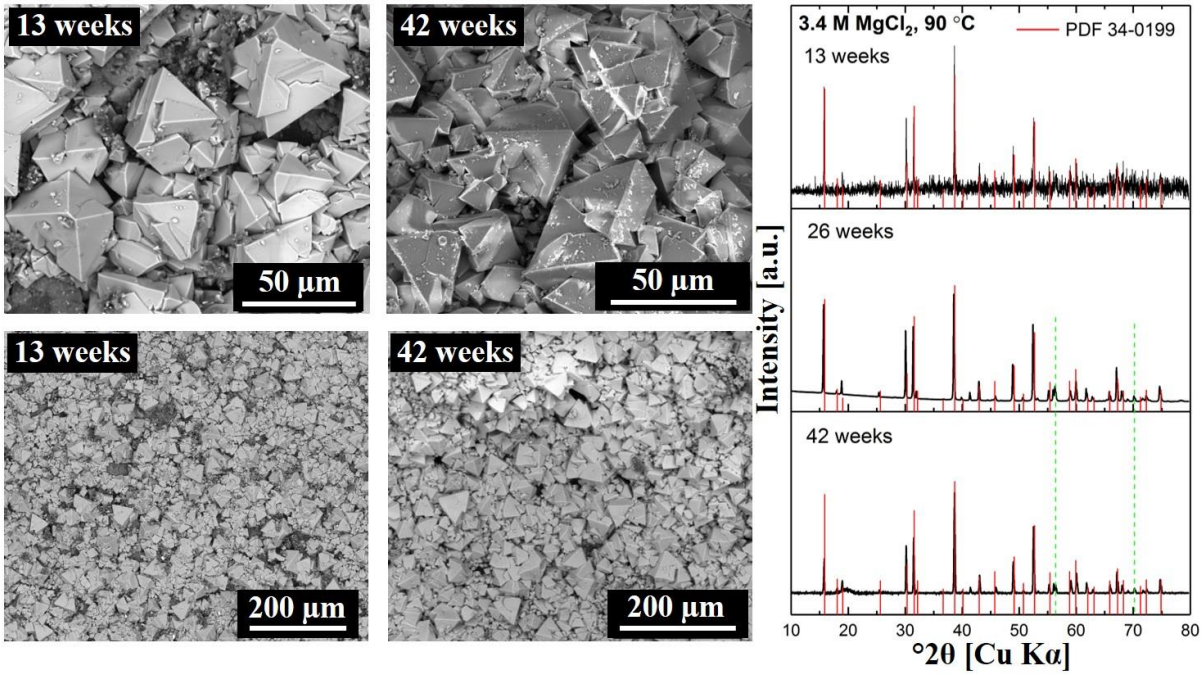

Figure 19. *Electron micrographs of SGI contacted with 3.4 M $MgCl_2$ at 90°C for 13 weeks (left), for 42 weeks (middle) and X-ray diffractograms (right) for samples after 13, 26 and 42 weeks of contact time. On diffractograms, PDF 34-0199 refers to iron hydroxychloride, the dotted green lines to amakinite.*

Iron hydroxychloride is metastable and prone to transformation into green rust [Nemer et al., 2011; Rémazeilles and Refait, 2008] or magnetite [Schlegel et al., 2016] depending on the geochemical boundary conditions. Thermodynamic data for this compound are very limited, and the stability constant is only available for 25°C. Using the amounts of dissolved elements at 42 weeks, and not including this phase for calculating the Pourbaix diagram, shows (Figure 20) that no phase would be expected to form under experimentally determined pH_M and E_h. In contrast, including this phase shows that experimental conditions are very close to the stability of iron hydroxychloride. This finding suggests that this phase may actually be thermodynamically stable under high ionic strength and weakly acidic conditions. The mismatch between experimental data and thermodynamically stable phase can also be attributed to high gradients in local conditions and/or kinetics of formation. The calculated activity of iron is also depending on the database, while the used [PI] database may be a source of uncertainty due to the lack of reliable and complete data for activity calculation using the Pitzer approach.

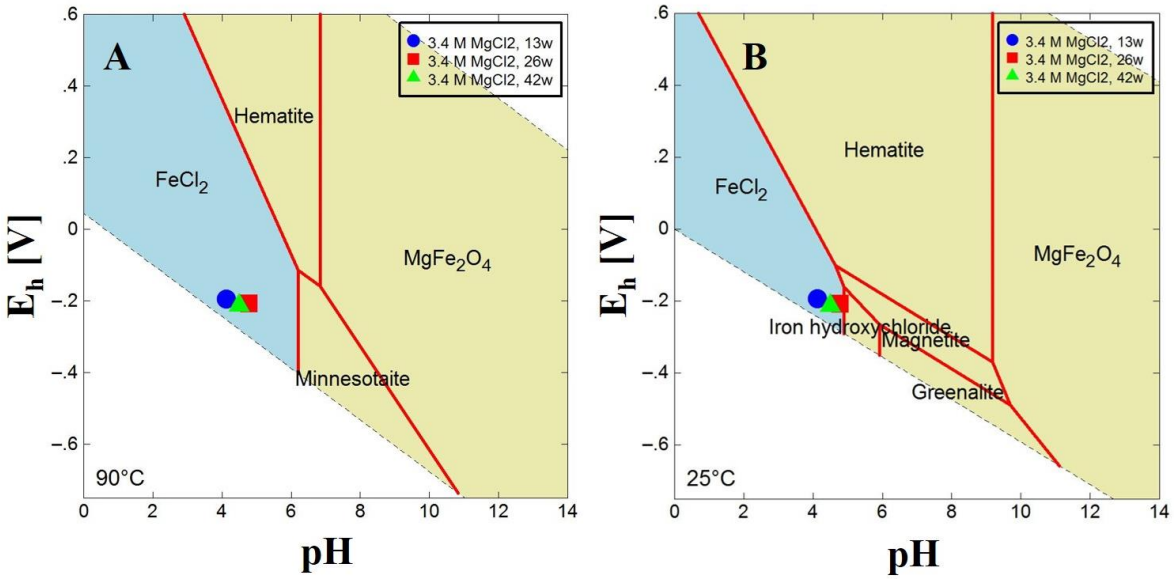

Figure 20. *Pourbaix diagrams corresponding to SGI corrosion experiments in 3.4 M $MgCl_2$ at 90°C calculated with the [PI] database and the Pitzer approach. Ferrous ion activities were taken from ICP-MS (log a = -3.65) and silica activities from weight loss ($SiO_{2,aq}$, log a = -1.87) (A). Diagram for higher iron (log a = 3) and lower Si (log a = -5) activities (B).*

SGI was also contacted with 3.4 M $MgCl_2$ at 90°C for 31 weeks for analysis of the corrosion front by application of synchrotron-based methods on a crosscut following the same procedure as for the sample prepared in 5 M NaCl. The analysis by optical microscopy [Morelová, 2020] revealed a rather uniform attack of the surface, and µRaman spectroscopy evidenced the presence of iron hydroxychloride and wüstite (FeO) (Figure 21). SEM-EDX analysis [Morelová, 2020] at various positions corroborated the presence of iron hydroxychloride, with Mg(II) replacing Fe(II), and further suggested the presence of possible Mg-Fe silicate or amakinite.

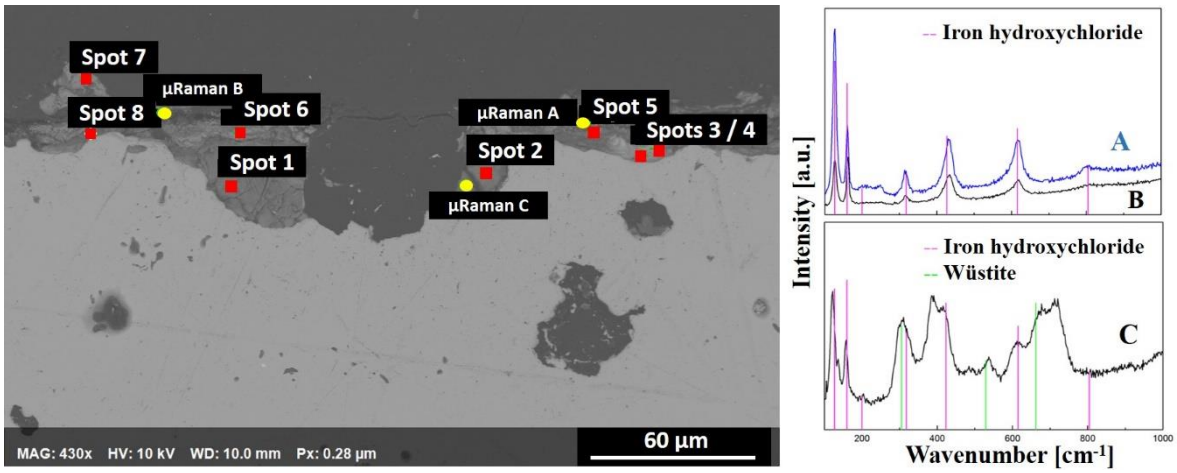

Figure 21. *Electron micrograph (left) of the corroded interface for SGI in contact with 3.4 M $MgCl_2$ at 90°C for 31 weeks. Spots show locations for EDX and µRaman analysis. Raman spectra (right) recorded at locations A, B and C.*

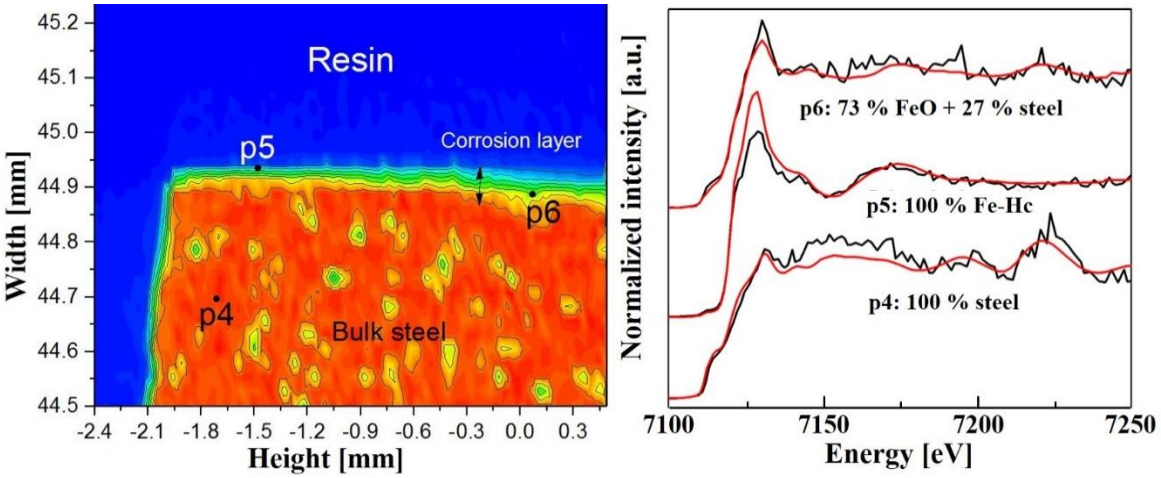

Figure 22. *Fe Kα intensity map (left) across the corroding interface for SGI contacted with 3.4 M $MgCl_2$ for 31 weeks at 90°C. The map indicates the position of points of interest for probing the Fe K-edge by XAS (right). Black lines are experimental spectra, red lines are fit to experimental data using spectra recorded for the pristine steel, wüstite (FeO) and iron hydroxychloride (Fe-Hc).*

At the steel/brine interface, a thick and rather homogeneous layer of corrosion products formed. Fits to the µXANES provided information on the nature of the corrosion products: iron hydroxychloride and wüstite closer to the surface (Figure 22), which agrees with the µRaman analysis. Furthermore, the presence of these compounds was also detected by XRD analysis in

a line scan through the corroded interface [Morelová, 2020]. The identification of wüstite as corrosion product is a new finding, as it could not be detected by surface analysis in the laboratory.

6. Corrosion in 3.4 M $MgCl_2$ at 25°C

Contacting SGI with 3.4 M $MgCl_2$ at 25°C for 49 weeks resulted in the formation of crystallites of pyramidal morphology, about 10-15 µm in size (Figure 23), with a coverage lower than at 90°C. Analysis by SEM-EDX and XPS yielded results comparable to that obtained for the same system at 90°C [Morelová, 2020]. XRD analysis identified these crystallites as iron hydroxychloride. Consequently, the same corrosion product formed at 25°C and at 90°C, and it may very likely be attributed to the high ionic strength (I = 10.2 M).

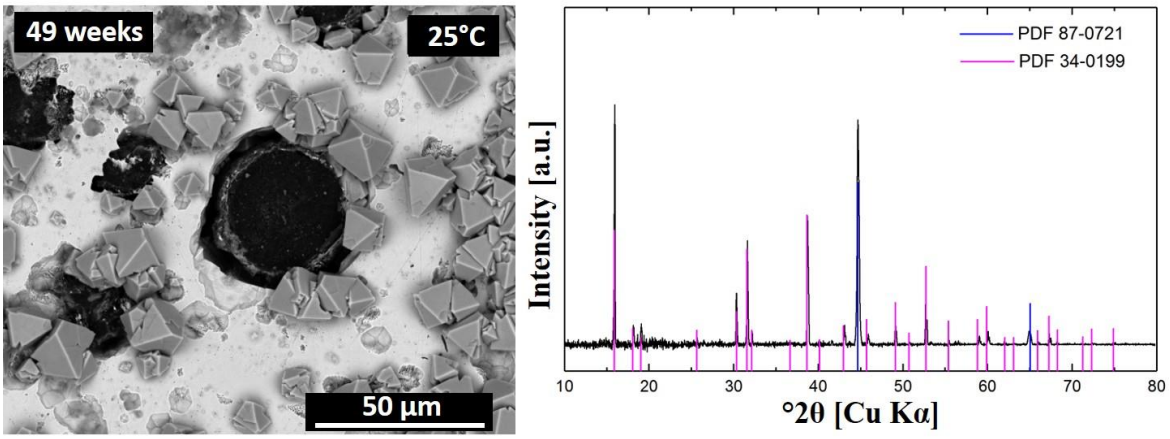

Figure 23. *Electron micrograph (left) and X-rax diffractogram (right) for SGI contacted with 3.4 M $MgCl_2$ for 49 weeks at 25°C. On the diffractogram, PDF 87-0721 refers to the non-corroded steel surface and PDF 34-0199 to iron hydroxychloride.*

7. Corrosion in 0.033 M $MgCl_2$ at 90°C

In 0.033 M $MgCl_2$ at 90°C, phases of octahedral and stacked hexagonal geometry formed. Results [Morelová, 2020] collectively identified these phases as magnetite and cronstedtite, as in 0.1 M NaCl. This suggests that at this ionic strength the nature of the formed secondary phases is not affected by the nature of the salt, the only noticeable difference is the presence of Mg(II) replacing Fe(II) within cronstedtite. This finding is not surprising as the amounts of

dissolved elements are very comparable, as a consequence of very comparable pH_M / E_h values, resulting in very similar Pourbaix diagrams.

8. Corrosion in Solution 1 at 90°C and at 25°C

Upon contact of SGI with Solution 1 at 90°C, particles of pyramidal morphology formed, with an additional phase laying on top. Compared to particles obtained in 3.4 M $MgCl_2$, pyramidal particles may be iron hydroxychloride, but the XPS Fe 2*p* narrow spectrum hinted at the presence of Fe(III) in significant amounts. Analysis of the solids by SEM-EDX revealed that pyramids have a composition matching the iron hydroxychloride composition, while results suggest that the second phase is chloride green rust, containing Mg(II) partly replacing Fe(II). The presence of green rust would be consistent with the presence of Fe(III) detected by XPS. XRD analysis confirmed the presence of iron hydroxychloride. This result is comparable to that of the pure 3.4 M $MgCl_2$ system, suggesting that the presence of minor amounts of additional salt does not play a significant role as long as pH_M are identical. The analysis of the crosscut by SEM revealed a thickness of the corrosion layer of 23-32 µm. At 25°C, SGI hardly corroded upon contact with Solution 1, no presence of corrosion products could be detected by surface analytics.

The nature of the corrosion products detected in SGI corrosion experiments are summarized in Table 5, together with pH_M and E_h values. Results discussed above show that corrosion products are distributed heterogeneously at the corrosion front and point at reaction(s) taking place without reaching equilibrium in investigated systems. This is also reflected by differences in the nature of the experimentally determined phases with that suggested by thermodynamic calculations (Pourbaix diagrams).

Table 6. *Observed corrosion products formed upon contact of SGI with various brines (Fe-Hc: iron hydroxychloride) at 90°C and at 25°C.*

Brine	T [°C]	pH_M	E_h [mV]	Experimentally determined secondary phase
5 M NaCl	90	9.0±0.3	-210±50	Cronstedtite and Fe_3O_4. Fe-Hc at the steel/corrosion layer interface.
5 M NaCl	25	7.10±0.05	-162±50	Chloride green rust, few Fe-Hc particles.
0.1 M NaCl	90	6.1±0.3	-218±50	Cronstedtite and Fe_3O_4.
Solution 3	90	5.2±0.3	-199±50	Cronstedtite with Mg partially replacing Fe(II).
Solution 3	25	8.97±0.05	-212±50	No phase precipitation on the surface, marginal presence of $Fe(OH)_2$ in the hole of the coupon.
3.4 M $MgCl_2$	90	6.6±0.3	-212±50	Fe-Hc with partial Fe(II) replacement by Mg(II). $(Fe,Mg)(OH)_2$ as potential precursor. FeO at the steel/corrosion layer interface.
3.4 M $MgCl_2$	25	8.58±0.05	-299±50	Fe-Hc with partial Fe(II) replacement by Mg(II).
0.033 M $MgCl_2$	90	6.4±0.3	-155±50	Cronstedtite and Fe_3O_4.
Solution 1	90	6.7±0.3	-81±50	Fe-Hc with partial Fe(II) replacement by Mg(II). Chloride green rust with partial Fe(II) replacement by Mg(II).
Solution 1	25	8.90±0.05	-112±50	No phase precipitation.

v. Corrosion mechanism

In all SGI corrosion experiments, graphitic corrosion took place, and iron close to inclusions was preferentially corroded due to positioning of anodic sites (iron) close to cathodic sites (graphite). Overall, uniform corrosion was observed in NaCl and $MgCl_2$ brines, without pit formation, and the extent of corrosion was governed by the pH_M. Coupling oxidation of iron and reduction of water, ferrous hydroxide may have formed, because of Fe^{2+} and OH^- accumulation, without change in pH.

SGI contains 3.4 wt % Si which was released upon steel corrosion. The solubility of silicon can reach ~1 mmol/L at near-neutral pH, 25°C and 0.3 M NaCl [Ahmed et al., 2015], which is sufficient for the formation of sheet silicates under certain conditions. In this project, the formation of cronstedtite was observed at 90°C in systems where pH_M was below 6.5 (5 M NaCl, 0.1 M NaCl, 0.033 M $MgCl_2$ and Solution 3). The formation of this phase does not affect the pH_M (Eq. 6) [Schlegel et al., 2014, 2016], and observed pH_M variations with contact time in

these systems can be explained by water reduction. The observed decrease in E_h can be attributed to the formation of hydrogen.

$$4Fe(0) + SiO_{2,aq} + 7H_2O \leftrightarrow \boldsymbol{Fe_2^{2+}Fe^{3+}(Si, Fe^{3+}O_5)(OH)_4} + 5H_2 \quad \text{(Eq. 6)}$$

Magnetite forms after only 26 weeks in 5 M NaCl, and from there magnetite and cronstedtite coexist without evidence of transformation or spatial separation at the surface. Initially, cronstedite formed first, likely favored by the presence of dissolved silicon. Once silicon was depleted close to the surface, magnetite may have formed via the Schikorr reaction (Eq. 5). Both phases are stable under comparable conditions, but the preferential formation of one over the other may result from differences in local concentrations of iron and silicon. The concomitant formation of both phases was also observed in dilute systems (0.1 M NaCl/0.033 M $MgCl_2$) because lowering the ionic strength shifts the stability fields of solid phases to lower pH_M values.

In 5 M NaCl at 90°C, no Cl-bearing phase could be detected, in line with the Pourbaix diagram. On the long-term, magnetite is expected to be stable and not to transform into another phase (e.g., cronstedtite). Minnesotaite is another long-term relevant phase, but its formation is dependent on the dissolved silicon content. In the timeframe of the experiments, no transformation of cronstedtite into magnetite could be detected, it may likely have been stabilized temporarily by cathodic protection. However, with increasing time, cracks and pores may have formed, which enabled chloride to reach the metal surface where it enhanced the anodic reaction. This spatial separation of anodic and cathodic reactions lead to electrophoretic migration and accumulation of chloride close to the surface where the formation of iron hydroxychloride was locally favored [Schlegel et al., 2016, 2018]. Conditions were only favorable in areas of thick layer of corrosion products, where electrochemical control took place. In this system, the interface is thus made of an internal layer of iron hydroxychloride and an external layer of magnetite and cronstedtite. This is the first time the presence and composition of a double layer for low-alloyed steel under high saline conditions is reported. Similar phenomenon was reported for low carbon steel exposed to clay porewater under anoxic and slightly alkaline conditions at 85°C for up to 2 years, where Cl-bearing corrosion products formed despite relatively low chloride content in the porewater [Schlegel et al., 2016, 2018].

In 5 M NaCl at 25°C, the formation of green rust was evidenced. Green rust can form by direct precipitation from Fe^{2+} and Fe^{3+} or from $Fe(OH)_2$ in the presence of dissolved oxygen (Eq. 7). The pH_M of this system at 25°C was lower than in the counterpart at 90°C, and can possibly be explained by the consumption of OH^- to from green rust. Green rust covered significantly and homogeneously the surface, slowing down the corrosion by hindering the water and chloride diffusion to the surface. With time, cracks and pores would develop and the surface further corrode. The pH_M can locally increase due to water reduction and green rust can convert into a mixture of magnetite and $Fe(OH)_2$ at pH >10 [Jolivet et al., 2004; Usman et al., 2018]. However, depending on ionic strength, the conversion can already start at lower pH [Sagoe-Crentsil and Glasser, 1993; Tosca et al., 2018].

$$7Fe(OH)_2 + Fe_{aq}^{2+} + 2Cl^- + (2n+1)H_2O + 0.5\,O_2 \leftrightarrow \mathbf{2}(\boldsymbol{Fe_3^{2+}Fe^{3+}})(\boldsymbol{OH})_{\mathbf{8}}Cl \times nH_2O \quad \text{(Eq. 7)}$$

In 3.4 M $MgCl_2$ and in Solution 1, the increase in pH was lower at 90°C (from ~5.2 to ~6.6) than at 25°C (from ~6.2 to ~8.6), but the surface coverage by iron hydroxychloride was larger at elevated than at room temperature. At 25°C, the steel corroded and water was reduced to produce hydroxide ions, but no phase precipitated and thus the system could not be buffered. At these high ionic strengths, the formation of Cl-bearing phases was favored, whereas the formation of iron silicate was favored in dilute $MgCl_2$. Corrosion products formed in $MgCl_2$ brines, likely by direct precipitation from Fe^{2+} [Rémazeilles and Refait, 2008], contain Mg(II) partially replacing structural Fe(II), in agreement with earlies findings of low carbon steel corroded in concentrated $MgCl_2$ brines [Grambow et al., 1996; Westermann and Pitman, 1984].

Iron hydroxychloride was stable during the timespan of the experiments, certainly due to favorable conditions imposed by the corroding steel. However, it may not be stable on the long-term and may rather transform into green rust [Rémazeilles and Refait, 2008] or magnetite [Schlegel et al., 2016]. Green rust and iron hydroxychloride are stable under comparable pH/E_h conditions, with the later favored at lower E_h conditions. Interestingly, chloride green rust is also prone to transformation into another form (e.g., sulfate), given the appropriate anion, Fe^{2+} and traces of dissolved oxygen are present [Refait and Génin, 1993]. Analysis by µXAS of SGI corroded in 3.4 M $MgCl_2$ indicated the presence of FeO close to the surface. With time, this

compound may convert into $Fe(OH)_2$, and in the presence of high chloride concentrations, convert into iron hydroxychloride [Nemer et al., 2011; Rémazeilles and Refait, 2008].

In Solutions 3 and 1 at 25°C, no distinct corrosion product could be observed. In the presence of sulfate, pyrite could be relevant in the long-term, but its formation may be conditioned by microbial activity.

For this steel, corrosion products, which may be of importance in the long-term, are magnetite, iron hydroxychloride and sheet silicates such as minnesotaite. These phases were obtained by calculating Pourbaix diagram and detected experimentally, except minnesotaite. The steel contains significant amounts of silicon but minnesotaite was not detected experimentally, longer contact times would certainly be needed to form this phase.

e. Stainless steel corrosion in dilute to concentrated NaCl and $MgCl_2$ solutions

The analysis of coupon before use in corrosion experiments showed the presence of small scratches likely originating from the production, and small carbon impurity spots. Analysis by EDX showed good agreement of the elemental composition with values from the certificate. The experimental XRD pattern matched with the entry of the database of composition 70 % Fe, 11 % Ni and 19 % Cr. Finally, a root mean square roughness of < 6 nm was determined for the polished surface. Note that for this steel a protective layer of Cr_2O_3 forms instantaneously implying that Cr(III) is always present at the surface, even before contacting the brines.

i. pH_M and E_h evolutions

pH_M values remained rather constant in all experiments, or slightly increased (Figure 24). Likewise, E_h values did not change much over the course of the experiments indicating that reducing conditions did not develop. E_h values can be related to affinity of electron exchange for redox buffers such as Fe(II)/Fe(III). Results hint at very low corrosion rates, resulting in low amounts of dissolved iron. The presence of oxygen, which would result in an increase in E_h, was ruled out by probing the gas phase at the end of the experiments. Stainless steel is prone to pitting corrosion and pitting potentials (E_{corr}, E_{pit}) were determined for this steel in concentrated NaCl and $MgCl_2$ solutions (see above) yielding at 25°C E_{corr} = -70 mV and E_{pit} = 200 mV in 5 M NaCl, and E_{corr} = -440 mV and E_{pit} = -80 mV in 3.4 M $MgCl_2$. In autoclave experiments at

25C, E_h values (212 ± 50 mV in 5 M NaCl and 202 ± 50 mV in 3.4 M $MgCl_2$) are above this pitting potential, indicating an efficient passivation of the surface. Note that pitting can be a slow process and take place in the long-term.

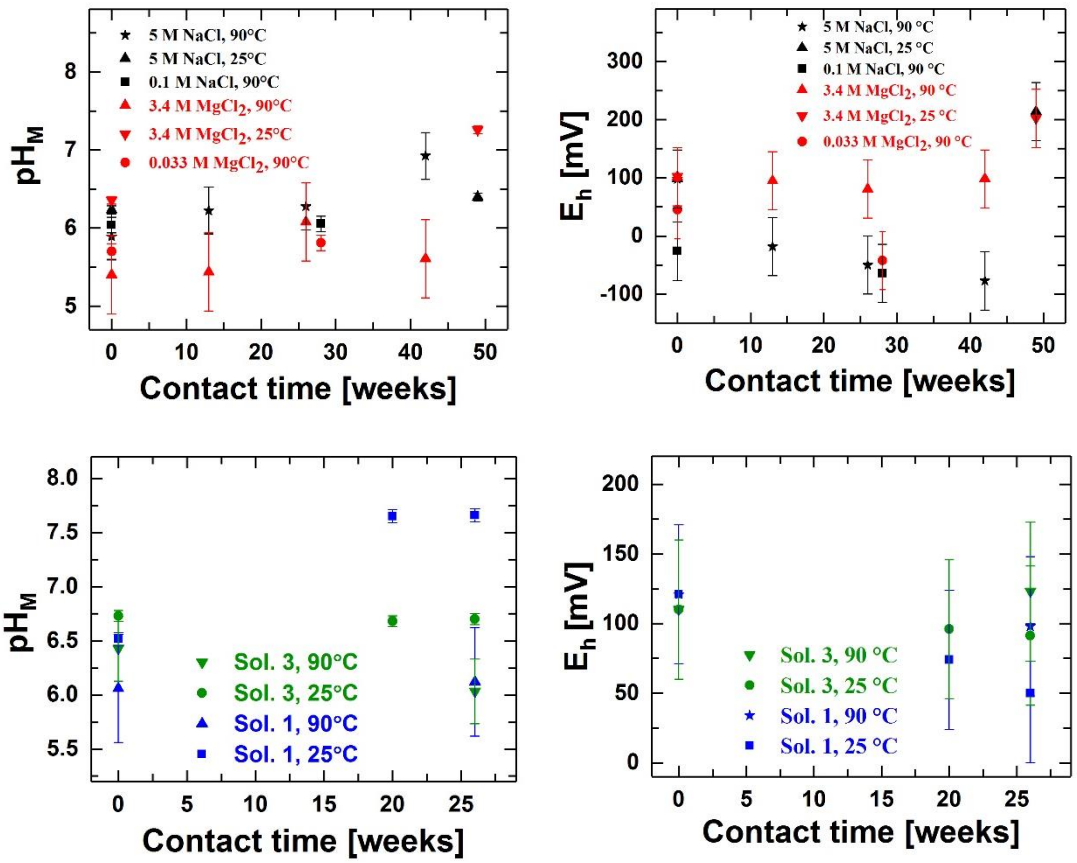

Figure 24. *pH_M (left) and E_h (right) evolutions for 309S corroded in different brines as a function of contact time.*

ii. Amounts of dissolved elements

Concentration dissolved of chromium, iron and nickel were quantified and are shown below for iron (Table 7) and elsewhere [Morelová, 2020] for chromium and nickel. Lowest values were obtained for chromium and highest for nickel. For chromium, determined concentrations were either below of close to the detection limit, which can be explained by the low solubility of Cr(III) oxide. For iron, the highest value was obtained in 3.4 M $MgCl_2$ at 90°C after 26 weeks. Dissolved amounts of iron increased first then decreased, hinting at dissolution followed by precipitation of solid phase(s). However, values are below the solubility limit of Fe(II) phases. Given experimental E_h values, the formation of Fe(III)-bearing phases is possible, and thus

explain the values of dissolved iron. The trend of dissolved amounts of nickel parallels that of iron, suggesting a behavior comparable for both elements. However, as nickel is not redox sensitive under given conditions, Ni may be entrapped in precipitating Fe- or Cr-bearing solids.

Table 7. *Amounts of dissolved iron (in µg/L) in 309S corrosion experiments. Numbers in parentheses correspond to the relative standard deviation in %.*

Systems	13 weeks	26 weeks	28 weeks	42 weeks	49 weeks
5 M NaCl, 90°C	11.93 (28.2)	61.1 (15.3)	-	<10	-
5 M NaCl, 25°C	-	-	-	-	<10
0.1 M NaCl, 90°C	-	-	117 (58.6)	-	-
3.4 M $MgCl_2$, 90°C	91 (43.9)	1099 (3.9)	-	<10	-
3.4 M $MgCl_2$, 25°C	-	-	-	-	<10
0.033 M $MgCl_2$, 90°C	-	-	<10	-	-
Solution 3, 90°C	-	668(23.5)	-	-	-
Solution 3, 25°C	-	<10	-	-	-
Solution 1, 90°C	-	151 (3.0)	-	-	-
Solution 1, 25°C	-	<10	-	-	-

iii. Corrosion rates

Corrosion rates (Table 8) were calculated from the weight loss. Values of <0.1 µm/a were obtained for most systems, except for Solutions 1 and 3 at 90°C. Typical corrosion rates reported for 309S are around 1 µm/a [Kursten et al., 2004]. It has also been used in *in situ* corrosion experiments at the Asse II salt mine, where after 5 years in an electrically heated borehole, a corrosion rate of 0.3-0.7 µm/a was found, with stress corrosion cracking and pitting corrosion (up to 200 µm in depth) [Smailos and Fiehn, 1995].

Table 8. *Corrosion rates (in µm/a) from 309S corrosion experiments based on weight loss.*

Systems	13 weeks	20 weeks	26 weeks	28 weeks	42 weeks	49 weeks
5 M NaCl, 90°C	<0.1	-	<0.1	-	<0.1	-
5 M NaCl, 25°C	-	-	-	-	-	<0.1
0.1 M NaCl, 90°C	-	-	-	<0.1	-	-
3.4 M $MgCl_2$, 90°C	<0.1	-	<0.1	-	<0.1	-
3.4 M $MgCl_2$, 25°C	-	-	-	-	-	<0.1
0.033 M $MgCl_2$, 90°C	-	-	-	<0.1	-	-
Solution 3, 90°C	-	-	0.49±0.05	-	-	-
Solution 3, 25°C	-	<0.1	<0.1	-	-	-
Solution 1, 90°C	-	-	0.45±0.05	-	-	-
Solution 1, 25°C	-	<0.1	<0.1	-	-	-

iv. Secondary phases and evolution

1. Corrosion in NaCl brines

At 90°C in 5 M NaCl, only a thin corrosion layer can be evidenced after 13 weeks and it hardly increases with contact time (Figure 25). After 13 and 26 weeks of contact time, XPS analysis indicated the presence of Cr(III), Fe(0), Fe(III), Ni(0) and a low Ni(II) contribution [Morelová, 2020], suggesting the formation of Cr_2O_3, $Cr(OH)_3$ and/or $NiFe_2O_4$ (possible solid solution with magnetite). After 42 weeks, XPS analysis suggested the presence of Cr(III) (hydr)oxide compounds and metallic Fe. Unfortunately, the surface coverage was too low for analysis by EDX or by XRD. The sample corroded for 13 weeks was embedded in resin and cross cut, but no surface damage could be detected by SEM.

One coupon was contacted with 5 M NaCl at 90°C for 31 weeks for analysis of the crosscut by synchrotron-based methods. Pre-characterization of the crosscut by optical microscopy showed the presence of two areas of interest where the thin corrosion layer was detached from the surface [Morelová, 2020]. Unfortunately, analysis by µRaman did not provide conclusive results, but SEM-EDX analysis revealed a composition possibly matching mixed $FeCr_2O_3/NiFe_2O_4$ and Cr_2O_3 or $Cr(OH)_3$ phases.

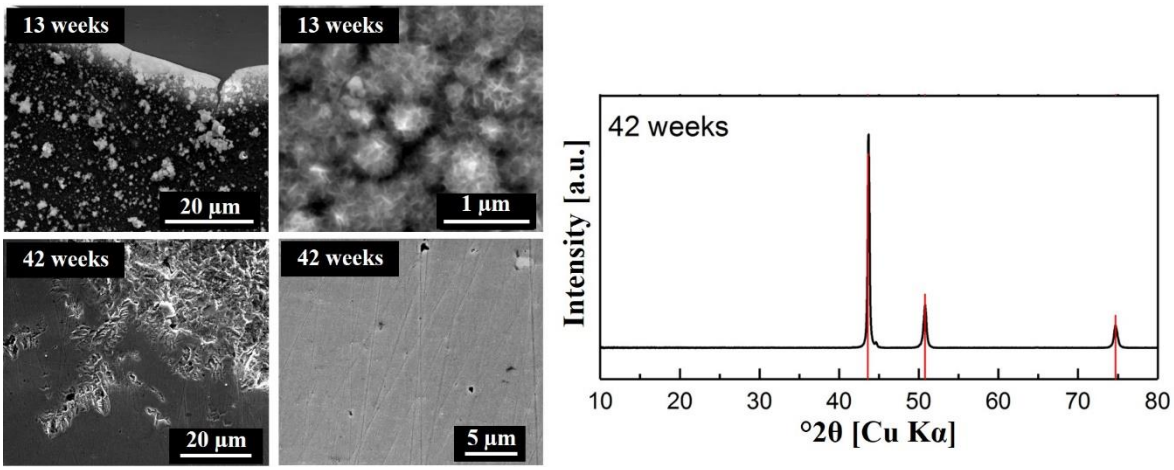

Figure 25. *Electron micrograph (left) and X-ray diffractogram (right) for 309S contacted with 5 M NaCl for 13 or 42 weeks at 90°C. On the diffractogram, vertical red bars refer to PDF 33-0397 corresponding to the non corroded steel.*

µXRF maps showing the elemental distribution of Cr, Fe and Ni where recorded, and points of interest were selected to obtain information on the nature of the formed corrosion products. The corroded interface is very thin and the distribution of Fe and Ni are comparable (Figures 26 and 27).

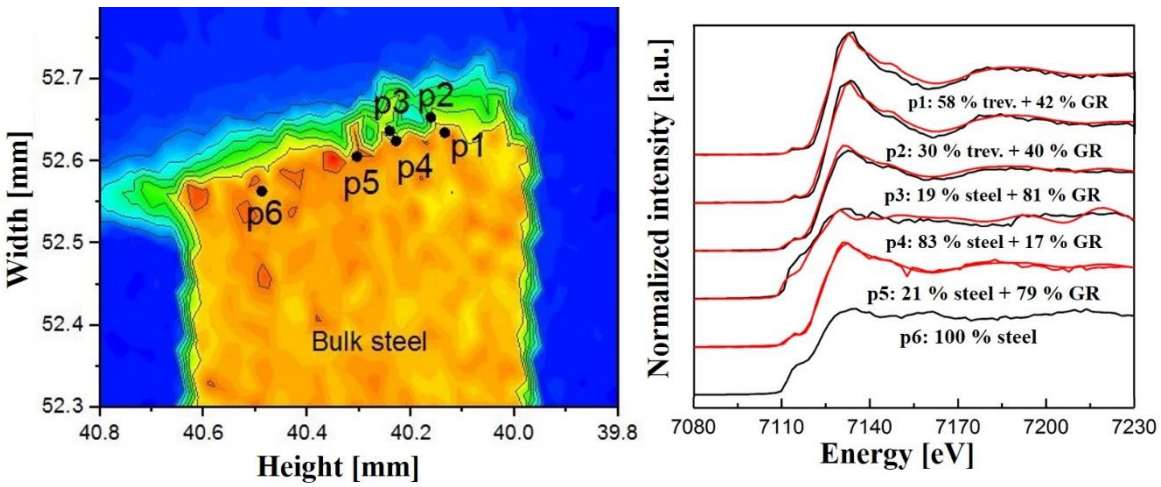

Figure 26. *Fe Kα intensity map (left) across the corroding interface for 309S contacted with 5 M NaCl for 31 weeks at 90°C. The map indicates the position of points of interest for probing the Fe K-edge by XAS (right). Black lines are experimental spectra, red lines are fits to experimental data using spectra recorded for the pristine steel, trevorite (trev., $NiFe_2O_4$) and chloride green rust (GR).*

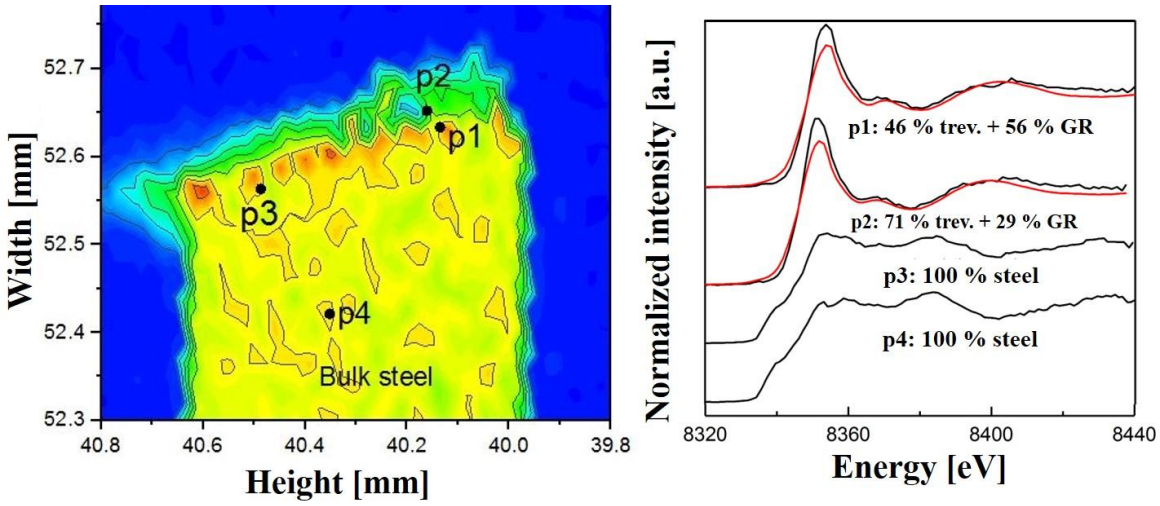

Figure 27. *Ni Kα intensity map (left) across the corroding interface for 309S contacted with 5 M NaCl for 31 weeks at 90°C. The map indicates the position of points of interest for probing the Ni K-edge by XAS (right). Black lines are experimental spectra, red lines are fits to experimental data using spectra recorded for the pristine steel, trevorite (trev., $NiFe_2O_4$) and Ni-doped chloride green rust (GR).*

Fits to the Fe *K*-edge µXANES revealed the presence of various compounds, such as chloride green rust and steel (points 3, 4 and 5), or green rust chloride and trevorite (points 1 and 2). Fits to the Ni *K*-edge µXANES were consistent with Fe *K*-edge data, namely the concomitant presence of Ni-doped green rust chloride and trevorite at points 1 and 2 (same positions as for Fe *K*-edge). Considering the proportions of each phase and their location in the corrosion layer, it can be concluded that green rust formed close to the steel while trevorite formed further away from the interface.

The upper right side of the sample was selected to obtain information on the elemental distribution and on the speciation of chromium (Figure 28). The concentration of chromium decreases from the bulk steel to the resin, and only pure Cr-containing compounds in various proportions were detected in the corrosion layer.

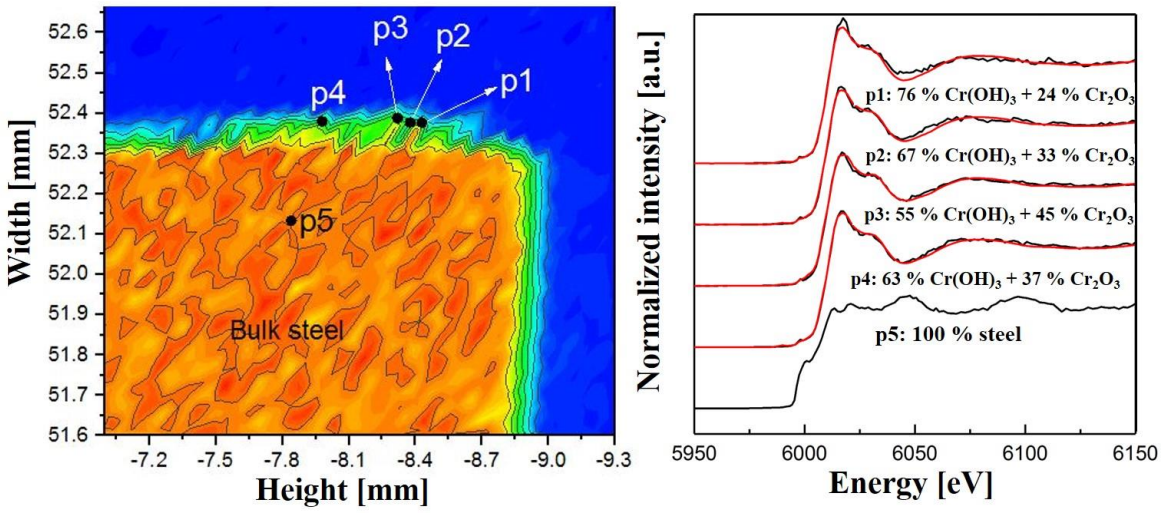

Figure 28. *Cr Kα intensity map (left) across the corroding interface for 309S contacted with 5 M NaCl for 31 weeks at 90°C. The map indicates the position of points of interest for probing the Cr K-edge by XAS (right). Black lines are experimental spectra, red lines are fits to experimental data using spectra recorded for the pristine steel, $Cr(OH)_3$ and Cr_2O_3.*

Complementary X-ray diffractograms were recorded [Morelová, 2020] on the upper right side of the sample from the corroded steel to the resin. No Fe- or Ni-bearing compound could be detected, only the presence of Cr_2O_3 was clearly evidenced, but no $Cr(OH)_3$ certainly due to the poor crystallinity. Results obtained by application of synchrotron-based methods suggest an evolution of the corrosion front, with the formation of doped green rust in the inner layer close to the steel surface, transforming into trevorite in the outer part. Cr-bearing compounds formed separately and were non-homogeneously distributed within the corrosion layer.

A thermodynamic model was developed for 309S contacting 5 M NaCl at 90°C. Pourbaix diagrams were calculated (Figure 29) using dissolved amounts of metal ions at 26 weeks (values after 13 and 26 weeks were very similar, dissolved amounts were below detection limits after 42 weeks). On the Pourbaix diagram with respect to iron, experimental conditions are at the border between aqueous $FeCl_2$ and the stability field of chromite ($FeCr_2O_4$). Unfortunately, this phase could not be detected by µXANES and XPS analysis hinted at the presence of Fe(III)-bearing phases. This mismatch remains unclear. On the Pourbaix diagram with respect to nickel, experimental conditions are in the aqueous Ni^{2+} region, close to the stability field of trevorite, and this phase was detected by µXANES. On the Pourbaix diagram with respect to chromium, the presence of Cr_2O_3 is expected, which agrees with experimental findings. These calculations need to be taken with care, as they were done using the SIT approach and the [TC] database,

and the ionic strength in the experiment is above the limit for this approach. Furthermore, because steel corrosion is a dynamical reaction, observed phases are not necessarily thermodynamically stable and mismatch with thermodynamic calculations can exist.

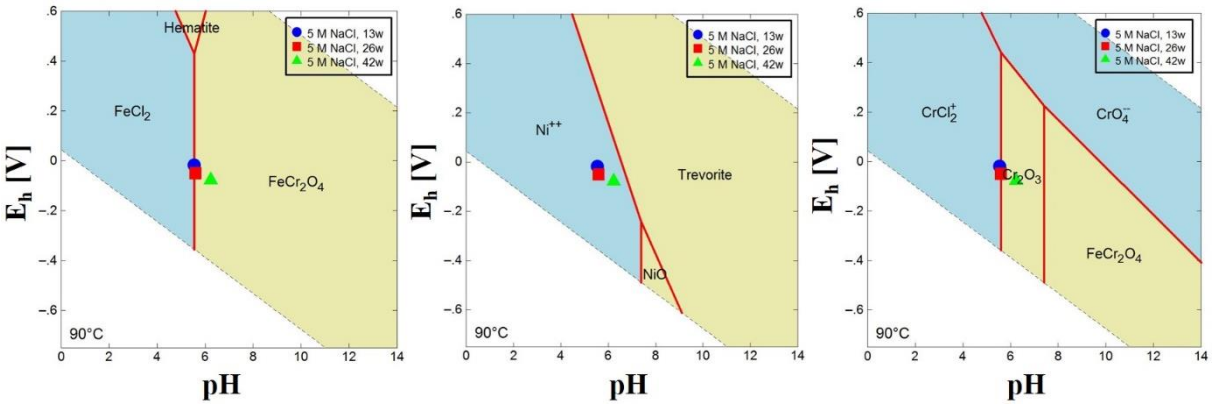

Figure 29. *Pourbaix diagrams for 309S contacting 5 M NaCl at 90°C drawn with respect to Fe (left), Ni (middle) and Cr (right) using amounts of dissolved elements after 26 weeks, the SIT approach and the [TC] database.*

In 0.1 M NaCl at 90°C after 28 weeks and in Solution 3 at 90°C after 26 weeks, a very thin and heterogeneous layer covered the surface [Morelová, 2020]. XPS analysis evidenced the presence of Fe(0), Fe(III), Ni(0), Ni(II) and Cr(III), comparable to findings obtained in 5 M NaCl at 90°C. EDX and XRD analyses only detected the presence of non-corroded steel. According to Pourbaix diagrams [Morelová, 2020] corresponding to Solution 3 at 90°C after 26 weeks with respect to iron and nickel, chromite and trevorite are thermodynamically stable phases, with XPS analysis favoring trevorite. Because of the presence of sulfate in this brine, pyrite would be stable under more reducing conditions, but is not expect to form under given experimental conditions.

In 5 M NaCl at 25°C after 49 weeks and in Solution 3 at 25°C after 20 and 26 weeks, no observable surface attack could be detected by SEM, XPS or XRD.

2. Corrosion in $MgCl_2$ brines

In 3.4 M $MgCl_2$ at 90°C, the evolution of the surface morphology is comparable to that in 5 M NaCl at 90°C, with the formation of a thin heterogeneous layer of corrosion products

[Morelová, 2020]. XPS analysis hinted at the presence of Cr(III) compound(s), along Fe(0) and Ni(0), while results from EDX and XRD analysis matched that of the non-corroded steel. A similar behavior was obtained for 3.4 M $MgCl_2$ at 25°C after 49 weeks and for 0.033 M $MgCl_2$ at 90°C after 28 weeks.

In Solution 1 at 25°C after 20 weeks, analyses point at the possible occasional presence of $MgFe_2O_4$ on the non-corroded surface. In the same brine at 90°C after 26 weeks, a likely pit initiation was observed with a precipitate in its vicinity. SEM and XPS analyses of this precipitate suggested the possible formation of chloride green rust, doped with Ni(II) and possibly Cr(III). Further away from the pit, XPS analysis evidenced the presence of Fe(0), Ni(0) and Cr(III). Interestingly, the analysis of the crosscut of this sample revealed the presence of a crack 1 mm in depth, evidencing stress corrosion cracking. It is very likely that the crack was initiated at the location of the pit during cutting. No other surface damage could be detected.

***Table 9**. Observed corrosion products formed by contacting 309S with various brines at 90°C and at 25°C.*

Brine	T [°C]	pH_M	E_h [mV]	Experimentally determined secondary phases
5 M NaCl	90	6.9±0.3	-77±50	Passive film composed of Cr_2O_3, $Cr(OH)_3$ and trevorite. Chloride green rust doped with Ni and Cr at the steel/film interface.
5 M NaCl	25	6.40±0.05	214±50	Cr_2O_3 and $Cr(OH)_3$ layer.
0.1 M NaCl	90	6.0±0.1	-64±50	Passive film composed of Cr_2O_3, $Cr(OH)_3$ and trevorite.
Solution 3	90	6.0±0.3	123±50	Passive film composed of Cr_2O_3, $Cr(OH)_3$ and trevorite.
Solution 3	25	6.70±0.05	91±50	Cr_2O_3 and $Cr(OH)_3$ layer.
3.4 M $MgCl_2$	90	5.6±0.5	98±50	Cr_2O_3 and $Cr(OH)_3$ layer.
3.4 M $MgCl_2$	25	7.26±0.05	202±50	Cr_2O_3 and $Cr(OH)_3$ layer.
0.033M $MgCl_2$	90	5.8±0.1	-42±50	Cr_2O_3 and $Cr(OH)_3$ layer.
Solution 1	90	6.1±0.5	98±50	Chloride green rust with Ni and Cr near starting pit. Cr_2O_3 and $Cr(OH)_3$ layer away from the pit.
Solution 1	25	7.66±0.05	50±50	Cr_2O_3 and $Cr(OH)_3$ layer. Possible $MgFe_2O_4$.

For this steel, either no surface damage or only a very thin layer of corrosion products was observed in NaCl and in $MgCl_2$ brines. Unfortunately, no reliable data are available for activity calculations using the Pitzer approach for Cr and Ni. However, given the comparable behavior of the steel in NaCl and in $MgCl_2$ brines, the formation of similar phases was assumed, with the onset of Ni(II) and Fe(III) phases likely shifting to higher pH_M value due to the high ionic strength of 3.4 M $MgCl_2$ compared to 5 M NaCl. The outcomes for this steel are summarized in Table 9.

v. Corrosion mechanism

At the surface of stainless steel, a protective layer of Cr_2O_3 is known to form instantaneously [McCafferty, 2010]. Indeed, the presence of Cr(III) at the surface of all coupons before immersion in brines was detected by XPS. Since this layer can be hydrated, Cr_2O_3 and $Cr(OH)_3$ are both always present in the passive film [Kirchheim et al., 1989; Zhu et al., 2015], in agreement with experimental findings.

Nickel present in the steel and located at the surface can be oxidized by water, similarly to iron (Eqs. 1 and 2). Because the solubility of nickel is higher than iron, amounts of dissolved nickel were larger than for iron in all systems.

Based on the composition of the steel, various oxides can form at the surface of corroding steel, such as spinel compounds, which are low soluble and corrosion resistant [Beverskog and Puigdomenech, 1999]. In this work, magnetite (Fe_3O_4), trevorite ($NiFe_2O_4$), chromite ($FeCr_2O_4$) and nichromite ($NiCr_2O_4$) are compounds likely to form, and some have been detected experimentally. Studies conducted either under acidic or in alkaline conditions reported that the passivation film has a double layer structure [Kirchheim et al., 1989; Ramya et al., 2010; Zhang et al., 2017], with an internal layer made of Cr-containing, and an outer layer made of Fe- and Ni-containing compounds possibly formed by dissolution-precipitation. It was also suggested [Zhang et al., 2017] that the film is composed of amorphous Cr_2O_3 covered by chromite ($FeCr_2O_4$) formed by reaction between $Fe(OH)_2$ and Cr^{3+}_{aq} (Eq. 8). Similarly, trevorite ($NiFe_2O_4$) can be formed by reaction between $Ni(OH)_2$ and Fe^{2+}_{aq} (Eq. 9). These reactions compete with the Schikorr reaction, but magnetite is less likely to form because of its lower stability [Beverskog and Puigdomenech, 1999]. The possible formation of spinel compounds of various compositions agrees with the observed heterogeneous composition of the passivation

films in this work. Note that the growth of the outer layer is governed by the stability of forming oxide phases.

$$Fe(OH)_2 + 2Cr_{aq}{}^{3+} + 6\,OH^- \leftrightarrow FeCr_2O_4 + 4H_2O \quad \text{(Eq. 8)}$$

$$Ni(OH)_2 + 2Fe_{aq}{}^{3+} + 6\,OH^- \leftrightarrow NiFe_2O_4 + 4H_2O \quad \text{(Eq. 9)}$$

The passive film is stable when the metal is in the passivation region. Considering pitting and corrosion potentials determined in this work by electrochemistry at 25°C, pitting corrosion would be expected to occur in all experiments performed in $MgCl_2$ brines. Unfortunately, the values of these potentials were not determined at 90°C, but they may likely be lower than at room temperature, suggesting that experiments performed in NaCl brines at 90°C may have reached the pitting potential. Unfortunately, pitting is a slow process and no pit formation could be detected, except for Solution 1 at 90°C after 26 weeks. In this experiment, after breakdown of the passive film, the metal around the pit was under cathodic control resulting in local high pH_M (water reduction) and local high chloride concentration. These conditions favored the formation of chloride green rust. In contrast, the pH_M decreased inside the pit due to cation hydrolysis (Eq. 11), favorable to pit growth and hindering re-passivation [Frankel, 1998].

$$FeCl_{2_{aq}} + H_2O \leftrightarrow Fe(OH)^+ + H^+ + 2Cl^- \quad \text{(Eq. 10)}$$

It is unclear whether the formed green rust would be stable under those conditions, or transform into more stable phases. Yet, at 90°C in 5 M NaCl, Fe and Ni *K*-edge µXANES indicated the presence of Ni-doped green rust covered by trevorite. Unfortunately, no pit could be detected in that sample by µXRF, certainly because of their small size. It is thus likely that the sample was at an early stage of pitting corrosion.

The pit initiation is sensitive to imperfections or cracks in the passive film, and thus it may vary from sample to sample. At 90°C in 5 M NaCl and in Solution 1 green rust formed, evidencing that the formation of the same phase was favored upon film penetration. The concentration of sulfate in Solution 1 was apparently too low to cause a shift in pitting potential [McCafferty,

2010] and it was also too low to favor the formation of sulfate over chloride green rust [Refait et al., 1997, 2003].

For this steel, spinel compounds such as trevorite and chromite, as well as Cr_2O_3 are quite stable compounds and may contribute on the long-term to radionuclide retention.

4. Actinide uptake by iron corrosion products under anoxic and low to high saline conditions

Corrosion products identified in steel corrosion experiments were selected to evaluate their retention properties towards actinides. In this project, trivalent radionuclides (Eu(III) and Am(III)) were either contacted with preformed phases in suspension, or present during the synthesis of corrosion products. All experiments were performed under anoxic and room temperature conditions, and in dilute to concentrated NaCl or $MgCl_2$ solutions.

a. Materials and methods

Mineral phases used in the uptake experiments were either synthesized or purchased. In all experiments, ultrapure water was used and reagents of ACS grade or higher.

i. Mineral phases

Magnetite has been synthesized [Cornell and Schwertman, 1996] earlier and kept as stock suspension under Ar. Two batches of iron hydroxychloride ($Fe_2(OH)_3Cl$) were used: the project partner (GRS Braunschweig) provided one batch and the second batch was synthesized at KIT-INE [Morelová, 2020]. Note that the Fe endmember was used in sorption studies, while in the compounds identified in corrosion studies Fe was partly replaced by Mg. Chloride green rust (GR-Cl, $Fe^{(II,III)}_4(OH)_8Cl{\cdot}nH_2O$) was prepared by direct precipitation from Fe(II) and Fe(III) salts. Trevorite ($NiFe_2O_4$) and chromium oxide (Cr_2O_3) were both purchased to perform sorption experiments. Before use in uptake experiments, all compounds were characterized using various microscopic and spectroscopic techniques to characterize the morphology, structure and surface properties [Morelová, 2020].

ii. Titration of mineral phases

The surface charge behavior of a solid in suspension as a function of pH is a critical input for surface complexation modeling. This information can be obtained by acid-base titration to determine the number of protons sorbed or desorbed by the surface as a function of pH. Protonation/deprotonation constants are obtained from data modelling. Because ionic strength affects the surface charge, a titration should be performed at each value of ionic strength. From

the five mineral phases selected only three of them were titrated ($NiFe_2O_4$, Cr_2O_3 and Fe_3O_4), mostly because of the very narrow pH stability range of iron hydroxychloride and chloride green rust.

Trevorite and chromium oxide were titrated using a titrator under humidified argon. The mineral phase was suspended in 0.1 M or 1.0 M NaCl, and 1 M NaOH was added to obtain starting alkaline conditions. Small aliquots of acid were added stepwise and the pH was recorded. The amount of protons consumed or released from the surface was calculated using the molar proton concentration and the known total proton concentration, and subsequently used to calculate the charge density [Lützenkirchen et al., 2012]. The blank, titrated under identical conditions but without mineral surface, was subtracted. Absolute values of relative surface charge as function of pH_M were obtained using the point of zero charge either taken from literature for $NiFe_2O_4$ (8.3 [Barale et al., 2008; Martin Cabanas et al., 2011]) Cr_2O_3 (7.9 [Blesa et al., 2000; Wiśniewska & Szewczuk-Karpisz, 2013]) and corrected for ionic strength, or measured independently for Fe_3O_4. Magnetite was titrated manually in the Ar box, following comparable procedure [Morelová, 2020]. The obtained point of zero charge (pH_M = 6.4) agreed with the independently measured isoelectric point and with reported values [Vidojkovic and Rakin, 2017].

iii. Eu(III)/Am(III) uptake

The uptake of europium by various solid phases was investigated in batch type experiments for various NaCl or $MgCl_2$ concentrations under anoxic conditions [Morelová, 2020]. The percentage of sorbed Eu and solid-liquid distribution coefficients (K_D values) were obtained as a function of pH_M at fixed Eu concentrations (5.1×10^{-10} M, 1×10^{-7} M, and 1×10^{-5} M). The pH_M range was chosen to avoid dissolution of the mineral phase and precipitation of Eu solid phase(s). The solid was first equilibrated with the background electrolyte for 24 h, then a pH buffer (MES, MOPS, TRIS) was added to reach 20 mM in solution before europium was added after further 5 h of equilibration. At the lowest Eu concentration, only active Eu was used (stock solution of dissolved $EuCl_3$ obtained from Eckert & Ziegler Nuclitec with a composition of >95 % ^{152}Eu ($t_{1/2}$ = 13.5 y), 3.76 % ^{153}Gd and 0.55 % ^{154}Eu, and an activity of 1×10^4 MBq/L on 15.03.2016). At higher concentration, it was mixed with an inactive solution prepared by dissolving Eu_2O_3 in HCl. After the desired contact time, the suspension was ultracentrifuged (Beckman Coulter XL-90 K) at 90,000 rpm (~700,000 *g*) for 30 minutes. An aliquot of the supernatant was acidified before quantification using a gamma counter (Packard Cobra Auto-

Gamma 5003). The amount of dissolved Cr/Fe/Ni in the supernatant was quantified by HR-ICP-MS. A kinetic study showed that equilibrium sorption was reached within 24 h for magnetite, green rust and chromium oxide, and 72 h for trevorite and iron hydroxychloride. Sorption isotherms were also determined for magnetite following similar procedure, at pH_M ~6 and ~7, at constant m/V = 0.5 g/L, for *I* = 0.96 M, 2.9 M and 4.8 M NaCl for Eu concentrations ranging from 1×10^{-4} M to 5.1×10^{-10} M. Finally, americium was also contacted with magnetite to prepare samples for XAS experiments to provide information on the binding mode at the surface.

iv. X-ray absorption spectroscopy

Molecular-scale information on the americium binding mode to the surface was provided by X-ray absorption spectroscopy at the INE-Beamline for actinide research [Rothe et al., 2012] at the KIT synchrotron light source (Karlsruhe, Germany). Information on potential effects of ionic strength and retention mechanism was used to build a surface complexation model.

Samples were prepared by contacting Am (7.8×10^{-6} M) with magnetite (m/V = 1 g/L) at pH_M of 6.1 and ~7.1 at *I* = 0.95 M NaCl and 4.7 M NaCl. The equilibrated sample was centrifuged, the wet paste transferred into a vial, which was sealed and mounted inside a tight cell. The sample preparation took place in the Ar box. At the beamline, the energy of the incoming beam was calibrated using a Zr foil. Am L_3-edge spectra were recoded under anoxic conditions in fluorescence-yield mode. Data were treated following standard procedures using Athena and Artemis interfaces to the Ifeffit software [Ravel and Newville, 2005].

b. Solubility and speciation of Eu and Am in dilute to concentrated NaCl and $MgCl_2$ solutions

Prior to the experiments, saturation indices of relevant Eu and Am solid phases were calculated as a function of pH_M and for various ionic strengths [Morelová, 2020] using either the SIT approach with [TC] for 0.1 M and 1.0 M NaCl or the Pitzer approach with [TPA] at ionic strengths of 4.7 M and higher. Calculations were performed for various Eu and Am concentrations in NaCl and $MgCl_2$ brines used in batch sorption studies and in samples prepared for XAS measurements. All uptake experiments were performed to avoid the precipitation of any solid Eu or Am phase.

Europium and americium speciation diagrams were calculated for NaCl brines [Morelová, 2020]. Using the SIT approach with [TC], predominant species in acidic-neutral pH_M range are Eu^{3+} for low ionic strength and Eu^{3+}, $EuCl^{2+}$ and $EuCl_2^+$ for high ionic strength. In the alkaline pH_M region, hydroxo species take over speciation. A similar behavior is observed for americium. Speciation curves in $MgCl_2$ brines follow identical patterns as in NaCl brines, as long as the ionic strength is the same.

c. Eu/Am adsorption to preformed corrosion products

i. Magnetite

1. Solid phase titration in dilute to concentrated NaCl solutions

Titration data were modeled using a modified version of FITEQL2. The CD-MUSIC model was used to predict proton binding constants for the various terminal oxygen sites. Capacitance values and binding constants for Na^+ and Cl^- to differently coordinated sites were obtain from the fit, using input data from Vayssières [1995] for the (111) plane of magnetite. The number of adjustable parameters was reduced by considering equal the binding constants of Na^+ and Cl^- to non-charged surface hydroxyl groups. The (111) plane of magnetite has two different surface terminations, the pK values and the surface charge calculated from bond valence are shown in Table 10.

Contributions from each termination were adjusted to retrieve the experimental point of zero charge. Experimental and modeled titration data for magnetite in 0.1 M and 1.0 M NaCl are shown in Figure 30. The point of zero charge $pH_M = 6.4$ agrees with literature data [Vidojkovic and Rakin, 2017]; best model parameters are shown in Table 11. The simplest model in terms of number of adjustable parameters was obtained when constraining intrinsic ion binding constants for singly and triply coordinated sites to be identical, with a separate value for the doubly coordinated sites. Ion binding on these sites is weak, and thus ions prefer binding to singly/triply coordinated sites. The overall Stern capacitance value of 1.32 F/m^2 is within the range of overall capacitance for metal (hydr)oxides reported by Hiemstra and Van Riemsdijk [1991] for non-porous and well-ordered planar crystal faces ranging from 0.9 to 1.7 F/m^2.

***Table 10**. pK values and surface charge calculated from bond valence for each coordination in the two terminations of the magnetite (111) plane [Vayssières, 1995].*

Mixed octahedral and tetrahedral termination			
Coordination of oxo/hydroxo groups	Reaction	pK	Surface charge calculated from bond valence
doubly	$Fe_2 - O^{-0.83} + H^+ \rightleftharpoons Fe_2 - OH^{0.17}$	9.3	-0.83
doubly	$Fe_2 - OH^{0.17} + H^+ \rightleftharpoons Fe_2 - OH_2{}^{1.17}$	-5.1	0.17
singly	$Fe_1 - O^{-1.25} + H^+ \rightleftharpoons Fe_1 - OH^{-0.25}$	17.5	-1.25
singly	$Fe_1 - OH^{-0.25} + H^+ \rightleftharpoons Fe_1 - OH_2{}^{0.75}$	3.6	-0.25
Octahedral termination			
Coordination of oxo/hydroxo groups	Reaction	pK	Surface charge calculated from bond valence
doubly	$Fe_2 - O^{-1.16} + H^+ \rightleftharpoons Fe_2 - OH^{-0.16}$	16.4	-1.16
doubly	$Fe_2 - OH^{-0.16} + H^+ \rightleftharpoons Fe_2 - OH_2{}^{0.84}$	2.5	-0.16
triply	$Fe_3 - O^{-0.75} + H^+ \rightleftharpoons Fe_3 - OH^{0.25}$	7.6	-0.75

Capacitance values and binding constants within the triple layer model were subsequently held fixed. For the radionuclide uptake, reactions with surface groups were defined. Activity coefficients of Eu species in solutions were also considered. The dielectric constant of aqueous solutions was calculated for each ionic strength and used for the diffuse part of the triple layer model. The model was then run in various site configurations until a good fit to experimental uptake data was achieved.

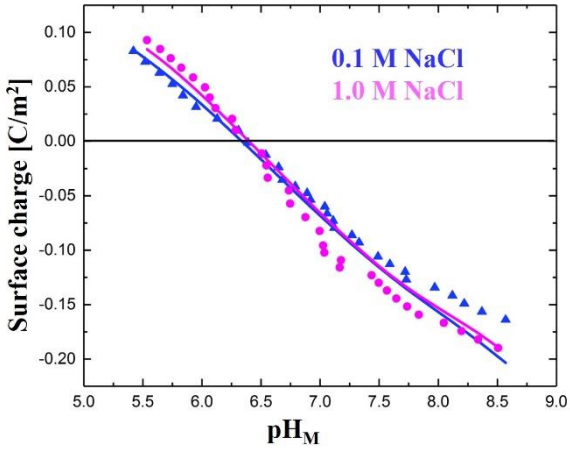

***Figure 30.** Experimental (symbols) and modeled (lines) surface charge of magnetite in 0.1 M NaCl and 1.0 M NaCl. Fit results are shown in Table 11.*

Table 11. *CD-MUSIC model parameters used for modeling the magnetite surface charging curves shown in Figure 30.*

Capacitance 1	3.22	F/m^2
Capacitance 2	2.25	F/m^2
Overall Stern capacitance	1.32	F/m^2
Constant for Cl^- and Na^+ binding to doubly coordinated hydroxyl sites, log K_a	-5.01	-
Constant for Cl^- and Na^+ binding to singly/triply coordinated hydroxyl sites, log K_e	2.45	-
Site densities used in optimization		
Doubly coordinated octahedral termination	6.68	$sites/nm^2$
Triply coordinated octahedral termination	2.23	$sites/nm^2$
Singly coordinated mixed termination	1.48	$sites/nm^2$
Doubly coordinated mixed termination	4.45	$sites/nm^2$

2. pH dependent Eu uptake in dilute to concentrated NaCl and $MgCl_2$ solutions

At the lowest concentration, europium is strongly retained by magnetite, with an uptake >99 % at $pH_M > 6.2$ (Figure 31). At $pH_M < 6.2$ the uptake decreases with increasing ionic strength. These findings agree with reported data of Singh et al. [2009] who observed quantitative sorption of Eu (2×10^{-9} M) onto magnetite at $pH_M > 5.5$ in 0.1 M $NaClO_4$, though using magnetite (2 g/L) of specific surface area higher than in this project. At 1×10^{-5} M, the uptake was low at pH_M 5.5, but increased with pH to reach quantitative uptake at $pH_M \geq 8.0$ for all salt concentrations. At this Eu concentration, the log K_D values increased from 2.7±0.2 at 20±4 % sorption to 4.6±0.2 at 95±4 %. Here also, the observed pH dependent sorption agrees with reported studies [Catalette et al., 1998].

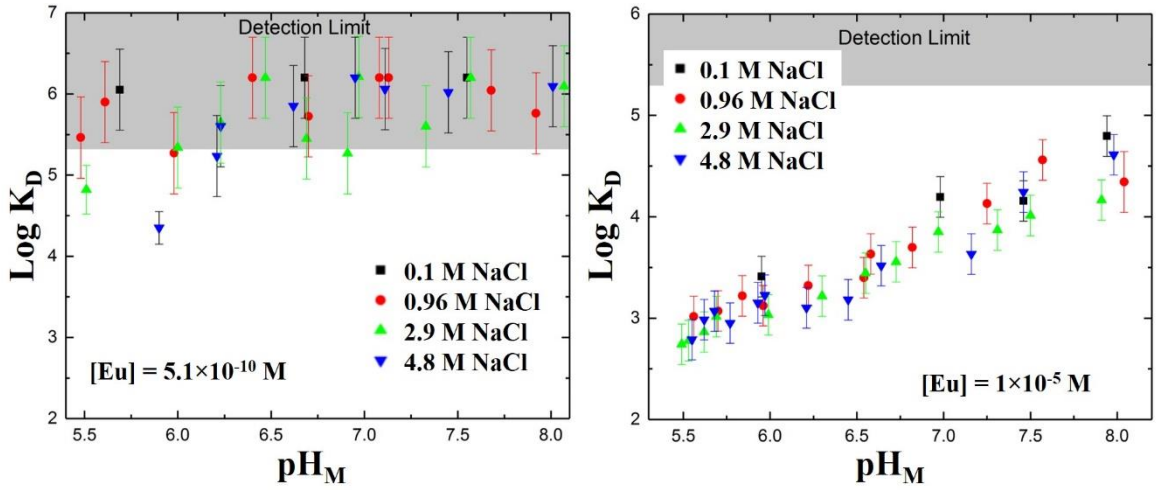

Figure 31. *Uptake of Eu (left: 5.1×10^{-10} M; right: 1×10^{-5} M) by magnetite (m/V = 0.5 g/L) as a function of pH_M at different NaCl ionic strengths under anoxic and room temperature conditions.*

At the lowest Eu concentration, the uptake by magnetite at I = 0.1 M $MgCl_2$ is comparable to that at I = 0.1 M NaCl (data not shown). At 10^{-5} M Eu (Figure 32), the decrease in sorption with increasing ionic strength in $MgCl_2$ solutions is more evident than in NaCl solutions. The uptake decreased by ~15 % from I = 0.95 M $MgCl_2$ to I = 2.85 M $MgCl_2$. Further increasing the ionic strength to 9.77 M, which becomes relevant for Mg-rich brines in rock salt formations, resulted in a significant decrease in Eu retention. At this salt content, the Eu uptake competes with Mg uptake and the surface screening increases thereby lowering the affinity for Eu.

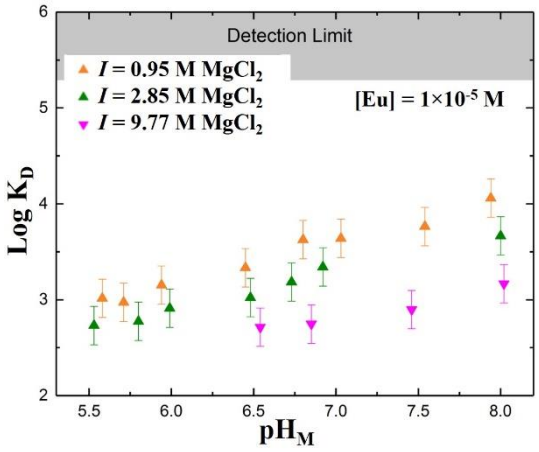

Figure 32. *Uptake of Eu (1×10^{-5} M) by magnetite (m/V = 0.5 g/L) as a function of pH_M at different $MgCl_2$ ionic strengths under anoxic and room temperature conditions.*

During Eu(III) sorption, magnetite dissolved marginally (Figure 33). The observed increase in dissolved iron corresponds to preferential release of Fe^{2+} from the surface. This effect is higher in $MgCl_2$ than in NaCl solutions and is pH dependent. Experimental results agree with reported data [Missana et al., 2003] and GWB modelling [Morelová, 2020].

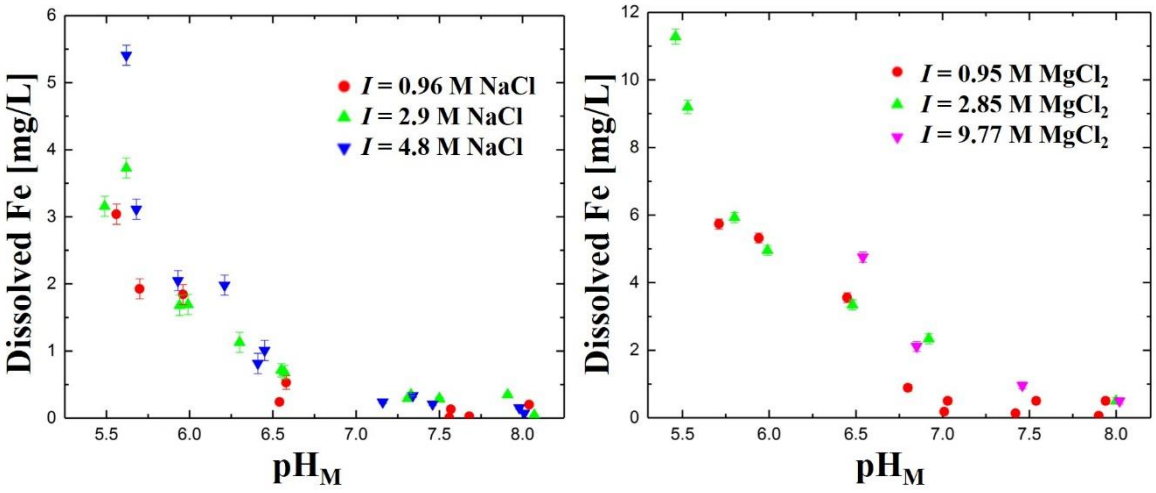

Figure 33. *Dissolved iron contents during Eu sorption experiments to magnetite in NaCl (left) and in $MgCl_2$ (right) solutions.*

3. Eu sorption isotherms in concentrated NaCl solutions

Eu sorption isotherms were performed at pH_M ~6.0 and ~7.0 for an Eu concentration varying from 10^{-10} M to 10^{-4} M at various ionic strengths set by NaCl (Figure 34). All isotherms exhibit a linear behavior, hinting at the presence of only 1 strong sorption site group. No effect of ionic strength is visible until 10^{-5} M where a slight deviation can be observed.

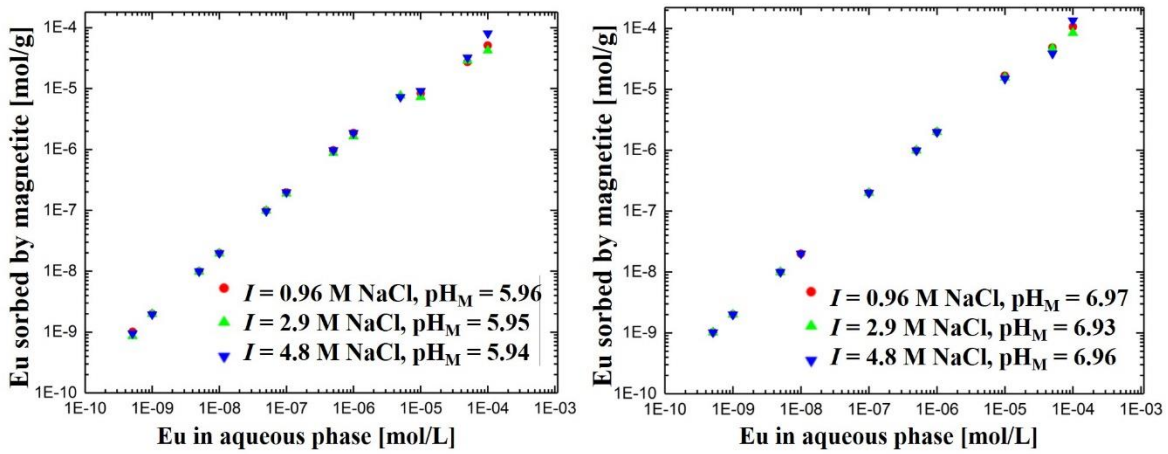

Figure 34. *Sorption isotherms of Eu to magnetite (0.5 g/L) at pH_M ~6 and pH_M ~7 at various ionic strengths set by NaCl.*

4. Structure of sorbed Am surface species by XAS

For this XAS study, 4 sorption samples were prepared and the Am(III) aqueous ions recorded as reference compound. The spectrum of the aqueous ions exhibits a single wave of decreasing amplitude, whereas that of sorption samples have lower oscillation amplitude and differ in the amplitude maximum at k ~5 Å^{-1} (Figure 35). The corresponding Fourier transforms (FT) differ accordingly. The most significant difference is the contribution at $R + \Delta R$ ~3 Å for the sorption samples which is absent in the FT of the aqueous ions. The FT of all sorption samples are very similar, suggesting comparable structure. Aqueous speciation calculations indicated that the dominant species do not vary between all applied chemical conditions, further suggesting comparable structure.

For the aqueous ions, fit to the data yielded 9 oxygen atoms at d(Am-O) = 2.44 Å (Figure 35 and Table 12), in agreement with earlier findings [Finck et al., 2015; Skerencak-Frech et al., 2014]. In the sorption samples, Am is bound to 9 O atoms at 2.48-2.53 Å, with the additional presence of 3 Fe atoms at 3.49-3.54 Å. These data evidence structural binding of Am to the magnetite surface, via 3 O atoms to three edge-sharing FeO_6, and the 6 remaining O atoms belonging to bound water molecules. This configuration is similar to that reported for Am sorbed to magnetite at lower ionic strength [Finck et al., 2016a, 2016b] highlighting the negligible effect of ionic strength on the nature of the sorbed species, which agrees with the low effect of I on Eu sorption. Interestingly, this configuration is also comparable to that of Pu(III) sorbed to magnetite in 0.1 M NaCl [Kirsch et al., 2011]. No neighboring Am was detected,

ruling out the formation of polymers. Adding Cl did not improve the fit, ruling out a surface chloro complex. Am incorporation into the magnetite structure was also ruled out [Finck et al., 2016a].

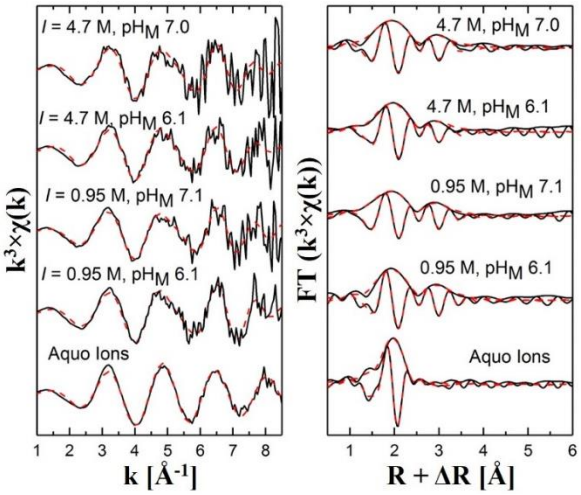

Figure 35. *Experimental (solid black lines) and modeled (red dashed lines) Am L_3-edge EXAFS spectra (left) of the sorption samples at various pH_M and NaCl concentrations, and of the Am^{3+} aqueous ions, with the corresponding Fourier transforms (right).*

Table 12. *Best-fit results from fits to the Am L_3-edge EXAFS data for the Am sorption samples and the Am^{3+} aqueous ions (S_0^2 = 0.87).*

Sample	FT range [Å^{-1}]	Fit range [Å]	Shell	N	*d* [Å]	σ^2 [Å^2]	ΔE_0 [eV]	R_f (×10^2)
***I* = 4.7 M, pH_M = 7.0**	3.2-7.7	1.3-3.3	O1 Fe1	9.9(6) 2.9(6)	2.49 3.54	0.015 0.007	1.9(0.5)	0.19
***I* = 4.7 M, pH_M = 6.1**	3.3-8.0	1.4-3.3	O1 Fe1	9.6(9) 2.5(9)	2.53 3.54	0.013 0.008	2.5(2.1)	0.18
***I* = 0.95 M, pH_M = 7.1**	3.2-7.8	1.3-3.5	O1 Fe1	9.9(7) 3(2)	2.48 3.49	0.016 0.006	0.1(1.1)	0.19
***I* = 0.95 M, pH_M = 6.1**	3.2-8.2	1.5-3.5	O1 Fe1	8.9(6) 3.1(5)	2.51 3.53	0.011 0.006	1.8(1.3)	0.13
Am^{3+} ions	3.2-10.3	1.7-2.6	O1	9.0	2.44	0.008	1.2(1.4)	0.21

FT range: Fourier transformed range, N: coordination numbers, d: interatomic distance, σ^2: Debye-Waller factor, ΔE_0: shift in ionizing energy with E_0 taken as maximum of the first derivative, R_f: figure of merit of the fit. Estimated uncertainties on d are ±0.03 Å and are ±0.001 Å^2 on σ^2.

5. Surface complexation model

The surface complexation model used input from the solid phase titration, the aquatic speciation of Eu/Am and outcomes from XAS, assuming that europium sorption follows closely americium sorption. The charge distribution in the Am surface complex was formulated such as three O atoms bond the surface and six were split between the 0 and b plane.

A poor fit was obtained using singly coordinated sites, which was contrary to expectations as titrations experiments showed these to be dominant proton sorption sites. The best fit was obtained using only doubly coordinated sites, with a satisfactory fit for both terminating hydroxyl groups. XAS suggested that binding occurred at octahedral terminations, matching well the reported structure of octahedral termination [Vayssières, 1995] allowing Am to be located close to three Fe atoms at the same distance. Results from sorption data modeling are shown in Figure 36, with surface complexes and complexation constants at infinite dilution shown in Table 13. Subtracting log K_1 from log K_2 results in the constant of the hydrolysis reaction of the magnetite sorbed Am(III) surface complex. The difference of 7.7 is close to log K of the hydrolysis of Am in solution (7.2), showing that values are realistic.

$$S_0{:}\,(Fe_2 - OH^{-0.16})_3 + Am^{3+} \leftrightharpoons \{(Fe_2 - OH^{-0.16})_3 Am^{3+}\} \qquad log\ K_0$$

Transfer of charge: $\Delta z_0 = 1.5$, $\Delta z_\beta = 1.5$

$$S_1{:}\,(Fe_2 - OH^{-0.16})_3 + Am^{3+} \leftrightharpoons \{(Fe_2 - OH^{-0.16})_2\,(Fe_2 - O^{-1.16})Am^{3+}\} + H^+ \qquad log\ K_1$$

Transfer of charge: $\Delta z_0 = 0.5$, $\Delta z_\beta = 1.5$

$$S_2{:}\,(Fe_2 - OH^{-0.16})_3 + Am^{3+} + H_2O \leftrightharpoons \{(Fe_2 - OH^{-0.16})_2 (Fe_2 - O^{-1.16}) Am(OH)^{2+}\} + 2H^+ \qquad log\ K_2$$

Transfer of charge: $\Delta z_0 = 0.5$, $\Delta z_\beta = 0.5$

Table 13. *Complexation constants for Eu/Am sorption to magnetite at infinite dilution.*

$\boldsymbol{log\ K_0}$	6.9 ± 0.1
$\boldsymbol{log\ K_1}$	0.2 ± 0.1
$\boldsymbol{log\ K_2}$	-7.5 ± 0.1

The aquatic speciation showed the presence of $EuCl^{2+}$/$AmCl^{2+}$ in significant proportions, but do not contribute to the surface complexation in significant proportions, which is corroborated by the satisfactory fit without using an Am-Cl complex $\{(\ Fe_2 - OH^{-0.16}\ )_3 Am\ Cl\}$. The model was able to capture the pH_M dependent sorption data (Figure 36) as well as the isotherms (Figure 37). The distribution of surface complexes is affected by the ionic strength. At [Eu] = 10^{-5} M, though the distribution trend is the same, the dominance of each is shifted to higher pH_M with increasing ionic strength. At [Eu] = 5.1×10^{-10} M the distribution differs, with S_0 dominating up to pH_M 7.6 at low ionic strength, and dominating over the whole pH_M range at higher ionic strength (data not shown). At higher ionic strength, the electrolyte interacts with the surface and competes with Eu, and this becomes notable at higher Eu concentration. At lower Eu concentration, the competition is minor. Overall, data reflect a high affinity of magnetite for trivalent actinides, rendering this phase a candidate for strong radionuclide retention in dilute to concentrated NaCl brines in the near-field of a DGR.

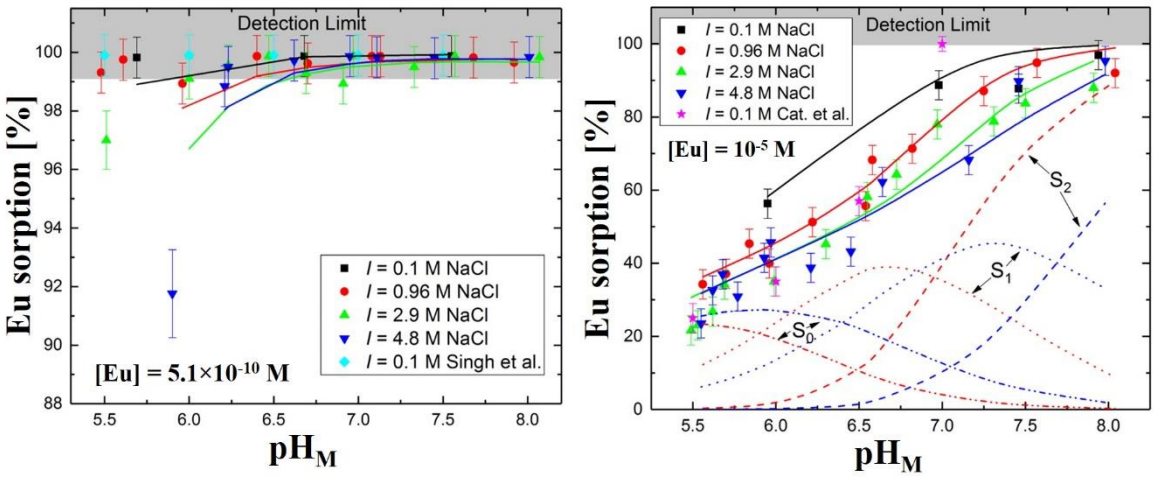

Figure 36. *pH_M dependent Eu sorption (left: [Eu] = 5.1×10^{-10} M; right: [Eu] = 1×10^{-5} M)) onto magnetite at various ionic strengths. Experimental (symbols) and modelled (solid lines) data obtained using surface complexation model in FITEQL with the Pitzer approach and [TPA]. The distribution of the three complexes are represented by red (I = 0.96 M) and blue (I = 4.8 M) dashed lines. (Singh et al. [2009]; Cat. et al.: [Catalette et al., 1998]).*

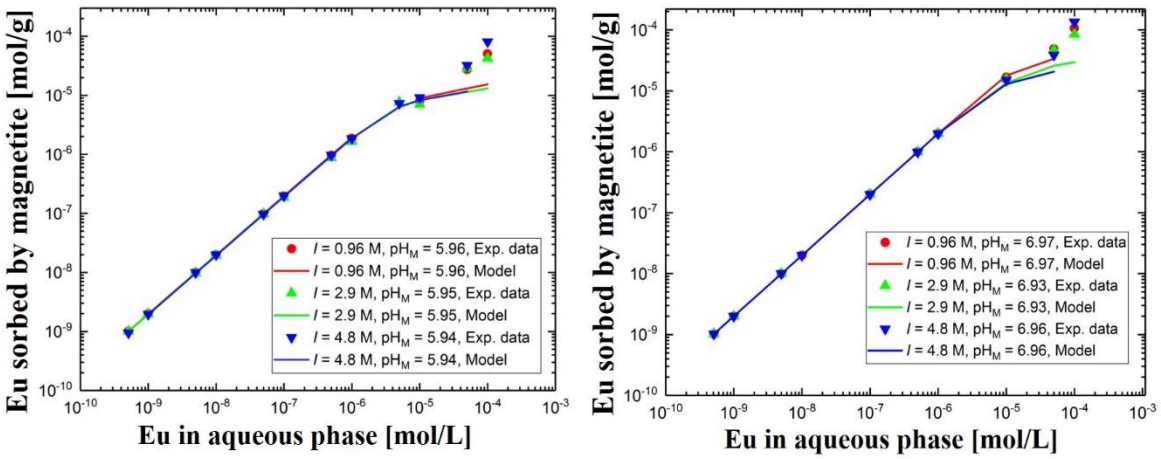

Figure 37. *Sorption isotherms of Eu onto magnetite at pH_M ~6.0 (left) and at pH_M ~7.0 (right) at various ionic strengths. Experimental (symbols) and modelled (solid lines) data using surface complexation model in FITEQL with the Pitzer approach and [TPA] database.*

ii. Iron hydroxychloride

The stability of this compound is restricted to a relatively narrow pH range [Réguer et al., 2005]. The select pH_M range for sorption experiments in this project was 6.7 – 9.0. The quantification of dissolved Fe present in the supernatant revealed a significant dissolution (nearly half of the introduced compound) in the pH_M range 6.8 – 7.8, in both NaCl and $MgCl_2$ solutions [Morelová, 2020]. Values of dissolved Fe reach 300 mg/L, which may result in the precipitation of magnetite, according to geochemical calculations.

At [Eu] = 5.1×10^{-10} M, the uptake was >96 % in the investigated pH_M range at all ionic strengths (Figure 38). Resulting values are close to the analytical detection limit and given their associated uncertainties, no effect of ionic strength on the sorption can be evidenced. The dissolution seems not to affect the retention, because the remaining solid (possibly mixed with magnetite) seems enough to sorb the introduced europium. At [Eu] = 1×10^{-7} M, the uptake first decreases and then increases with increasing pH_M. This behavior may be related to dissolution and uptake of Fe(II) competing with Eu(III). Once dissolution decreases, the Eu uptake increases with pH_M. No obvious ionic strength effect could be observed at this Eu concentration.

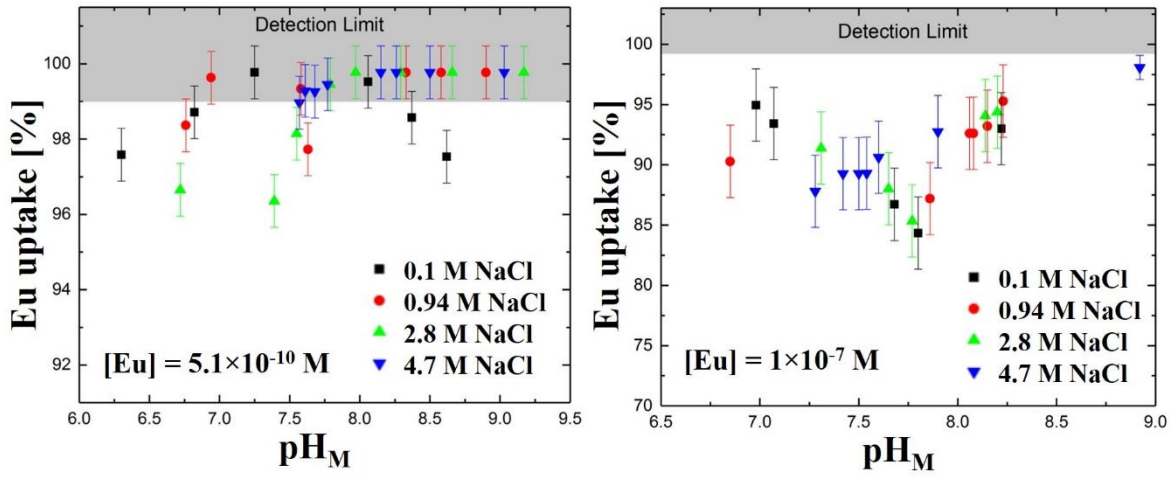

Figure 38. *Europium uptake (left: [Eu] = 5.1×10^{-10} M; right: [Eu] = 1×10^{-7} M) by iron hydroxychloride (m/V = 1 g/L) at different ionic strengths of NaCl.*

At an ionic strength of 0.1 M $MgCl_2$ and [Eu] = 5.1×10^{-10} M the uptake behavior was comparable to that in NaCl at the same ionic strength (Figure 39). With increasing ionic strength, the uptake decreased with increasing pH_M. This behavior differed from that in NaCl and was quite unexpected. A comparable behavior, as a function of pH_M and ionic strength, was observed at an europium concentration of 1×10^{-7} M (Figure 39). The possible alteration of the solid phase, an uptake during dissolution-recrystallization, or the formation of another phase scavenging Eu was not further investigated.

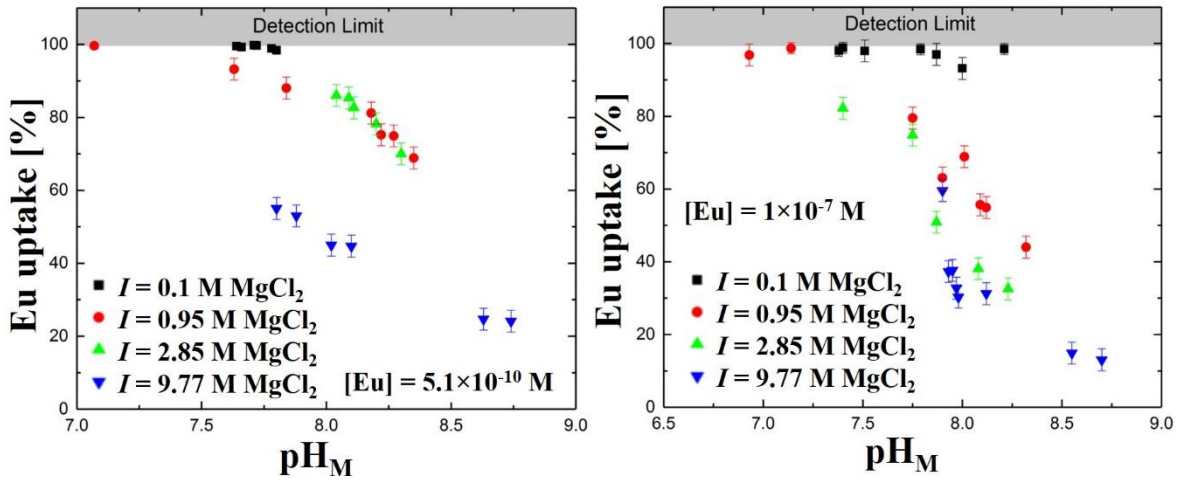

Figure 39. *Europium uptake (left: [Eu] = 5.1×10^{-10} M; right: [Eu] = 1×10^{-7} M) by iron hydroxychloride (m/V = 1 g/L) at different ionic strengths of $MgCl_2$.*

The uptake of Eu(III) can possibly be affected by concurrent Mg(II) uptake. Dzombak and Morel [1990] reported a high uptake of divalent Ca and Sr by hydrous ferric oxide already at low concentration (10^{-7} M). In this project, the higher Mg concentration and the higher hydrolysis tendency of Mg compared to Ca and Sr can easily explain the observed decreasing Eu uptake trend with increasing $MgCl_2$ concentration. No sorption model was developed because the sorption behavior is not well enough understood at present.

iii. Chloride green rust (GR-Cl)

Green rust is stable under reducing conditions in a narrow pH range. The selected pH_M range was 7.0 – 9.0. In this range, europium was quantitatively retained by the solid phase in dilute to concentrated NaCl solutions, at [Eu] = 5.1×10^{-10} M and [Eu] = 1×10^{-7} M (Figure 40). The amounts of dissolved Fe increased for decreasing pH_M and with increasing ionic strength [Morelová, 2020]. The uptake did not show any pH dependence, and hence no effect of dissolved Fe.

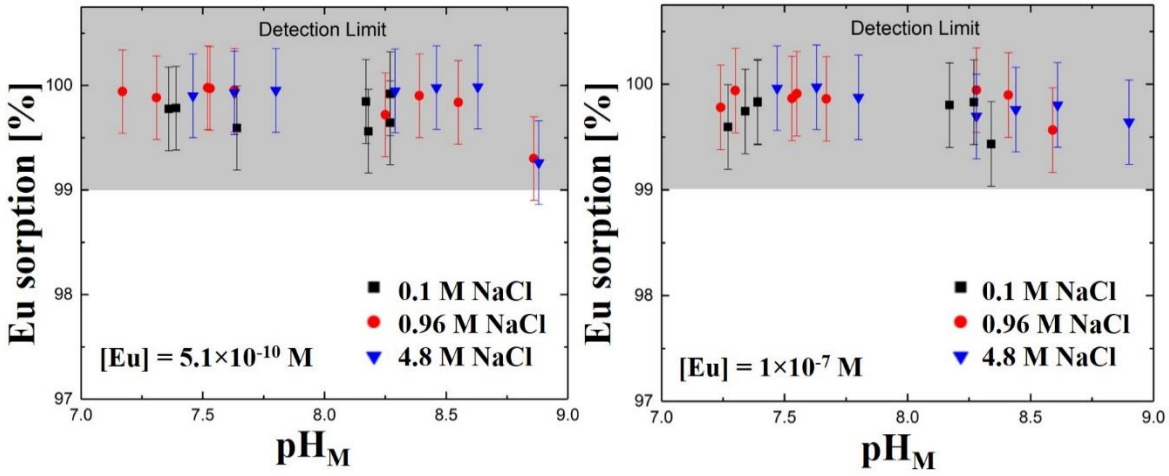

Figure 40. *Europium sorption (left: [Eu] = 5.1×10^{-10} M; right: [Eu] = 1×10^{-7} M) to chloride green rust (m/V = 1 g/L) at various ionic strengths of NaCl.*

This brief study does not allow deriving a detailed mechanistic model, but it shows that GR-Cl is a strongly sorbing solid in dilute to concentrated NaCl solutions. Unfortunately, not many studies reporting uptake of actinides by green rust compounds can be found in the literature,

but it has been shown that they can rapidly and efficiently reductively immobilize both dissolved U(VI) [Latta et al., 2015] or Np(V) [Bach et al., 2014] present in solution.

iv. Trevorite ($NiFe_2O_4$)

1. Solid phase titration in dilute to concentrated NaCl solutions

Trevorite is isostructural with magnetite, but no detailed structural information was available for this compound. A sorption model was thus developed considering a generic site and a site density of 10 sites/nm^2. Titration data were modeled using an approach similar to that used for magnetite, experimental and modeled data are shown in Figure 41. A point of zero charge of 8.3 was obtained, in agreement with reported data [Barale et al., 2008; Martin Cabanas et al., 2011]. Capacitance values are comparable to that of magnetite and the ion pair formation constants are similar, with a slightly weaker binding affinity for cations (Table 14). Note that the shape of the modeled titration curve is linear because of the one-step protonation process.

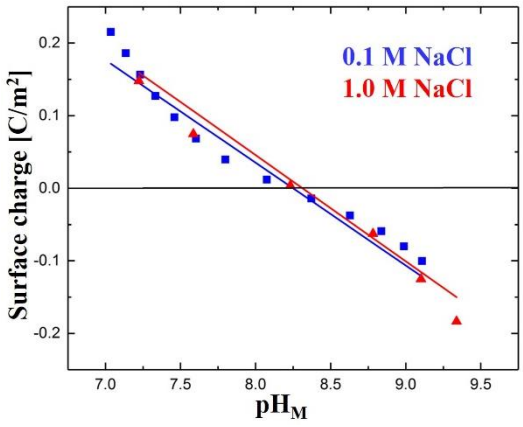

Figure 41. *Experimental (symbols) and modeled (solid lines) pH_M dependent charging behavior of trevorite at two ionic strengths of NaCl. Numerical values are shown in Table 14.*

Table 14. *CD-MUSIC model parameters used for modeling the trevorite surface charging curves shown Figure 41.*

Capacitance 1	3.07	F/m^2
Capacitance 2	2.34	F/m^2
Overall Stern capacitance	1.33	F/m^2
Constant for Cl^- binding, log K_a	0.63	-
Constant for Na^+ binding, log K_c	0.5	-

2. pH dependent Eu uptake in dilute to concentrated NaCl solutions

Europium sorption experiments were performed under conditions comparable to that of magnetite to allow direct comparison. At [Eu] = 5.1×10^{-10} M, the uptake is nearly quantitative at $pH_M \geq 6.2$ for all ionic strengths (Figure 42), whereas a clear effect of the salt content on the sorption is visible at $pH_M \leq 6.2$. At [Eu] = 1×10^{-5} M, the sorption is pH dependent, and a small ionic strength effect on the sorption is observed at lower pH_M values. The dissolution of the solid phase during sorption experiments was negligible [Morelová, 2020]. The europium uptake behavior of trevorite at both concentrations is comparable to that of magnetite, suggesting a negligible effect of the Fe(II) substitution by Ni(II) and thus a similar surface reactivity of both compounds. The observed slightly weaker uptake by trevorite may be attributed to differences in points of zero charge (6.4 for Fe_3O_4, 8.3 for $NiFe_2O_4$).

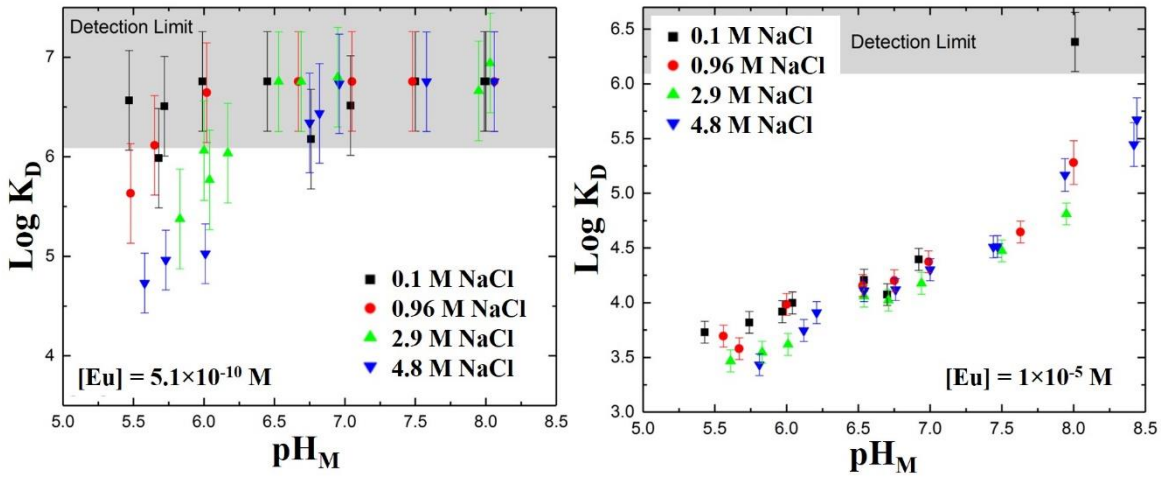

Figure 42. *Europium sorption (left: [Eu] = 5.1×10^{-10} M; right: [Eu] = 1×10^{-5} M) to trevorite (m/V = 0.08 g/L) at various ionic strengths of NaCl.*

3. Surface complexation model

Sorption data were modeled using a surface complexation model very similar to that of Eu/Am sorption to magnetite. The formation of a tridentate surface complex was assumed, which still needs to be determined experimentally, and the quality of the fit was not as good as for magnetite because of lack of information on that solid. Unfortunately, the model was not able to model sorption data at both europium concentrations: it overestimates the sorption at low

ionic strength and slightly underestimates at high ionic strength (Figure 43). This could be improved by implementation of more structural and electrostatic information on the solid phase.

Despite similarity in uptake data, complexation constants significantly differ. This result can be attributed to the use of different models, the lower uptake by trevorite, or the potential competition of dissolved Fe and Ni with Eu(III) for sorption. At I = 0.1 M, S_0 prevails up to pH_M 7.4, above which S_2 is dominant, while S_1 does not contribute much over the whole pH_M range. At I = 4.8 M, S_0 is dominant over the whole pH_M range. The small observed ionic strength effect can be attributed to competition of ions from electrolytes with Eu(III) for sorption to the surface. Data show that trevorite seems to be a strongly sorbing solid under conditions representative of a near-field repository in salt rock.

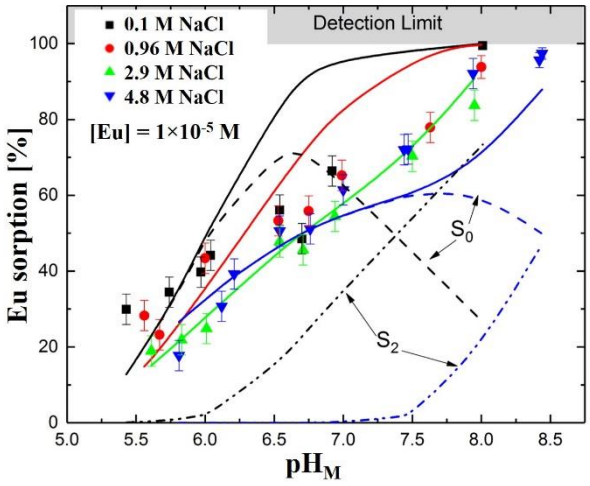

Figure 43. *Experimental (symbols) and modelled (solid lines) pH_M dependent Eu sorption ([Eu] = 1×10^{-5} M) onto trevorite at various ionic strengths. Modeling was performed using surface complexation model in FITEQL with the Pitzer approach and [TPA] database. The distribution of two complexes are represented by black (I = 0.1 M) and blue (I = 4.8 M) dashed/dotted lines, the contribution of S_1 is too ow to be visible on the figure.*

S_0: $(SOH^{-0.5})_3 + Eu^{3+} \leftrightharpoons \{(SOH^{-0.5})_3 Eu^{3+}\}$ $\log K_0$

Transfer of charge: $\Delta z_0 = 2.5$, $\Delta z_\beta = 1.0$

S_1: $(SOH^{-0.5})_3 + Eu^{3+} \leftrightharpoons \{(SOH^{-0.5})_2 (SO^{-1.5}) Eu^{3+}\} + H^+$ $\log K_1$

Transfer of charge: $\Delta z_0 = 1.5$, $\Delta z_\beta = 1.0$

S_2: $(SOH^{-0.5})_3 + Eu^{3+} + H_2O \leftrightharpoons \{(SOH^{-0.5})_2 (SO^{-1.5})Eu(OH)^{2+}\} + 2H^+$ $\quad log\ K_2$

Transfer of charge: $\Delta z_0 = 1.5$, $\Delta z_\beta = 0.0$

Table 15. *Complexation constants for Eu sorption to trevorite at infinite dilution.*

$\boldsymbol{log\ K_0}$	10.0 ± 0.1
$\boldsymbol{log\ K_1}$	-2.2 ± 0.1
$\boldsymbol{log\ K_2}$	-6.6 ± 0.1

v. Chromium oxide Cr_2O_3

1. Solid phase titration in dilute to concentrated NaCl solutions

As no detailed structural information was available for this compound, titration data were modeled (Figure 44) using the same approach as for trevorite, with a point of zero charge of 7.9 taken from literature [Blesa et al., 2000; Wisniewska and Szewczuk-Karpisz, 2013]. Compared to magnetite and trevorite, the inner layer capacitance is higher while the outer layer capacitance is lower, resulting in a low overall Stern capacitance for Cr_2O_3. Na^+ and Cl^- binding constants are similar (Table 16).

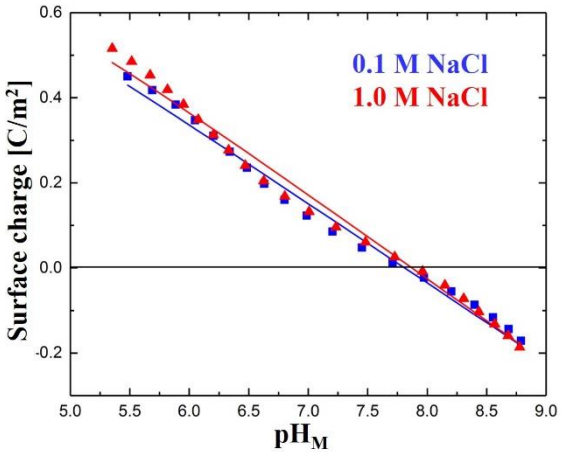

Figure 44. *Experimental (symbols) and modeled (solid lines) pH_M dependent charging behavior of Cr_2O_3 at two ionic strengths of NaCl. Numerical values are shown in Table 16.*

Table 16. *CD-MUSIC model parameters used for modeling the chromium oxide surface charging curves shown Figure 44.*

Capacitance 1	4.49	F/m^2
Capacitance 2	0.11	F/m^2
Overall Stern capacitance	0.11	F/m^2
Constant for Cl^- binding, log K_a	0.57	-
Constant for Na^+ binding, log K_c	0.53	-

2. pH dependent Eu uptake in dilute to concentrated NaCl solutions

At 1 g/L Cr_2O_3 and [Eu] = 5.1×10^{-10} M, the sorption is clearly pH dependent without a significant ionic strength effect (Figure 45). The behavior is comparable at [Eu] = 1×10^{-5} M, exhibiting a pH dependence but no ionic strength effect, with a lower sorption ranging from ~10 % at pH < 4 to ~73 % at pH_M 8.4. The amounts of dissolved chromium in these experiments were very low [Morelová, 2020].

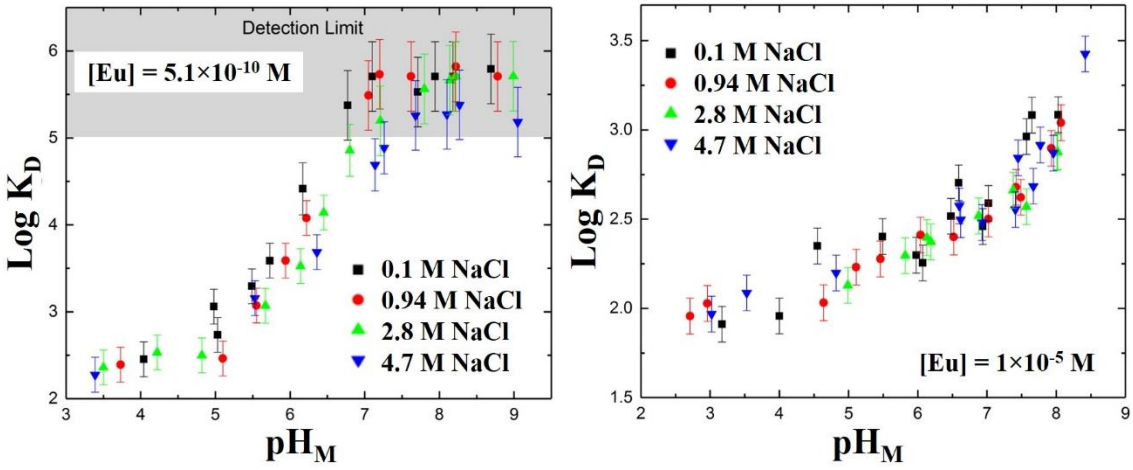

Figure 45. *Europium sorption (left: [Eu] = 5.1×10^{-10} M; right: [Eu] = 1×10^{-5} M) to chromium oxide (m/V = 1.0 g/L) at various ionic strengths of NaCl.*

Uptake experiments were also performed for a higher solid content (5.7 g/L Cr_2O_3) to reach conditions comparable to that in magnetite and trevorite uptake experiments [Morelová, 2020]. At [Eu] = 5.1×10^{-10} M, the behavior for Cr_2O_3 was comparable to that of both spinel compounds, reaching 99 % sorption at pH_M 6.3, and a low ionic strength effect can be seen. At [Eu] = 1×10^{-5} M, the uptake is pH dependent and the ionic strength effect is small.

3. Surface complexation model

Uptake data were modeled using the same model as for trevorite, considering a tridentate binding mode. Only sorption data obtained for the lowest europium concentration were modeled, and data at I = 4.7 M were not modeled because of lack of data in the low pH range. The model can thus only be considered as preliminary. A satisfactory fit to the experimental data was obtained and the model was able to capture the ionic strength effect (Figure 46). The experimental uptake data below pH_M 4.5 was underestimated, it could be improved by implementing more structural and electrostatic information. At I = 0.1 M, the contribution of S_0 is low over the whole pH_M range, while S_1 prevails until pH_M 7.0 above which S_2 is predominant. Outcomes suggest that the reactivity of the compound toward europium is comparable to that of magnetite and trevorite, implying that the formation of this corrosion product at the surface a canisters contributes to immobilizing actinide in the near-field.

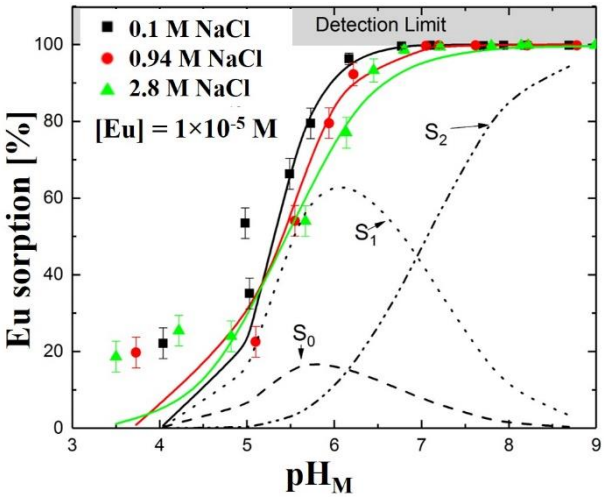

Figure 46. *Experimental (symbols) and modelled (solid lines) pH_M dependent Eu sorption ([Eu] = 1×10^{-5} M) onto chromium oxide at various ionic strengths. Modeling was performed using surface complexation model in FITEQL with the Pitzer approach and [TPA] database. The distribution of the complexes are represented by dashed/dotted lines for I = 0.1 M.*

S_0: $(SOH^{-0.5})_3 + Eu^{3+} \leftrightharpoons \{(SOH^{-0.5})_3 Eu^{3+}\}$ $\log K_0$

Transfer of charge: $\Delta z_0 = 2.0$, $\Delta z_\beta = 1.5$

$S_1: (SOH^{-0.5})_3 + Eu^{3+} \leftrightharpoons \{(SOH^{-0.5})_2 (SO^{-1.5})Eu^{3+}\} + H^+$ $\quad log\ K_1$

Transfer of charge: $\Delta z_0 = 1.0$, $\Delta z_\beta = 1.5$

$S_2: (SOH^{-0.5})_3 + Eu^{3+} + H_2O \leftrightharpoons \{(SOH^{-0.5})_2 (SO^{-1.5})Eu\,(OH)^{2+}\} + 2H^+$ $\quad log\ K_2$

Transfer of charge: $\Delta z_0 = 1.0$, $\Delta z_\beta = 0.5$

Table 17. *Complexation constants for Eu sorption to chromium oxide at infinite dilution.*

$\boldsymbol{log\ K_0}$	9.6 ± 0.1
$\boldsymbol{log\ K_1}$	2.5 ± 0.1
$\boldsymbol{log\ K_2}$	-5.2 ± 0.1

d. Eu uptake during synthesis of corrosion products

The uptake of trivalent lanthanides/actinides during the synthesis of magnetite was investigated at various ionic strengths set by NaCl under anoxic conditions. Magnetite was prepared by rising the pH of a solution containing ferrous and ferric ions (atomic ratio Fe(II):Fe(III) = 1:2) to 8.9–9.9 (Table 18) spiked with ^{152}Eu. After various equilibration times, the nature of the solid in suspension was identified by XRD and the amounts of dissolved Eu (gamma counter) were quantified after ultracentrifugation at 90,000 rpm for 60 minutes.

Table 18. *Experimental conditions for the preparation of samples, with pH_M and E_h values after synthesis (d0), after 1 (d1) and 7 (d7) days of equilibration. MgEuX refers to magnetite prepared in the presence of Eu. (n.d.: not determined).*

Sample	NaCl	$[Fe]_{tot}$	[Eu]	pH_M			E_h [mV *vs* Ag/AgCl]		
	[mol/L]	[mol/L]	[µmol/L]	d0	d1	d7	d0	d1	d7
MgEu1	0	0.109	109	8.90	8.95	n.d.	-570	-614	n.d.
MgEu2	0.1	0.109	109	8.78	8.66	n.d.	-540	-600	n.d.
MgEu3	1	0.109	109	8.97	8.89	n.d.	-520	-585	n.d.
MgEu4	3	0.109	109	9.44	9.19	n.d.	-540	-580	n.d.
MgEu5	5	0.109	109	9.90	9.75	n.d.	-540	-575	n.d.

In all samples, only the presence of magnetite could be detected (Figure 47). The diffractograms match that recorded for magnetite synthesized without added Eu and without added NaCl, indicating the absence of effect of Eu on the synthesis. Interestingly, reflexes became wider with increasing ionic strength (inset in Figure 47). This finding agrees with reported studies, where it was shown that increasing the ionic strength at constant pH results in the formation of smaller magnetite particles [Vaissières et al., 1998]. In these samples, the uptake was nearly quantitative after only 1 day (Table 19). Magnetite is an effective scavenger for trivalent actinides, this has been shown in this project (see above "Eu/Am adsorption to preformed corrosion product") and in reported coprecipitation studies [Finck et al., 2016].

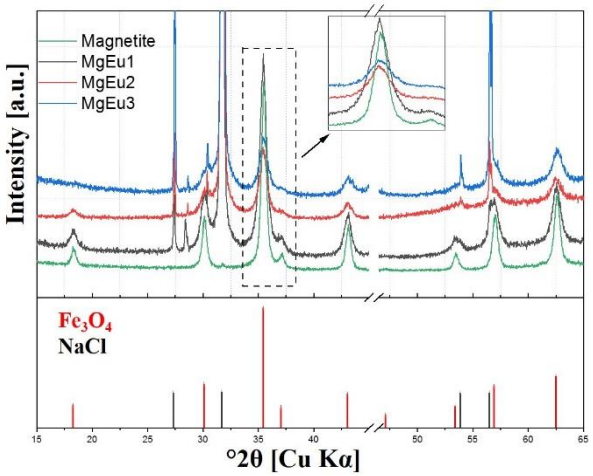

Figure 47. *X-ray diffractograms of samples MgEuX at day 1 and of magnetite synthesized without Eu and without added salt, patterns of reference compounds from the PDF-2 database.*

Table 19. *Eu uptake (%) in the magnetite series experiments at day 1.*

Sample	MgEu1	MgEu2	MgEu3	MgEu4	MgEu5
Eu uptake [%]	99.63	99.70	99.67	99.68	99.69

e. Structural incorporation of trivalent lanthanides/actinides into Fe corrosion phases: Theoretical calculations (DFT)

Uptake experiments in the laboratory were complemented by theoretical calculations. In the framework of this project, a novel application of first principle density functional theory (DFT) to the incorporation of lanthanides/actinides was explored. Both iron (hydr)oxides and lanthanides/actinides are very challenging from a theoretical perspective because of their open shell electronic structures. Investigations covered various iron (hydr)oxides, from pure ferric to mixed ferric and ferrous (hydr)oxide compounds, as well as various radionuclides (uranyl and trivalent lanthanides/actinides). The presence of Fe(II) rendered the application of DFT to magnetite and green rust very challenging. However, results showed convincingly that DFT is an appropriate tool for such theoretical studies and that it can provide very valuable information helping to improve the understanding of experimental work.

i. Incorporation of trivalent lanthanides into hematite and goethite

In the laboratory, ferrihydrite containing Lu(III) was left to transform into more stable hematite and goethite. The transformation products were analyzed by aberration corrected high-angle annular dark field scanning transmission electron microscopy (HAADF-STEM) and high efficiency energy dispersive X-ray spectroscopy (EDXS) [Yokosawa et al., 2019]. Besides, theoretical investigations were performed in order to determine whether Lu(III) is incorporated within hematite or within goethite nanoparticles. DFT calculations were performed with periodic boundary conditions as implemented in the Vienna Ab initio Simulation Package (VASP). The first step of the calculations was to determine the lattice parameters of the bulk hematite and goethite structures by looping over the volume and relaxing the positions of the ions and optimizing the cell shape. The optimized bulk structures of pure hematite and goethite served as basis for further theoretical exploration of the Lu(III) incorporation into these phases. For both compounds a 2×2×2 supercell containing 32 Fe(III) ions was used. Information on the energetics of Lu(III) incorporation within hematite or goethite was obtained by DFT and DFT+U calculations on the pure bulk phases, and DFT+U calculations for each structure where one of the 32 Fe(III) ions in the supercell was replaced by one Lu(III) ion.

In pure hematite, the *d*(Fe-O) distances calculated with DFT+U are 197 and 212 pm. Following the substitution of one Fe(III) by Lu(III), the corresponding *d*(Lu-O) distances in hematite determined with DFT+U are 212 and 226 pm. Averaging over these distances, the exact

experimental value of 219 pm is obtained [Finck et al., 2019]. In pure goethite, *d*(Fe-O) distances of 194, 197 (O^{2-}), 209 and 210 pm (OH^-) were obtained. Substitution of Lu(III) for Fe(III) resulted in a *d*(Lu-O^{2-}) distance of 212 and *d*(Lu-OH^-) distances of 223-224 pm with DFT+U, which are comparable to reported experimental data for Lu incorporated within goethite [Dardenne et al., 2002]. The increase in bond length from *d*(Fe-O) to *d*(Lu-O) is related to the larger ionic radius [Shannon, 1976] of Lu(III) (^{VI}Lu(III) = 86 pm) compared to Fe(III) (^{VI}Fe(III) = 65 pm). Furthermore, the correct antiferromagnetic state for the pure iron (hydr)oxides has been obtained. All these results underpin the high quality of the DFT+U calculations.

The agreement between calculated and experimental *d*(Lu-O) and *d*(Fe-O) was very good for both systems, implying that the corresponding energies can be considered well suited to estimate theoretically whether the incorporation of Lu(III) in hematite or in goethite is favored. In hematite and in goethite *d*(Fe-O) are similar, meaning that sites available for Fe substitution are of same ionic size in both structures, and thus substitution of Lu(III) for Fe(III) within both structures should thus be equally possible.

In order to determine in which mineral the incorporation of Lu(III) is energetically favored, following reaction was considered with (Iron oxide/Fe) corresponding to either hematite or goethite and (iron oxide/Lu) to the replacement of one Fe(III) by Lu(III) in either hematite or goethite.

$$\text{(iron oxide/Fe)} + \text{Lu(III)}(9H_2O) \rightarrow \text{(iron oxide/Lu)} + \text{Fe(III)}(9H_2O) \qquad \text{(Eq. 11)}$$

The corresponding reaction energies are key parameters to judge in which phase Lu is more likely to become incorporated: $\Delta E_{\text{iron oxide/Lu}} = E_{\text{iron oxide/Lu}} + E_{\text{Fe(9H2O)}} - E_{\text{iron oxide/Fe}} - E_{\text{Lu(9H2O)}}$. For hematite and goethite, calculations yielded $\Delta E_{\text{hematite/Lu}} = 0.12$ eV and $\Delta E_{\text{goethite/Lu}} = 0.20$ eV, respectively. Since these energy differences are very similar, DFT calculations indicate that the incorporation of Lu(III) should be equally likely for hematite and goethite and not even a slight preference can be determined. Additional information can be found in the corresponding publication [Yokosawa et al., 2019]. Consequently, the preferential incorporation within one transformation product over the other may likely be related to distinctively different and concurrent ferrihydrite transformation processes.

ii. Incorporation of uranium(V) into magnetite

Magnetite was synthesized in the presence of various U(VI) loadings (1,000-10,000 ppm) and the compounds were analyzed by various complementary microscopic and spectroscopic techniques in order to evidence the presence of U(V) in magnetite nanoparticles [Pidchenko et al., 2017]. Theoretical investigations were performed to support experimental efforts.

DFT calculations utilizing plane-wave basis sets with periodic boundary conditions as implemented in the VASP were performed to verify if the incorporation of U(V) is energetically favorable. A 2×2×2 magnetite supercell was used where one Fe^{2+} and one Fe^{3+} ions were replaced by U^{5+} and a vacancy ($Fe^{2+} + Fe^{3+} \rightarrow U^{5+} + \square$) for charge balance. Fe^{2+} and Fe^{3+} ions were chosen to be close to each other, hence the presence of the vacancy allows the substitution of Fe by U to relax more easily. Since U(V) is an open shell system, the occupation of the 5*f* orbitals and the orientation of the spin of this electron were carefully monitored.

Results show that U(V) can be incorporated into a Fe^{2+} or a Fe^{3+} octahedral site, since both cases are energetically very close to each other. Interestingly, the orientation of the spin was found to be important: the spin of the 5*f* electron points in the opposite direction compared to the spins of the two replaced Fe ions. Furthermore, DFT calculations yielded $d(U-O_2)$ and $d(U-Fe_1)$ values of 2.15(3) Å and 3.18(4) Å, respectively, in excellent agreement with experimental results of $d(U-O_2)$ = 2.18 Å and $d(U-Fe_1)$ = 3.18 Å, respectively. Additional information can be found in the corresponding publication [Pidchenko et al., 2017].

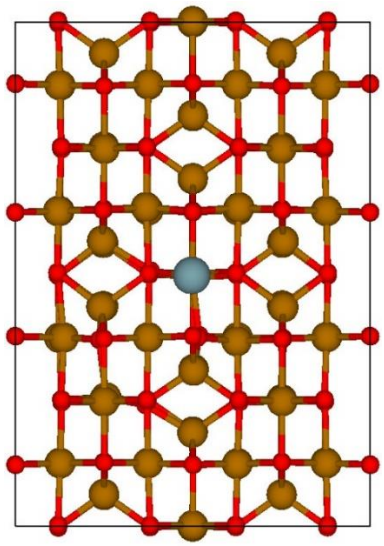

Figure 48. *U(V) incorporated into an octahedral site of magnetite as optimized by DFT. O atoms are red, Fe atoms are brown and the U atom is blue.*

iii. Incorporation of trivalent lanthanides/actinides into green rust

Green rust was detected as steel corrosion product in various experiments (see above), and can be considered as precursor to the formation of magnetite. Green rust is made of bructite-like layers of $Fe(OH)_2$ and the substitution of part of Fe^{2+} by Fe^{3+} creates a layer charge, which is compensated by interlayer anions (e.g. carbonate, sulfate or chloride). The structures of hydroxycarbonate GR(CO_3^{2-}), with the chemical formula $[Fe^{2+}_4Fe^{3+}_2(OH)_{12}]^{2+}\cdot[CO_3^{2-}\cdot 3H_2O]^{2-}$, and hydroxychloride with chemical formulas $GR_{2:1}(Cl^-)$ $[Fe^{2+}_2Fe^{3+}(OH)_6]^+\cdot[Cl^-\cdot 1.5H_2O]^-$ or $GR_{3:1}(Cl^-)$ $[Fe^{2+}_3Fe^{3+}(OH)_8]^+\cdot[Cl^-\cdot 1.5H_2O]^-$ were selected in this project. To set up calculations for GR(CO_3^{2-}), experimental results of Aissa et al. [Aissa et al., 2006] reporting lattice parameters and internal coordinates, and results of Rusch et al. [Rusch et al., 2008] reporting the ferrimagnetic behavior of Fe^{2+}/Fe^{3+} within one brucite layer of GR(CO_3^{2-}) were used.

Lattice parameters and internal coordinates of pure hydroxycarbonate and hydroxychloride green rust were characterized and available experimental structural data could be reproduced to a very high accuracy. Consequently, findings show that DFT+U is very well suited to describe the structure, the electric properties and the correct spin states of Fe^{2+}/Fe^{3+} in these compounds. Based on these results the incorporation of trivalent lanthanides (La, Eu) and actinides (Am, Cm) into the brucite layer of green rust by replacing Fe^{3+} was investigated.

Results showed that trivalent lanthanides and actinides are incorporated in the central plane of the brucite layer of GR(CO_3^{2-}) substituting for Fe^{3+}. Consequently, interatomic distances between Ln^{3+}/An^{3+} and the first six oxygen atoms are very similar. In contrast, for both GR(Cl^-) systems the trivalent lanthanides and actinides are significantly displaced off the central plane resulting in a split of the first O shell into two subshells having slightly longer/shorter interatomic distances. However, the mean interatomic distance to the first O shell in GR(Cl^-) is in reasonable agreement with reported experimental data [Finck et al., 2016]. The corresponding manuscript is in preparation [Polly et al., in preparation].

5. Extension 4th year: iron corrosion at the steel/bentonite interface under anoxic and elevated temperature conditions

During the term of the project, the participation as full partner in the Material Corrosion Test (MaCoTe) experiment at the Grimsel Test Site (Switzerland) was provided to KIT-INE, as leader of a group of German research institutions. The MaCoTe experiment is supervised by NAGRA and consists of heated and non-heated experiments to study the *in situ* corrosion of candidate canister materials embedded in bentonite (https://www.grimsel.com/gts-phase-vi/macote-the-material-corrosion-test/macote-introduction). Given this opportunity, it was decided to extend KORSO with a dedicated joint project to investigate the corrosion behavior of steel in contact with bentonite, where these *in situ* experiments within MaCoTe would be complemented by experiments performed in the laboratory at KIT-INE. In order to prepare these experiments and to gain experience in this new system, KORSO was extended by one year to perform preliminary experiments relevant to the steel/bentonite system. A separate project proposal to BMWi to follow up on this preparation phase with further studies integrated into MaCoTe has been developed together with the GRS (Braunschweig), the German Federal Institute for Geosciences and Natural Resources (BGR, Hannover) and the Institute for Material Sciences of the University of Hannover.

a. Experimental

All experiments, from sample preparation until sample analysis were performed under anoxic conditions, whether in an Ar-filed glovebox or in airtight containers. The same materials as used above for experiments in high saline conditions were used, allowing direct comparison of the medium on the corrosion behavior. SGI and 309S coupons had 6 mm × 6 mm × 4 mm in size, were polished with carbide paper and diamond paste, and cleaned in an ultrasonic bath. The MX-80 bentonite was selected in this project and used without preliminary purification or fractionation. The bentonite was hydrated by 0.1 M NaCl at m/V = 150 g/L for one day at room temperature. At this stage, pH and E_h values were 6.2 and -44.5 mV *vs* Ag/AgCl, respectively. In 5 mL glass vials, 3 mL of this suspension was added to one steel specimen each. Vials were sealed with a rubber septum and placed in an oven at 65°C. Replicates were prepared allowing to stop experiments after 1, 2 and 6 months of contact time. After cooling down to room temperature, vials were transferred to inside the glovebox and opened. Steel specimens were taken out carefully with a tweezer, and the sticking clay was scrapped off to be measured by XRD. Coupons were carefully washed and dried in the glovebox for investigations by XPS and

SEM/EDX. Lastly, the remaining clay in the vial was taken out to be ultracentrifuged before quantification of the supernatant by ICP-OES.

b. Results

Both investigated steels showed different behavior (Figure 49). For SGI, the color of the bentonite in contract with the steel became blue/green already after 1 month of contact time and the thickness of colored bentonite increased with the contact time. The observed coloration can be attributed to steel corrosion and iron diffusion away from the steel/bentonite interface. In contrast, the bentonite in contact with 309S hardly changed color, only a slight brown color was seen after 6 months.

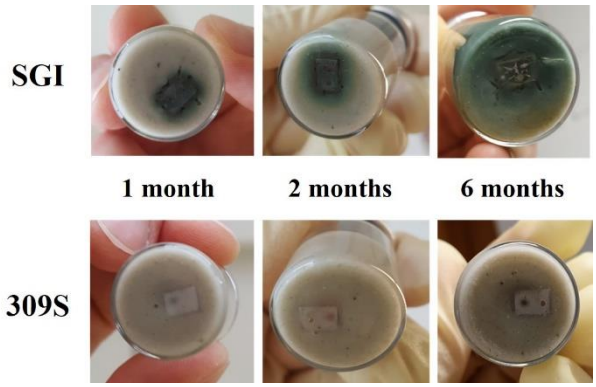

Figure 49. *Pictures showing the evolution of steel (top: SGI, bottom: 309S) in contact with bentonite after 1 month (left), 2 months (middle) and 6 months (right).*

The bentonite porewater in experiments with 309S did not show any progressive or significant evolution of the composition (Table 20), suggesting a very low corrosion damage, in agreement with visual inspection of the systems. For experiments performed with SGI, the porewater had comparable composition, except a lower Si content, a higher Mg content and a decreasing K content with increasing contact time. Unfortunately, pH and E_h could not be measured reliably in this case. However, indicative information on local pH at the steel/bentonite interface could be obtained by using standard commercial pH paper. The amount of water was not important but enough to react with the paper and the color to change. After 6 months, data suggest that the pH at the steel/bentonite interface is around 5.5 for 309S, and around 7-8 for SGI. The

uncertainty associated with this determination of pH is rather high but values may suggest a slight decrease for 309S and a slight increase in the case of SGI.

Table 20. *Composition of the bentonite porewater (mg/L) after various contact times with 309S or SGI.*

	Si	Na	K	Ca	Sr	Al	Fe	Mg	Cr	Ni	S
309S											
1 month	24.31	2341	46.49	76.8	3.73	1.35	0.35	12.4	<	<	112.6
2 months	24.72	2658	34.04	84.46	4.06	<	<	13.18	<	<	134.91
6 months	35.91	2553	42.99	81.63	4.09	0.12	<	11.37	<	<	136.2
SGI											
1 month	13.93	2342	38.65	83.02	3.66	0.32	0.11	16.96	<	<	105.8
2 months	11.00	2593	32.70	103.45	3.72	<	<	22.45	<	<	124.14
6 months	15.58	2515	28.77	75.17	2.74	0.39	13.5	20.4	<	<	117.6

Information on mineralogy of the contacting bentonite was provided by XRD analysis (Figures 50 and 51). The starting material is mostly made of montmorillonite, with the presence of admixed quartz, cristobalite, calcite and feldspars (e.g., microcline, albite, not indexed on figures). After 6 months of contact with either SGI or 309S, the mineralogical composition of the bentonite is essentially the same as that of the starting material, and differences in intensity can be related to orientation of particles. This result implies that no mineral phase dissolved quantitatively and that no new phase formed (or formed in very low amount).

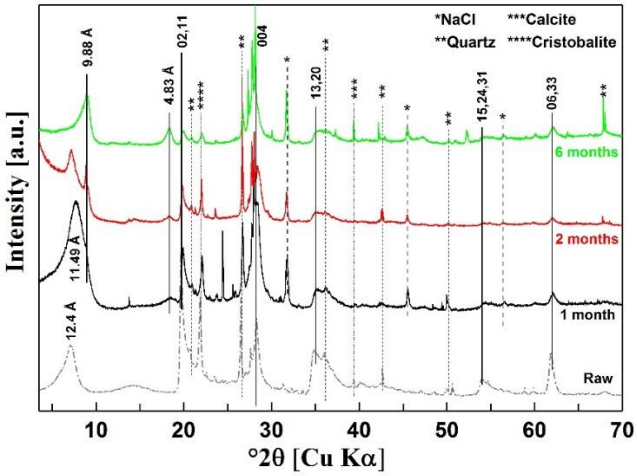

Figure 50*. X-ray diffractograms of the starting (raw) MX-80 bentonite and after 1, 2 and 6 months of contact time with SGI at 65°C under anoxic conditions. Basal spacings are indicated, lattice planes of montmorillonite are indexed and various admixed phases are identified.*

The low angular region of the diffractograms contains information on basal spacing and water content of the interlayer. The basal spacing (d_{001} or basal repeat distance) of montmorillonite in the raw material equals 12.4 Å and only 11.49 Å after one month of contact time with SGI, which can be attributed to a slightly different hydration state of interlayer cations. This reflex also contains a shoulder at ~9.88 Å, which becomes a clear reflex at 2 months of contact time and the only reflex at 6 months. Note the parallel formation and increase in intensity of the reflex at 4.83 Å. Montmorillonite is able to swell, i.e., increasing the water content of the interlayer. In contrast, mica and illite are not able to swell, have a basal spacing of d_{001} ~9.90 Å and their interlayer frequently contains potassium. Interestingly, the analysis of the supernatants showed a decrease in dissolved potassium with increasing contact time (Table 20). The decrease in dissolved K in the supernatant and the decrease in basal spacing may suggest an uptake of potassium, which is tightly bound to ditrigional cavities of two consecutive layers and thus prevents montmorillonite to swell. In that case, the reflex at 4.83 Å would then correspond to d_{002}. If potassium would be taken up by the smectite, Ca or Na should be released but unfortunately, a corresponding clear increase in dissolved amounts of these cations could not be detected in the supernatant. In experiments with 309S, already after only 1 month of contact time, the basal spacing is ~9.80 Å and diffractograms also contain a reflex at 4.83 Å. This would suggest that the reaction was faster with this steel, but visual inspection and quantification of the supernatant showed that 309S was hardly damaged in these experiments. Further work is needed to decipher the actual underlying mechanism responsible for this

decrease in basal spacing. The presence of typical corrosion phases such as green rust or magnetite may be ruled out by the absence distinctive reflex at ~11 °2θ (sulfate green rust), ~11.5 °2θ (chloride green rust) and at ~35.4 °2θ (magnetite). Likewise, the absence of reflex at ~12.5 °2θ and ~25.1 °2θ rules the presence of iron silicate phases such as cronstedtite or berthierine.

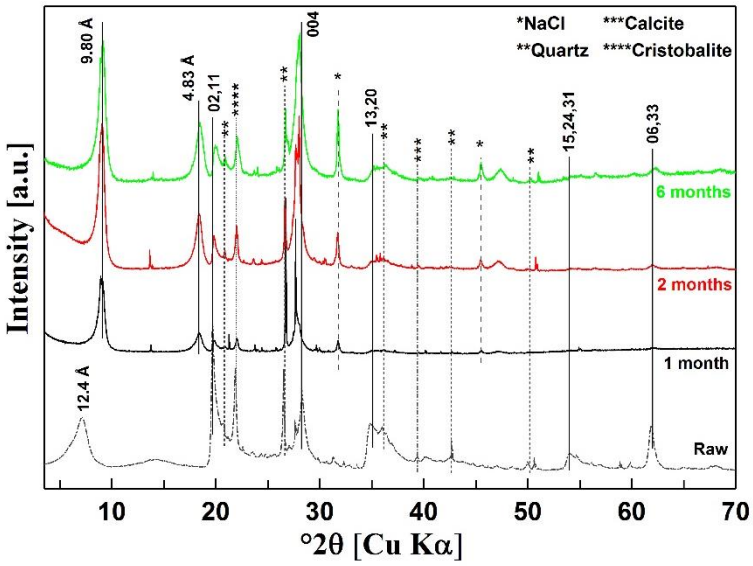

Figure 51. *X-ray diffractograms of the starting (raw) MX-80 bentonite and after 1, 2 and 6 months of contact time with 309S at 65°C under anoxic conditions. Basal spacings are indicated, lattice planes of montmorillonite are indexed and various admixed phases are identified.*

Complementary information on the bentonite contacting the steel for 6 months was provided by Fourier transform infrared (FTIR) spectroscopy using an INVENIO-R spectrometer equipped with an ATR accessory (Platinum) and a DLaTGS detector. With the available experimental setup, these measurements could only be performed under ambient (air) conditions, but the contact time with air was limited and is believed to not having influenced the results.

Overall, no significant changes upon contacting steels could be detected by FTIR spectroscopy (Figure 52). The position of the –OH stretching band (3628 cm^{-1}) is typical of montmorillonite [Finck et al., 2015b; Madejová and Komadel, 2001]. The broad band centered at 3410 cm^{-1} can be attributed to –OH stretching of water and the corresponding –OH deformation band at 1635 cm^{-1} [Madejová and Komadel, 2001]. Bands at 995 cm^{-1} and at 1116 cm^{-1} can be attributed to Si-O stretching [Madejová and Komadel, 2001]. Bands at 915 cm^{-1}, 879 cm^{-1}, 842 cm^{-1} and at

796 cm^{-1} can be attributed to Al_2-OH, AlFe(III)-OH, AlMg-OH and to Fe(III)Mg-OH deformation, respectively [Finck et al., 2015b; Gates, 2008]. Note that the band at 796 cm^{-1} can also be attributed to the presence of admixed quartz and the band at 879 cm^{-1} to admixed calcite [Finck et al., 2015b; Madejová and Komadel, 2001]. Finally, bands at 693 cm^{-1} and 517 cm^{-1} can be attributed to Si-O vibration and to Al-O-Si deformation, respectively [Madejová and Komadel, 2001]. The band at 729 cm^{-1} could not be attributed with certainty, but may possibly be attributed to $Fe(II)_2$-OH [Gates, 2008] or alternatively to admixed feldspars. IR spectra of sulfate green rust contain bands at 515, 780, 880 and 1550 cm^{-1} arising in the brucite-like sheet, and IR spectra of magnetite bands at 570 and 375 cm^{-1} [Usman et al., 2018]. Some of these bands overlap with that of montmorillonite and others are absent in the spectra of bentonites, ruling out the presence of green rust or magnetite in significant amounts in these samples. These results show that the composition of the bentonite was not affected during the corrosion experiments, or only to a level not detected by this technique.

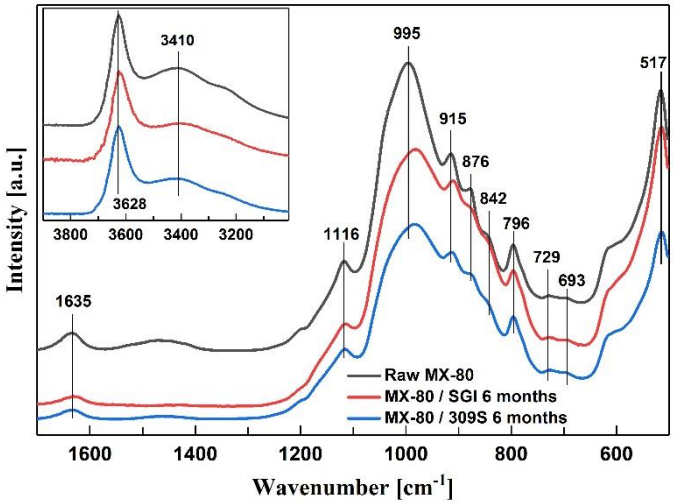

***Figure 52**. FTIR spectra of the raw MX-80 bentonite (black), the bentonite contacting SGI (red) and 309S (blue) for 6 months. Inset show the hydroxyl stretching region.*

The steel specimen were analyzed by XPS and SEM-EDX after removing the bentonite sticking at the surface. Morphological changes could be seen at the surface of SGI coupons after 1 and 2 months of contact time (Figure 53). After 1 month, the electron micrograph shows a lamellar structure adjacent to a more compact structure containing graphite nodules. Observations indicate that graphite is included in ferrite, which is further surrounded by pearlite. Pearlite has a lamellar structure composed of alternating layers of ferrite (α-Fe) and cementite (Fe_3C).

Images suggest a preferential dissolution of ferrite from pearlites [Lee et al., 2006], leaving cementite lamella. After 6 months, the surface seems flakier and no preferential morphology changes could be observed. No presence of iron (hydr)oxide could be detected, if present they likely would have been removed with the sticking bentonite. For the 309S coupon, no modification of the surface morphology could be detected, hinting at the absence of surface damage.

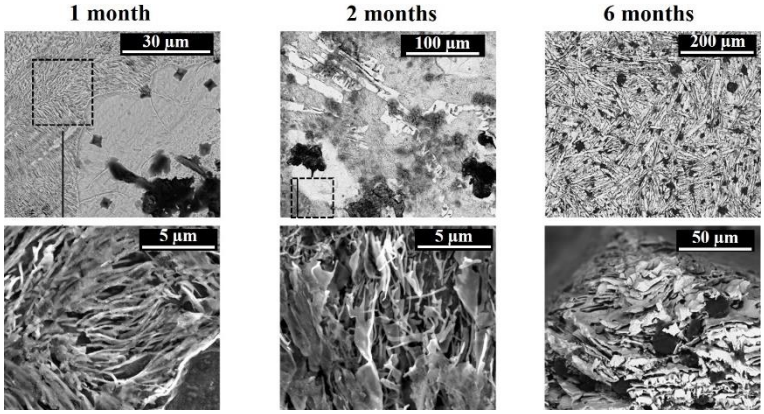

Figure 53*. Electron micrographs of SGI coupons contacting bentonite for 1 (left), 2 (middle) and 6 months (right) at two magnifications.*

Information on individual elements at the surface was provided by XPS. After 1 months, hardly any metallic Fe can be detected and most of the iron is present as Fe(II) (Figure 54). With increasing contact time, the contribution of Fe(0) and Fe(III) increase, which may be surprising. Actually, at early stages, iron may corrode readily upon contact with bentonite porewater and result in the formation of Fe(II)-bearing corrosion products (such as green rust) covering the surface. The corrosion may slow down with time and neoformed Fe products may react/transform/dissolve upon contact with bentonite resulting in iron diffusion away from the interface, leaving a less protected surface (i.e. Fe(0)). The increase in Fe(III) contribution may be explained by the conversion of initial $Fe(OH)_2$ or green rust into magnetite. These findings may be corroborated by narrow O 1*s* spectra. Initially, oxygen is mostly present as hydroxide, and with increasing time, the oxide component increases, corroborating a conversion from hydrous to oxide Fe compounds. For 309S, only Cr and O could be detected by XPS. After 1 month of contact time, Cr is dominantly present as Cr(III) hydroxide, with a lower fraction of metallic Cr. This indicates the formation of a passive film. With increasing contact time, the

contribution of Cr(0) decreases as well as the contributions from $Cr(OH)_3$ in favor of Cr_2O_3. This result would suggest that Cr oxidized to form $Cr(OH)_3$ first, before converting to Cr_2O_3. This would agree with results obtained by µXAS analysis of 309S corroded in high saline brines showing the presence of the same compounds at the corrosion front.

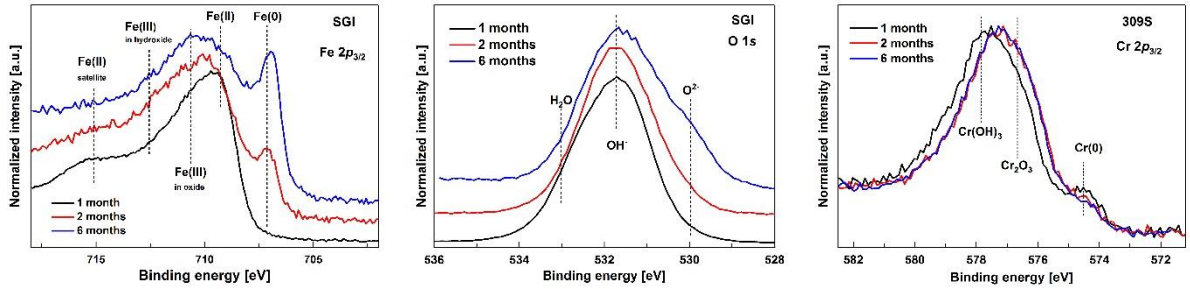

Figure 54. *Fe $2p_{3/2}$ (left) and O 1s (middle) X-ray photoelectron spectra recorded for SGI coupons and Cr $2p_{3/2}$ spectra (right) recorded for 309S coupons after 1, 2 and 6 months of contact time with bentonite.*

c. Corrosion mechanism and comparison with experiments in high saline brines

The behavior of 309S differed from that of SGI in contact with bentonite at 65°C. The stainless steel was hardly affected, only the formation of a passivation film could be detected. This behavior is very similar to that in high salt content (Table 8), implying that in experiments with bentonite the presence of additional dissolved species (e.g., Si, Ca, Mg) in the porewater played no role.

The surface of SGI was attacked, meaning that iron oxidized. This was evidenced by visual inspection, suggesting the formation of Fe-bearing corrosion products. Electron micrographs revealed that the origin of iron was the preferential dissolution of ferrite from the pearlite. No presence of newly formed phase could not be detected by XRD or FTIR, but XPS suggested the formation of hydrous compounds (e.g., GR). The formation of such corrosion products was also identified in experiments performed in autoclaves (Table 5), but no formation of magnetite or iron silicates could be detected in experiments with bentonite. Dedicated experiments with longer contact times are needed to unambiguously identify the long-term stable phase(s).

6. Acknowledgements

The German Federal Ministry for Economic Affairs and Energy (BMWi) within the KORSO project (grant agreement n° 02 E 11496 B) is acknowledged for financial support.

The KIT synchrotron light source (Karlsruhe, Germany) is acknowledged for provision of synchrotron radiation beam time, and the Institute for Beam Physics and Technology is thanked for the operation of the storage ring, the Karlsruhe Research Accelerator (KARA). Dr Kathy Dardenne (KIT-INE) and Dr Jörg Rothe (KIT-INE) are gratefully acknowledged for their help and availability during measurements at the INE Beamline.

The synchrotron light source SOLEIL (Saint Aubin, France) is acknowledged for provision of synchrotron radiation beam time, and the staff at the DiffAbs beamline, especially Dr Solenn Reguer, is gratefully acknowledged for the help and availability during measurements at the beamline.

Dr Michel Schlegel (CEA Saclay, France) is gratefully acknowledged for his help and constructive discussions on corrosion mechanisms. Dr Johannes Lützenkirchen is gratefully acknowledged for his help, time and expertise in uptake studies. This work would also not have been possible without the support of many other colleagues of KIT-INE.

The French National Museum of Natural History is acknowledged for provision of reference compounds.

Gefördert durch:

aufgrund eines Beschlusses
des Deutschen Bundestages

7. References

Ahmed, F.A., Elraies, A.K., Mohammed, A.A., Gaafar, R.G., 2015. An investigation study on the effect of brine composition on silica dissolution. Adv. Environ. Geol. Sci. Engineer., 188-192. ISBN: 978-1-61804-314-6

Aissa, R., Francois, M., Ruby, C., Fauth, F., Medjahdi, G., Abdelmoula, M., Génin, J.-M., 2006. Formation and crystallographical structure of hydroxysulfate and hydroxycarbonate green rusts synthesized by coprecipitation. J. Phys. Chem. Solids. 67, 1016-1019. doi.org/10.1016/j.jpcs.2006.01.020

Altmaier, M., Metz, V., Neck, V., Müller, R., Fanghänel, T., 2003. Solid-liquid equilibria of $Mg(OH)_2$(cr) and $Mg_2(OH)_3Cl{\cdot}4H_2O$(cr) in the system Mg-Na-H-OH-Cl-H_2O at 25°C. Geochim. Cosmochim. Acta, 67, 3595-3601. doi.org/10.1016/S0016-7037(03)00165-0

Altmaier, M., Neck, V., Fanghänel, T., 2008. Solubility of Zr(IV), Th(IV) and Pu(IV) hydrous oxides in $CaCl_2$ solutions and the formation of ternary Ca-M(IV)-OH complexes. Radiochim. Acta, 96, 541-550. doi.org/10.1524/ract.2008.1535

Appelo, C.A.J., 2015. Principles, caveats and improvements in databases for calculating hydrogeochemical reactions in saline waters from 0 to 200 °C and 1 to 1000 atm. Applied Geochem. 55, 62-71. doi.org/10.1016/j.apgeochem.2014.11.007

ASTM International, 2003. G1-03 Standard Practice for Preparing, Cleaning, and Evaluating Corrosion Test Specimens. West Conshohocken, PA; ASTM International. doi.org/10.1520/G0001-03

Bach, D., Christiansen, B.C., Schild, D., Geckeis, H., 2014. TEM study of green rust sodium sulphate ($GR_{Na,SO4}$) interacted with neptunyl ions (NpO_2^+). Radiochim. Acta 102, 279-289. doi.org/10.1515/ract-2013-2105

Banik, N.L., Marsac, R., Lützenkirchen, J., Marquardt, C.M., Dardenne, K., Rothe, J., Bender, K. Geckeis, H., 2017. Neptunium sorption and redox speciation at the illite surface under highly saline conditions. Geochim. Cosmochim. Acta 215-421-431. dx.doi.org/10.1016/j.gca.2017.08.008

Barale, M., Mansour, C., Carrette, F., Pavageau, E.M., Catalette, H., Lefèvre, G., Fedoroff, M., Cote, G., 2008. Characterization of the surface charge oxide particles of PWR primary water circuits from 5 to 320°C. J. Nucl. Mater. 381, 302-308. doi.org/10.1016/j.jnucmat.2008.09.003

Baroux, B., 1988. The kinetics of pit generation on stainless steel. Corros. Sci. 28, 969-986. doi.org/10.1016/0010-938X(88)90015-7

Bethke, C.M., 1996. Geochemical Reaction Modeling. Concepts and Applications. Oxford University Press.

Bethke, C.M., Yeakel, S., 2018. The Geochemist's Workbench. Release 11. GWB Essentials Guide. Aqueous Solutions, LLC, Champaign, Illinois. www.gwb.com/pdf/GWB11/GWBessentials.pdf

Beverskog, B., Puigdomenech, I., 1999. Pourbaix diagrams for the ternary system of iron-chromium-nickel. Corros. 55, 1077-1087. doi.org/10.5006/1.3283945

Blesa, M.A., Weisz, A.D., Morando, P.J., Salfity, J.A., Magaz, G.E., Regazzoni, A.E., 2000. The interaction of metal oxide surfaces with complexing agents dissolved in water. Coord. Chem Rev. 196, 31-63. doi.org/10.1016/S0010-8545(99)00005-3

Broli, A., Holtan, H., Midjo, M., 1973. Use of potentiokineti and potentiostatic methods for the determination of characteristic potentials for pitting corrosion of an Fe-Cr alloy. Br. Corros. J. 8, 173-176. doi.org/10.1179/000705973798322189

Catalette, H., Dumonceau, J., Ollar, P., 1998. Sorption of cesium, barium and europium on magnetite. J. Contam. Hydrol. 35, 151-159.

Christiansen, B., Geckeis, H., Marquardt, C., Bauer, A., Römer, J., Wiss, T., Schild, D., Stipp, S., 2011. Neptunyl (NpO_2^+) interaction with green rust, $GR_{Na,SO4}$. Geochim. Cosmochim. Acta 75, 1216-1226. doi.org/10.1016/j.gca.2010.12.003

Ciavatta, L., 1980. The specific interaction theory in evaluating ionic equilibria. Ann. Chim. (Rome) 70, 551-567.

Dardenne, K., Schäfer, T., Lindqvist-Reis, P., Denecke, M.A., Plaschke, M., Rothe, J., Kim, J.I., 2002. Low temperatur investigation on the lutetium binding changes during the 2-line ferrihydrite alteration process. Environ. Sci. Technol. 36, 5092-5099. doi.org/10.1021/es025513f

Davies, C.W., 1962. Ion Association. Butterworths, London, 37-53.

Dumas, T., Fellhauer, D., Schild, D., Gaona, X., Altmaier, M., Scheinost, A.C, 2019. Plutonium retention mechanisms by magnetite under anoxic conditions: Entrapment versus sorption. ACS Earth Space Chem. 3, 2197-2206. 10.1021/acsearthspacechem.9b00147

Elgrishi, N., Rountree, K.J., McCarthy, B.D., Rountree, E.S., Eisenhart, T.T., Dempsey, J.L., 2018. A practical beginner's guide to cyclic voltammetry. J. Chem. Educ. 95, 197-206.

El Mendili, Y., Abdelouas, A., Ait Chaou, A., Bardeau, J.-F., Schlegel, M.L., 2014. Carbon steel corrosion in clay-rich environment. Corr. Sci., 88, 56-65. dx.doi.org/10.1016/j.corsci.2014.07.020

Estes, S.L., Arai, Y., Becker, U., Fernando, S., Yuan, K., Ewing, R.C., Zhang, J., Shibata, T., Powell, B., 2013. A self-consistent model describing the thermodynamics of Eu(III) adsorption onto hematite. Geochim. Cosmochim. Acta 122, 430-447. dx.doi.org/10.1016/j.gca.2013.08.023

Finck, N., Dardenne, K., Geckeis, H., 2015. Am(III) coprecipitation with and adsorption on the smectite hectorite. Chem. Geol. 409, 12-19. doi.org/10.1016/j.chemgeo.2015.04.020

Finck, N., Schlegel, M.L., Bauer, A., 2015b. Structural iron in dioctahedral and trioctahedral smectites: a polarized XAS study. Phys. Chem. Minerals 42, 847-859. doi.org/10.1007/s00269-015-0768-3

Finck, N., Nedel, S., Dideriksen, K., Schlegel, M.L., 2016. Trivalent actinide uptake by iron (hydr)oxides. Environ. Sci. Technol. 50, 10428-10436. doi.org/10.1021/acs.est.6b02599

Finck, N., Radulescu, L., Schild, D., Rothmeier, M., Huber, F., Lützenkirchen, J., Rabung, T., Heberling, F., Schlegel, M.L., Dideriksen, K., Nedel, S., Geckeis, H., 2016b. XAS signatures of Am(III) adsorbed onto magnetite and maghemite. J Phys. Conf. Ser. 712, 012085. doi:10.1088/1742-6596/712/1/012085

Finck, N., Bouby, M., Dardenne, K., 2019. Fate of Lu(III) sorbed on 2-line ferrihydrite at pH 5.7 and aged for 12 years at room temperature. I: Insights from ICP-OES, XRD, ESEM, AsFlFFF/ICP-MS, and EXAFS spectroscopy. Environ. Sci. Pollut. Res. 26, 5238-5250. doi.org/10.1007/s11356-018-1314-x

Frankel, G.S., 1998. Pitting corrosion of metals: A review of critical factors. J. Electrochem. Soc. 145, 2186-2198. doi.org/10.1149/1.1838615

García, D., Lützenkirchen, J., Petrov, V., Siebentritt, M., Schild, D., Lefèvre, G., Rabung, T., Altmaier, M., Kalmykov, S., Duro, L., Geckeis, H., 2019. Sorption of Eu(III) on quartz at high salt concentrations. Colloids Surf., A 578, 123610. doi.org/10.1016/j.colsurfa.2019.123610

Gates, W.P., 2008. Cation mass-valence sum (CM-VS) approach to assessing OH-bending bands in dioctahedral smectites. Clays Clay Minerals, 56, 10-22. doi.org/10.1346/CCMN.2008.0560102

Gaudin, A., Gaboreau, S., Tinseau, E., Bartier, D., Petit, S., Grauby, O., Foct, F., Beaufort, D., 2009. Mineralogical reactions in the Tournemire argilite after in-situ interaction with steels. Appl. Clay Sci. 43, 196-207. doi.org/10.1016/j.clay.2008.08.007

Geckeis, H., Lüzenkirchen, J., Polly, R., Rabung, T., Schmidt, M., 2013. Mineral-water interface reactions of actinides. Chem. Rev. 113, 1016-1062. dx.doi.org/10.1021/cr300370h

Grambow, B., Smailos, E., Geckeis, H., Müller, R., Hentschel, H., 1996. Sorption and reduction of uranium(VI) on iron corrosion products under reducing saline conditions. Radiochim. Acta 74, 149-154. doi.org/10.1524/ract.1996.74.special-issue.149

Grenthe, I., Mompean, F., Spahiu, K., Wanner, H., 2013. TDB-2. Guidelines for the extrapolation to zero ionic strength. OECD, Nuclear Energy Agency, Data Bank, Issy-les-Moulineaux, France. www.oecd-nea.org/dbtdb/guidelines/tdb2.pdf

Grivé, M., Duro, L., Colàs, E., Giffaut, E., 2015. Thermodynamic data selection applied to radionuclides and chemotoxic elements: An overview of the ThermoChimie-TDB. Appl. Geochem. 55, 85-94. doi.org/10.1016/j.apgeochem.2014.12.017

Guillaumont, R., Fanghänel, T., Fuger, J., Grenthe, I., Neck, V., Palmer, D.A., Rand, M.J.H., 2003. Update on the Chemical Thermodynamics of Uranium, Neptunium, Plutonium, Americium and Technetium. Chemical Thermodynamics Vol. 5, OECD, Nuclear Energy Agency. ISBN: 0-444-51401-5

Hansen, F.D., Leigh, C.D., 2011. Salt disposal of heat-generating nuclear waste. Sandia Report SAND2011-0161, Sandia National Laboratories. https://energy.sandia.gov/wp-content/gallery/uploads/SAND2011-0161.pdf

Harvie, C.E., Møller, N. and Weare, J.H., 1984. The prediction of mineral solubilities in natural waters: The Na-K-Mg-Ca-H-Cl-SO_4-OH-HCO_3-CO_3-CO_2-H_2O system to high ionic strengths at 25°C. Geochim. Cosmochim, Acta 48, 723-751.

Heusler, K.E., Landolt, D., Trasatti, S., 1989. Electrochemical corrosion nomenclature. Pure Appl. Chem. 61, 19-22. doi.org/10.1351/pac198961010019

Hiemstra, T., Van Riemsdijk, W.H., 1996. A surface structural approach to ion adsorption: The Charge Distribution (CD) model. J. Colloid Interface Sci. 179, 488-508. doi.org/10.1006/jcis.1996.0242

Huber, F., Schild, D., Vitova, T., Rothe, J., Kirsch, R., Schäfer, T., 2012. U(VI) removal kinetics in presence of synthetic magnetite nanoparticles. Geochiom. Cosmochim. Acta 96, 154-173. dx.doi.org/10.1016/j.gca.2012.07.019

Hummel, W., Berner, U., Curti, E., Pearson, F.J., Thoenen, T., 2002. Nagra/PSI chemical thermodynamic database 01/01. Radiochim. Acta 90, 805-813. doi.org/10.1524/ract.2002.90.9-11_2002.805

Hung, C.-C., Wu, Y.-C., King, F., 2017. Corrosion assessment of canister for the disposal of spent nuclear fuel in crystalline rock in Taiwan. Corr. Engineer. Sci. Technol. 52, 194-199. doi.org/10.1080/1478422X.2017.1285855

Hsu, C.-H., Chen, M.L., 2010. Corrosion behavior of nickel alloyed and austempered ductile irons in 3.5 % sodium chloride. Corros. Sci. 52, 2945-2949. doi.org/10.1016/j.corsci.2010.05.006

HZDR, 2018. RES^{3}T – Rossendorf Expert System for Surface and Sorption Thermodynamics. https://www.hzdr.de/db/RES3T.DATAASSEMBLY

Ilton, E.S., Boily, J.-F., Buck, E.C., Skomurski, F.N., Rosso, K.M., Cahill, C.L., Bargar, J.R., Felmy, A., 2010. Influence of dynamical conditions on the reduction of U^{VI} at the magnetite−solution interface. Environ. Sci. Technol. 44, 170-176. doi.org/10.1021/es9014597

Kienzler, B., Loida, A., 2001. Endlagerrelevanten Eigenschaften von hochradioaktiven Abfallprodukten – Charakterisierung und Bewertung – Empfehlungen des Arbeitskreises HAW-Produkte. Wissenschaftliche Berichte, FZKA 6651, Forschungszentrum Karlsruhe. ISSN 0947-8620.

Kienzler, B., 2017a. Corrosion of canister materials for radioactive waste disposal. Atw. International Zeitschrift für Kernenergie, 62, 542-549.

Kienzler, B., 2017b. F&E-Arbeiten zur Korrosion von Endlager-Behälterwerkstoffen im INE. KIT Scientific Reports 7729, KIT Scientific Publishing, KIT, Karlsruhe. ISBN 978-3-7315-0648-5. DOI: 10.5445/KSP/1000067005

King, F., 2008. Corrosion of carbon steel under anaerobic conditions in a repository for SF and HLW in Opalinus Clay. NAGRA Technical Report 08-12.

King, F., 2012. 4 - General corrosion in nuclear reactor components and nuclear waste disposal systems, pp 77-130. In: Feron, D. (Ed) *Nuclear Corrosion Science and Engineering*, Woodhead Publishing Series in Energy, 2012. ISBN 9781845697655

King, F., Sanderson, D., Watson, S., 2016. Durability of High Level Waste and Spent Fuel Disposal Containers – an overview of the combined effect of chemical and mechanical degradation mechanisms. Quintessa report for the Nuclear Decommissioning Agency, QRS-1589A-R9.

Kirchheim, R., Heine, B., Fischmeister, H., Hofmann, S., Knote, H., Stolz, U., 1989. The passivity of iron-chromium alloys. Corros. Sci. 29, 899-917. doi.org/10.1016/0010-938X(89)90060-7

Kirsch, R., Fellhauer, D., Altmaier, M., Neck, V., Rossberg, A., Fanghänel, T., Charlet, L., Scheinost, A., 2011. Oxidation state and local structure of plutonium reacted with magnetite, mackinawite, and chukanovite. Environ. Sci. Technol. 45, 7267-7274. doi.org/10.1021/es200645a

Kursten, B., Smailos, E., Azkarate, I., Werme, L., Smart, N.R., Santarini, G., 2004. COBECOMA. State-of-the-art document on the COrrosion BEhaviour of Container Materials. Final report.

Latta, D.E., Boyanov, M.I., Kemner, K.M., O'Loughlin, E.J., Scherer, M., 2015. Reaction of uranium(VI) with green rusts: Effect of interlayer anion. Curr. Inorg. Chem. 5, 156-168.

Latta, D.E., Gorski, C.A., Boyanov, M.I., O'Loughlin, E.J., Kemner, K.M, Scherer, M., 2011. Influence of magnetite stoichiometry on U^{VI} reduction. Environ. Sci. Technol. 46, 778-786. dx.doi.org/10.1021/es2024912

Lee, C.T., Odziemkowski, M.S., Shoesmith, D.W., 2006. An in situ Raman-electrochemical investigation of carbon steel corrosion in Na_2CO_3/$NaHCO_3$, Na_2SO_4, and NaCl solutions. J. Electrochem. Soc. 153, B33-B41. doi.org/10.1149/1.2140680

Li, D.; Kaplan, D., 2012. Sorption coefficients and molecular mechanisms of Pu, U, Np, Am and Tc to Fe (hydr)oxides: A review. J. Hazard. Mater. 243, 1-18. dx.doi.org/10.1016/j.jhazmat.2012.09.011

Lützenkirchen, J., 2006. Surface Complexation Modelling, Volume 11. Academic Press, Burlington. ISBN: 9780123725721

Lützenkirchen, J., Preocanin, T., Kovacevic, D., Tomisic, V., Lövgren, L., Kallay, N., 2012. Potentiometric titrations as a tool for surface charge determination. Croat. Chem. Acta 85, 391-417. dx.doi.org/10.5562/cca2062

Madejová, J., Komadel, P., 2001. Baseline studies of the clay minerals society source clays: infrared methods. Clays Clay Minerals, 49, 410-432. doi.org/10.1346/CCMN.2001.0490508

Marsac, R., Banik, N., Lützenkirchen, J., Diascorn, A., Bender, K., Marquardt, C., Geckeis, H., 2017. Sorption and redox speciation of plutonium at the illite surface under highly saline conditions. J. Colloids Interface Sci. 485, 59-64. doi.org/10.1016/j.jcis.2016.09.013

Martin Cabanas, N., Leclercq, S., Barboux, P., Fédoroff, M., Lefèvre, G., 2011. Sorption of nickel and cobalt ions onto cobalt and nickel ferrites. J. Colloids Interface Sci. 360, 695-700. doi.org/10.1016/j.jcis.2011.04.082

Marsch, G.P., Taylor, K.J., Bland, I.D., Westcott, C., Tasker, P.W., Sharland, S.M., 1985. Evaluation of the localized corrosion of carbon steel overpacks for nuclear waste disposal in granite environments. Mat. Res. Soc. Symp. Proc. 50, 421-428. doi.org/10.1557/PROC-50-421

McCafferty, E., 2010. *Introduction to Corrosion Science.* Springer-Verlag, New York, 2010. doi.org/10.1007/978-1-4419-0455-3

Millero, F.J.; Yao, W.; and Aicher, J., 1995. The Speciation of Fe(II) and Fe(III) in natural waters. Mar. Chem. 50, 21-39. doi.org/10.1016/0304-4203(95)00024-L

Missana, T., Garcia-Gutierrez M., Fernandez, V., 2003. Uranium (VI) sorption on colloidal magnetite under anoxic environment: experimental study and surface complexation modelling. Geochim. Cosmochim. Acta, 67, 2543-2550. doi.org/10.1016/S0016-7037(02)01350-9

Moog, H.C., Bok, F., Marquardt, C.M., Brendler, V., 2015. Disposal of nuclear waste in host rock formations featuring high-saline solutions – Implementation of a thermodynamic reference database (THEREDA). Applied Geochem. 55, 72-84. doi.org/10.1016/j.apgeochem.2014.12.016

Morelová, N. Steel corrosion and actinide sorption by iron corrosion products under saline conditions. PhD thesis, KIT, Karlsruhe.

Nakata, K., Nagasaki, S., Tanaka, S., Sakamoto, Y., Tanaka, T., Ogawa, H., 2002. Sorption and reduction of neptunium(V) on the surface of iron oxides. Radiochim. Acta 90, 665-669. doi.org/10.1524/ract.2002.90.9-11_2002.665

Naveau, A., Monteil-Rivera, F., Dumonceau, J., Boudesocque, S., 2005). Sorption of europium on a goethite surface: influence of background electrolyte. J. Contam. Hydrol. 77, 1-16. doi.org/10.1016/j.jconhyd.2004.10.002

Necib, S., Linard, Y., Crusset, D., Michau, N., Daumas, S., Burger, E., Romaine, A., Schlegel, M.L., 2016. Corrosion at the carbon steel-clay borehole water and gas interfaces at 85°C under anoxic and transient acidic conditions. Corr. Sci. 111, 242-258. dx.doi.org/10.1016/j.corsci.2016.04.039

Necib, S., Linard, Y., Crusset, D., Schlegel, M.L., Daumas, S., Michau, N., 2017. Corrosion processes of C-steel in long-term repository conditions. Corr. Engineer. Sci. Technol. 52, 127-130. doi.org/10.1080/1478422X.2017.1320155

Neck, V., Altmaier, M., Rabung, T., Lützenkirchen, J., Fanghänel, T., 2009). Thermodynamics of trivalent actinides and neodymium in NaCl, $MgCl_2$, and $CaCl_2$ solutions: Solubility, hydrolysis, and ternary Ca-M(III)-OH complexes. Pure Appl. Chem. 81, 1555-1568. doi.org/10.1351/PAC-CON-08-09-05

Nemer, M.B., Xiong, Y., Ismail, A.E., Jang, J.-H., 2011. Solubility of $Fe_2(OH)_3Cl$ (pure-iron end-member of hibbingite) in NaCl and Na_2SO_4 brines. Chem. Geol. 280, 26-32. doi.org/10.1016/j.chemgeo.2010.10.003

Olsson, C.-O.A., Landolt, D., 2003. Passive films on stainless steels-chemistry, structure and growth. Electrochim. Acta 48, 1093-1104. doi.org/10.1016/S0013-4686(02)00841-1

Parkhurst, D.L., Appelo, C.A.J., 1999. User's guide to PHREEQC (Version 2): A computer program for speciation, batch-reaction, one-dimensional transport, and inverse geochemical calculations. Water-Resources Investigations Report 99-4259, U.S. Geological Survey. doi.org/10.3133/wri994259

Payne, T.E., Brendler V., Ochs, M., Baeyens, B., Brown, P.L., Davies, J.A., Ekberg, C., Kulik, D.A., Lutzenkirchen, J., Missana, T., Tachi, Y., Van Loon, L.R., Altmann, S., 2013. Guidelines for thermodynamic sorption modelling in the context of radioactive waste disposal. Environ. Modell. Softw. 42, 143-156. dx.doi.org/10.1016/j.envsoft.2013.01.002

Pidchenko, I., Kvashnina, K.O., Yokosawa, T., Finck, N., Bahl, S., Schild, D., Polly, R., Bohnert, E., Rossberg, A., Göttlicher, J., Dardenne, K., Rothe, J., Schäfer, T., Geckeis, H.,

Vitova, T., 2017. Uranium redox transformations after U(VI) coprecipitation with magnetite nanoparticles. Environ. Sci. Technol. 51, 2217-2225. doi.org/10.1021/acs.est.6b04035

Pitzer, K.S., 1991. Ion Interaction Approach: Theory and Data Correlation (Chapter 3). In: Pitzer, K.S. (Ed.) Activity Coefficients in Electrolyte Solutions, CRC Press, Boca Raton, Florida. doi.org/10.1201/9781351069472

Pitzer, K.S., Mayorga, G., 1973. Thermodynamics of electrolytes. II. Activity and osmotic coefficients for strong electrolytes with one or both ions univalent. J. Phys. Chem. 77, 2300-2308. doi.org/10.1021/j100638a009

Plummer, L.N., Parkhurst, D.L., Fleming, G.W., Dunkle, S.A., 1988. A computer program incorporating Pitzer's equations for calculation of geochemical reactions in brines. Water-Ressources Investigations Reports 88-4153, U.S. Geological Survey, Reston, Virginia. doi.org/10.3133/wri884153

Polly, R., Finck, N., Platte, T., Morelová, N., Heberling, F., Schimmelpfennig, B., Geckeis, H., in preparation. First principle investigation of the incorporation of trivalent lanthanides an actinides in hydroxycarbonate and hydroxychloride green rust.

Pradhan, S.K., Bhuyan, P., Mandal, S., 2019. Influence of the individual microstructural features on pitting corrosion in type 304 austenitic stainless steel. Corros. Sci. 158, 108091. doi.org/10.1016/j.corsci.2019.108091

Ramya, S., Anita, T., Shaikh, H., Dayal, R.K., 2010. Laser Raman microscopic studies of passive films formed on type 316LN stainless steel during pitting in chloride solution. Corros. Sci. 52, 2114-2121. doi.org/10.1016/j.corsci.2010.02.028

Ravel, B., Newville, M., 2005. ATHENA, ARTEMIS, HEPHAESTUS: data analysis for X-ray absorption spectroscopy using IFEFFIT. J. Synchrotron Rad. 12, 537-541. doi.org/10.1107/S0909049505012719

Refait, P., Drissi, S.H., Pytkiewicz, J., Génin, J.-M., 1997. The anionic species competition in iron aqueous corrosion: Role of various green rust compounds. Corros. Sci. 39, 1699-1710. doi.org/10.1016/S0010-938X(97)00076-0

Refait, P., Abdelmoula, M., Génin, J.-M., 1998. Mechanisms of formation and structure of green rust one in aqueous corrosion of iron in the presence of chloride ions. Corros. Sci. 40, 1547-1560. doi.org/10.1016/S0010-938X(98)00066-3

Refait, P., Memet, J.-B., Bon, C., Sabot, R., Génin, J.-M., 2003. Formation of the Fe(II)-Fe(III) hydroxysulfate green rust during marine corrosion of steel. Corros. Sci. 45, 833-845. doi.org/10.1016/S0010-938X(02)00184-1

Réguer, S., Dillmann, P., Mirambet, F., Bellot-Gurlet, L., 2005. Local and structural characterization of chlorinated phases formed on ferrous archaeological artefacts by μXRD and μXANES. Nucl. Instrum. Methods Phys. Res., Sect. B 240, 500-504. doi.org/10.1016/j.nimb.2005.06.217

Réguer, S., Mirambet, F., Rémazeilles, C., Vantelon, D., Kergourlay, F., Neff, D., Dillmann, P., 2015. Iron corrosion in archaeological context: Structural refinement of the ferrous hydroxychloride β-$Fe_2(OH)_3Cl$. Corros. Sci. 100, 589-598. doi.org/10.1016/j.corsci.2015.08.035

Réguer, S., Mocuta, C., Thiaudière, D., Daudon, M., Bazin, D., 2016. Combination of X-ray synchrotron radiation techniques to gather information for clinicians. C. R. Chimie 19, 1424-1431. doi.org/10.1016/j.crci.2015.03.012

Rémazeilles, C., Refait, P., 2008. Formation, fast oxidation and thermodynamic data of Fe(II) hydroxychlorides. Corr. Sci. 50, 856-864. doi.org/10.1016/j.corsci.2007.08.017

Roberts, H.E., Morris, K., Mosselmans, F.J., Law, G.T.W., Shaw, S., 2019. Neptunium reactivity during co-precipitation and oxidation of Fe(II)/Fe(III) (oxyhydr)oxides. Geosciences 9, 27. doi.org/10.3390/geosciences9010027

Rojo, I., Seco, F., Rovira, M., Giménez, J., Cervantes, G., Martí, V., de Pablo, J., 2009. Thorium sorption onto magnetite and ferrihydrite in acidic conditions. J. Nucl. Mater. 385, 474-478. doi.org/10.1016/j.jnucmat.2008.12.014

Rothe, J., Butorin, S., Dardenne, K., Denecke, M.A., Kienzler, B., Löble, M., Metz, M., Seibert, A., Steppert, M., Vitova, T., Walther, C., Geckeis, H., 2012. The INE-Beamline for actinide science at ANKA. Rev. Sci. Instrum. 83, 043105. doi.org/10.1063/1.3700813

Roy, A.K., Fleming, D.L., Gordon, S.R., 1996. Effect of chloride concentration and pH on pitting corrosion of waste package container materials. University of North Texas Libraries, UNT Digital Library. https://digital.library.unt.edu/ark:/67531/metadc694820/

Rusch, B., Génin, J.-M., Ruby, C., Abdelmoula, M., Bonville, P., 2008. Ferrimagnetic properties in Fe^{II-III} (oxy)hydroxycarbonate green rusts. Solid State Sci. 40-49. doi.org/10.1016/j.solidstatesciences.2007.07.007

Sagoe-Crentsil, K.K., Glasser, F.P., 1993. “Green rust”, iron solubility and the role of chloride in the corrosion of steel at high pH. Cem. Concr. Res. 23, 785-791. doi.org/10.1016/0008-8846(93)90032-5

Schlegel, M.L., Bataillon, C., Benhamida, K., Blamc, C., Menut, D., Lacour, J.-L., 2008. Metal corrosion and argilite transformation at the water-saturated, high-temperature iron-clay interface: A microscopic-scale study. Appl. Geochem. 23, 2619-2633. doi.org/10.1016/j.apgeochem.2008.05.019

Schlegel, M.L., Bataillon, C., Blanc, C., Prêt, D., Foy, E., 2010. Anodic activation of iron corrosion in clay media under water-saturated conditions at 90°C: Characterization of the corrosion interface. Environ. Sci. Technol. 44, 1503-1508. doi.org/10.1021/es9021987

Schlegel, M.L., Necib, S., Daumas, S., Blanc, C., Foy, E., Trcera, N., Romaine, A., 2016. Microstructural characterization of carbon steel corrosion in clay borehole water under anoxic and transient acidic conditions. Corr. Sci. 109, 126-144. doi.org/10.1016/j.corsci.2016.03.022

Schlegel, M.L., Necib, S., Daumas, S., Labat, M., Blanc, C., Foy, E., Linard, Y., 2018. Corrosion at the carbon steel-clay borehole water interface under anoxic alkaline and fluctuating temperature conditions. Corr. Sci. 136, 70-90. doi.org/10.1016/j.corsci.2018.02.052

Schnurr, A., Marsac, R., Rabung, T., Lützenkirchen, J., Geckeis, H., 2015. Sorption of Cm(III) and Eu(III) onto clay minerals under saline conditions: Batch adsorption, laser-fluorescence spectroscopy and modeling. Geochim.. Cosmochim. Acta 151, 192-202. dx.doi.org/10.1016/j.gca.2014.11.011

Scholze, R., Amayri, S., Reich, T., 2019. Modeling the sorption of Np(V) on Na-montmorillonite – effects of pH, ionic strength and CO_2. Radiochim. Acta 107, 615-622. doi.org/10.1515/ract-2019-3109

Schramke, J.A., Santillan, E.F.U., Peake, R.T., 2020. Plutonium oxidation states in the Waste Isolation Pilot Plant repository. Applied Geochem. 116, 104561. doi.org/10.1016/j.apgeochem.2020.104561

Shoesmith, D.W., 2006. Assessing the corrosion performance of high-level nuclear waste containers. Corros., 62, 703-722. doi.org/10.5006/1.3278296

Shoesmith, D.W., King, F., 1999. The effects of gamma radiation on the corrosion of candidate materials for the fabrication of nuclear waste packages. Atomic Energy of Canada Limited, Technical Report, AECL-11999. www.osti.gov/etdeweb/servlets/purl/20070844

Singh, B.K., Jain, A., Kumar, S., Tomar, B.S., Tomar, R., Manchanda, V.K., Ramanathan, S., 2009. Role of magnetite and humic acid in radionuclide migration in the environment. J. Contam. Hydrol. 106, 144-149. doi.org/10.1016/j.jconhyd.2009.02.004

Skerencak-Frech, A., Fröhlich, D.R., Rothe, J., Dardenne, K., Panak, P.J., 2014. Combined time-resolved laser fluorescence spectroscopy and extended X-ray absorption fine structure spectroscopy on the complexation of trivalent actinides with chloride at T = 20-200°C. Inorg. Chem. 53, 1062-1069. doi.org/10.1021/ic4025603

Smailos, E., 1993. Corrosion of high-level waste packaging materials in disposal relevant brines. Nucl. Technol. 104, 343-350. doi.org/10.13182/NT93-A34895

Smailos, E., Fiehn, B., 1995. In-situ corrosion testing of selected HLW container materials under the conditions of the HLW test disposal in the Asse salt mine. Wissenschaftliche Berichte FZKA 5508, Forschungszentrum Karlsruhe GmbH, Karlsruhe.

Smailos, E., Schwarzkopf, W., Köster, R., 1987. Corrosion behaviour of container materials for the disposal of high-level waste forms in rock salt formations. Kernforschungszentrum Karlsruhe, KfK 4265. ISSN 0303-4003.

Soltis, J., 2015. Passivity breakdown, pit initiation and propagation of pits in metallic materials – Review. Corros. Sci. 90, 5-22. dx.doi.org/10.1016/j.corsci.2014.10.006

Song, Y., Jiang, G., Chen, Y., Zhao, P., Tian, Y., 2017. Effects of chloride ions on corrosion of ductile and carbon steel in soil environments. Sci. Rep. 7, 6865. doi.org/10.1038/s41598-017-07245-1

Stolica, N., 1969. Pitting corrosion on Fe-Cr alloys. Corros. Sci. 9, 205-216. doi.org/10.1016/S0010-938X(69)80051-X

Stumpf, S., Stumpf, T., Dardenne, K., Hennig, C., Foerstendorf, H., Klenze, R., Fanghänel, T., 2006. Sorption of Am(III) onto 6-line-ferrihydrite and its alteration products: Investigations by EXAFS. Environ. Sci. Technol. 40, 3522-3528. doi.org/10.1021/es052518e

Tholen, M., 2009. Chemisch-toxische Stoffe in einem Endlager für hochradioaktive Abfälle. Kurztitel: CHEMOTOX. APII – Inventar chemotoxischer Stoffe. DBE Technology GmbH, Peine. http://chemotox.oeko.info/dokumente/APII_Inventar.pdf

Tosca, N.J., Ahmed, I.A.M., Tutolo, B.M., Ashpitel, A., Hurowitz, J.A., 2018. Magnetite authigenesis and the warming of early Mars. Nature Geosci. 11, 635-639. doi.org/10.1038/s41561-018-0203-8

Usman, M., Byrne, J.M., Chaudhary, A., Orsetti, S., Hanna, K., Ruby, C., Kappler, A., Haderlein, S.B. (2018). Magnetite and green rust: Synthesis, properties, and environmental applications of mixed-valent iron minerals. Chem. Rev. 118, 3251-3304. doi.org/10.1021/acs.chemrev.7b00224

Van Isegehm, R., 2012. 26 - Corrosion issues of radioactive waste packages in geological disposal systems, pp 939-987. In: Feron, D. (Ed) *Nuclear Corrosion Science and Engineering*, Woodhead Publishing Series in Energy, 2012. ISBN 9781845697655

Vayssières, L., 1995. Précipitation en milieu aqueux de nanoparticules d'oxydes. Modélisation de l'interface et contrôle de la croissance. PhD thesis of the University Pierre et Marie Curie, Paris.

Vayssières, L., Chanéac, C., Tronc, E., Jolivet, J.-P., 1998. Size tailoring of magnetite particles formed by aqueous precipitation: An example of thermodynamic stability of nanometric oxide particles. J. Colloid Interface Sci. 205, 205-212. doi.org/10.1006/jcis.1998.5614

Vidojkovic, S.M., Rakin, M.P., 2017. Surface properties of magnetite in high temperature aqueous electrolyte solutions: A review. Adv. Colloid Interface Sci. 245, 108-129. doi.org/10.1016/j.cis.2016.08.008

Vilks, P., Yang, T., 2018. Sorption of selected radionuclides on sedimentary rocks in saline conditions - Updated sorption values. NWMO TR-2018-03, Nuclear Waste Management Organization, Toronto,

Wang, Z., Moore, R.C., Felmy, A.R., Mason, M.J., Kukkadapu, R.K., 2001. A study of the corrosion products of mild steel in high ionic strength brines. Waste Manage. 21, 335-341. doi.org/10.1016/S0956-053X(00)00058-1

Wang, G., Um, W., Kim, D.-S., Kruger, A.A. 2019. ^{99}Tc immobilization from off-gas waste streams using nickel-doped iron spinel. J. Hazard. Mater. 364, 69-77. doi.org/10.1016/j.jhazmat.2018.09.064

Westall, J.C., 1982. FITEQL: A Computer Program for Determination of Chemical Equilibrium Constants from Experimental Data, Version 2.0. Report 82-02, Department of Chemistry, Oregon State University, Corvallis.

Westerman, R.E., Pitman, S.G., 1984. Corrosion of candidate iron-based waste package structural barrier materials in moist salt environments. MRS Proceedings, 44, 279. doi.org/10.1557/PROC-44-279

Winterle, J., Ofeoegbu, G., Pabalan, R., Manepally, C., Mintz, T., Pearcy, E., Smart, K., McMurry, J., Pauline, R., Fedors, R., 2012. Geological disposal of high-level radioactive waste in salt formations. Report of the Center for Nuclear Waste Regulatory Analyses for the U.S. Nuclear Regulatory Commission. https://www.nrc.gov/docs/ML1206/ML12068A057.pdf

Wisniewska, M., Szewczuk-Karpisz, K., 2013. Removal possibilities of colloidal chromium (III) oxide from water using polyacrylic acid. Environ. Sci. Pollut. Res. 20, 3657-3669. doi.org/10.1007/s11356-012-1273-6

Yokosawa, T., Prestat, E., Polly, R., Bouby, M., Dardenne, K., Finck, N., Haigh, S.J., Denecke, M.A., Geckeis, H., 2019. Fate of Lu(III) sorbed on 2-line ferrihydrite at pH 5.7 and aged for 12 years at room temperature. II: Insights from STEM-EDXS and DFT calculations. Environ. Sci. Pollut Res. 26, 5282-8293. doi.org/10.1007/s11356-018-1904-7

Yuan, K., Renock, D., Ewing, R.C., Becker, U., 2015. Uranium reduction on magnetite: Probing for pentavalent uranium using electrochemical methods. Geochim. Cosmochim. Acta 156, 194-206. doi.org/10.1016/j.gca.2015.02.014

Zhang, B., Hao, S., Wu, J., Li, X., Li, C., Di, X., Huang Y., 2017. Direct evidence of passive film growth on 316 stainless steel in alkaline solution. Mater. Charact. 131, 168-174. dx.doi.org/10.1016/j.matchar.2017.05.013

Zhu, J., Xu, L., Lu, M., Zhang, L., Chang, W., 2015. Interaction effect between $Cr(OH)_3$ passive layer formation and inhibitor adsorption on 3Cr steel surface. RSC Adv. 5, 18518-18522. doi.org/10.1039/C4RA15519J

8. List of Figures

Figure 67. *Pourbaix diagrams corresponding to SGI corrosion experiments in 5 M NaCl at 90°C calculated with the [PI] database and the Pitzer approach. $SiO_{2,aq}$ activity obtained from weight loss, log a = -2.9 (A) and reduced $SiO_{2,aq}$ activity of log a = -3.5 (B).*

Figure 68. *Electron micrograph (left) of the corroded interface for SGI in contact with 5 M NaCl at 90°C for 31 weeks. Spots show location for EDX and µRaman analysis. Raman spectra (right) recorded at locations A and B.*

Figure 69. *Fe Kα intensity map (left) across the corroding interface for SGI contacted with 5 M NaCl for 31 weeks at 90°C. The map indicates the position of points of interest for probing the Fe K-edge by XAS (right). Black lines are experimental spectra, red lines are fit to experimental data using spectra recorded for the pristine steel, cronstedtite (cronst.) and iron hydroxychloride (Fe-Hc).*

Figure 70. *Electron micrographs (top), XPS 2p narrow line (lower left) and XRD pattern (lower right) for SGI contacted with 5 M NaCl for 49 weeks at 25°C. XRD analysis identified the presence of steel (PDF 87-0721) and chloride green rust (PDF 49-0095).*

Figure 71. *Electron micrographs (left, middle) and XRD pattern (right) for SGI contacted with 0.1 M NaCl for 28 weeks at 90°C. XRD analysis identified the presence of steel (PDF 87-0721), magnetite (PDF 88-0315) and cronstedtite (PDF 82-2238).*

Figure 72*. Electron micrographs for SGI contacted with Solution 3 at 90°C for 26 weeks (left), at 25°C for 20 weeks (middle) and at 25°C for 26 weeks (right).*

Figure 73. *Electron micrographs of SGI contacted with 3.4 M $MgCl_2$ at 90°C for 13 weeks (left), for 42 weeks (middle) and X-ray diffractograms (right) for samples after 13, 26 and 42 weeks of contact time. On diffractograms, PDF 34-0199 refers to iron hydroxychloride, the dotted green lines to amakinite.*

Figure 74. *Pourbaix diagrams corresponding to SGI corrosion experiments in 3.4 M $MgCl_2$ at 90°C calculated with the [PI] database and the Pitzer approach. Ferrous ion activities were taken from ICP-MS (log a = -3.65) and silica activities from weight loss ($SiO_{2,aq}$, log a = -1.87) (A). Diagram for higher iron (log a = 3) and lower Si (log a = -5) activities (B).*

Figure 75. *Electron micrograph (left) of the corroded interface for SGI in contact with 3.4 M $MgCl_2$ at 90°C for 31 weeks. Spots show location for EDX and µRaman analysis. Raman spectra (right) recorded at locations A, B and C.*

Figure 76. *Fe Kα intensity map (left) across the corroding interface for SGI contacted with 3.4 M $MgCl_2$ for 31 weeks at 90°C. The map indicates the position of points of interest for probing the Fe K-edge by XAS (right). Black lines are experimental spectra, red lines are fit to experimental data using spectra recorded for the pristine steel, wüstite (FeO) and iron hydroxychloride (Fe-Hc).*

Figure 77. *Electron micrograph (left) and X-rax diffractogram (right) for SGI contacted with 3.4 M $MgCl_2$ for 49 weeks at 25°C. On the diffractogram, PDF 87-0721 refers to the non-corroded steel surface and PDF 34-0199 to iron hydroxychloride.*

Figure 78. *pH_M (left) and E_h (right) evolutions for 309S corroded in different brines as a function of contact time.*

Figure 79. *Electron micrograph (left) and X-ray diffractogram (right) for 309S contacted with 5 M NaCl for 13 or 42 weeks at 90°C. On the diffractogram, vertical red bars refer to PDF 33-0397 corresponding to the non corroded steel.*

Figure 80. *Fe Kα intensity map (left) across the corroding interface for 309S contacted with 5 M NaCl for 31 weeks at 90°C. The map indicates the position of points of interest for probing the Fe K-edge by XAS (right). Black lines are experimental spectra, red lines are fits to experimental data using spectra recorded for the pristine steel, trevorite (trev., $NiFe_2O_4$) and chloride green rust (GR).*

Figure 81. *Ni Kα intensity map (left) across the corroding interface for 309S contacted with 5 M NaCl for 31 weeks at 90°C. The map indicates the position of points of interest for probing the Ni K-edge by XAS (right). Black lines are experimental spectra, red lines are fits to experimental data using spectra recorded for the pristine steel, trevorite (trev., $NiFe_2O_4$) and Ni-doped chloride green rust (GR).*

Figure 82. *Cr Kα intensity map (left) across the corroding interface for 309S contacted with 5 M NaCl for 31 weeks at 90°C. The map indicates the position of points of interest for probing the Cr K-edge by XAS (right). Black lines are experimental spectra, red lines are fits to experimental data using spectra recorded for the pristine steel, $Cr(OH)_3$ and Cr_2O_3.*

Figure 83. *Pourbaix diagrams for 309S contacting 5 M NaCl at 90°C drawn with respect to Fe (left), Ni (middle) and Cr (right) using amounts of dissolved elements after 26 weeks, the SIT approach and the [TC] database.*

Figure 84. *Experimental (symbols) and modeled (lines) surface charge of magnetite in 0.1 M NaCl and 1.0 M NaCl. Fit results are shown in Table 11.*

Figure 85. *Uptake of Eu (left: 5.1×10^{-10} M; right: 1×10^{-5} M) by magnetite (m/V = 0.5 g/L) as a function of pH_M at different NaCl ionic strengths under anoxic and room temperature conditions.*

Figure 86. *Uptake of Eu (1×10^{-5} M) by magnetite (m/V = 0.5 g/L) as a function of pH_M at different $MgCl_2$ ionic strengths under anoxic and room temperature conditions.*

Figure 87. *Dissolved iron contents during Eu sorption experiments to magnetite in NaCl (left) and in $MgCl_2$ (right) solutions.*

Figure 88. *Sorption isotherms of Eu to magnetite (0.5 g/L) at pH_M ~6 and pH_M ~7 at various ionic strengths set by NaCl.*

Figure 89. *Experimental (solid black lines) and modeled (red dashed lines) Am L_3-edge EXAFS data of the sorption samples at various pH_M and NaCl concentrations, and of the Am^{3+} aqueous ions (left), with the corresponding Fourier transforms (right).*

Figure 90. *pH_M dependent Eu sorption (left: [Eu] = 5.1×10^{-10} M; right: [Eu] = 1×10^{-5} M)) onto magnetite at various ionic strengths. Experimental (symbols) and modelled (solid lines) data obtained using surface complexation model in FITEQL with the Pitzer approach and [TPA]. The distribution of the three complexes are represented by red (I = 0.96 M) and blue (I = 4.8 M) dashed lines. (Singh et al. [2009]; Cat. et al.: [Catalette et al. 1998]).*

Figure 91. *Sorption isotherms of Eu onto magnetite at pH_M ~6.0 (left) and at pH_M ~7.0 (right) at various ionic strengths. Experimental (symbols) and modelled (solid lines) data using surface complexation model in FITEQL with the Pitzer approach and [TPA] database.*

Figure 92. *Europium uptake (left: [Eu] = 5.1×10^{-10} M; right: [Eu] = 1×10^{-7} M) by iron hydroxychloride (m/V = 1 g/L) at different ionic strengths of NaCl.*

Figure 93. *Europium uptake (left: [Eu] = 5.1×10^{-10} M; right: [Eu] = 1×10^{-7} M) by iron hydroxychloride (m/V = 1 g/L) at different ionic strengths of $MgCl_2$.*

Figure 94. *Europium sorption (left: [Eu] = 5.1×10^{-10} M; right: [Eu] = 1×10^{-7} M) to chloride green rust (m/V = 1 g/L) at various ionic strengths of NaCl.*

Figure 95. *Experimental (symbols) and modeled (solid lines) pH_M dependent charging behavior of trevorite at two ionic strengths of NaCl. Numerical values are shown in Table 14.*

Figure 96. *Europium sorption (left: [Eu] = 5.1×10^{-10} M; right: [Eu] = 1×10^{-5} M) to trevorite (m/V = 0.08 g/L) at various ionic strengths of NaCl.*

Figure 97. *Experimental (symbols) and modelled (solid lines) pH_M dependent Eu sorption ([Eu] = 1×10^{-5} M) onto trevorite at various ionic strengths. Modeling was performed using surface complexation model in FITEQL with the Pitzer approach and [TPA] database. The distribution of two complexes are represented by black (I = 0.1 M) and blue (I = 4.8 M) dashed/dotted lines, the contribution of S_1 is too ow to be visible on the figure.*

Figure 98. *Experimental (symbols) and modeled (solid lines) pH_M dependent charging behavior of chromium oxide at two ionic strengths of NaCl. Numerical values are shown in Table 16.*

Figure 99. *Europium sorption (left: [Eu] = 5.1×10^{-10} M; right: [Eu] = 1×10^{-5} M) to chromium oxide (m/V = 1.0 g/L) at various ionic strengths of NaCl.*

Figure 100. *Experimental (symbols) and modelled (solid lines) pH_M dependent Eu sorption ([Eu] = 1×10^{-5} M) onto chromium oxide at various ionic strengths. Modeling was performed using surface complexation model in FITEQL with the Pitzer approach and [TPA] database. The distribution of the complexes are represented by dashed/dotted lines for I = 0.1 M.*

Figure 101. *X-ray diffractograms of samples of the WRX and WREuX series at day 1, and patterns of reference compounds from the PDF-2 database. (Fe-Hc: iron hydroxychloride).*

Figure 102. *X-ray diffractograms of samples WREuX at day 1 and at day 7, patterns of reference compounds from the PDF-2 database. (Fe-Hc: iron hydroxychloride, M: magnetite)*

Figure 103. *X-ray diffractograms of samples MgEuX at day 1 and of magnetite synthesized without Eu and without added salt, patterns of reference compounds from the PDF-2 database.*

Figure 104. *U(V) incorporated into an octahedral site of magnetite as optimized by DFT. O atoms are red, Fe atoms are brown and the U atom is blue.*

Figure 105. *Pictures showing the evolution of steel (top: SGI, bottom: 309S) in contact with bentonite after 1 month (left), 2 months (middle) and 6 months (right).*

Figure 106*. X-ray diffractograms of the starting (raw) MX-80 bentonite and after 1, 2 and 6 months of contact time with SGI at 65°C under anoxic conditions. Basal spacings are indicated, lattice planes of montmorillonite are indexed and various admixed phases are identified.*

Figure 107. *X-ray diffractograms of the starting (raw) MX-80 bentonite and after 1, 2 and 6 months of contact time with 309S at 65°C under anoxic conditions. Basal spacings are indicated, lattice planes of montmorillonite are indexed and various admixed phases are identified.*

Figure 108*. FTIR spectra of the raw MX-80 bentonite (black), the bentonite contacting SGI (red) and 309S (blue) for 6 months. Inset show the hydroxyl stretching region.*

Figure 109*. Electron micrographs of SGI coupons contacting bentonite for 1 (left), 2 (middle) and 6 months (right) at two magnifications.*

Figure 110. *Fe $2p_{3/2}$ (left) and O 1s (middle) X-ray photoelectron spectra recorded for SGI coupons and Cr $2p_{3/2}$ spectra (right) recorded for 309S coupons after 1, 2 and 6 months of contact time with bentonite.*

List of Tables

9. Veröffentlichungen

Veröffentlichungen in wissenschaftlichen (peer-reviewed) Zeitschriften

(1) Morelová, N., Finck, N., Lützenkirchen, J., Schild, D., Dardenne, K., Geckeis, H., 2020. Sorption of americium/europium onto magnetite under saline conditions: Batch experiments, surface complexation modelling and X-ray absorption spectroscopy study. J. Colloid Interface Sci. 561, 708-718 (doi.org/10.1016/j.jcis.2019.11.047).

Weiterhin sind folgende Publikationen in Vorbereitung

(2) Morelová, N., Finck, N., Schlegel, M., Schild, D., Geckeis, H., Corrosion of ductile iron under saline and elevated conditions temperature. In Preparation for submission in 2021.

(3) Polly, R., Finck, N., Platte, T., Morelová, N., Heberling, F., Schimmelpfennig, B., Geckeis, H., First principle investigation of the incorporation of trivalent lanthanides and actinides in hydroxycarbonate and hydroxychloride green rust. In Preparation for submission in 2021.

(4) Finck, N., Morelová, N., Schlegel, M.L., Schild, D., Geckeis, H., Corrosion of stainless steel under anoxic, high saline and elevated temperature conditions. In Preparation for submission in 2021.

Sonstige Veröffentlichungen und Publikationen

(1) Morelová, N., Doktorarbeit zu „Steel corrosion and actinide sorption by iron corrosion products under saline conditions“, Karlsruhe Institut für Technologie, 2020.

Vorträge bei wissenschaftlichen Konferenzen und Workshops

(1) Vozarová, N., et al. „Sorption of Eu(III) and Am(III) on magnetite in NaCl brines". Goldschmidt Conference, 12-17 August 2018, Boston, MA (USA).
(2) Polly, R., et al. „Incorporation of radionuclides in green rust". 4th International Workshop on Advanced Techniques in Actinides Spectroscopy (ATAS), 06-09 November 2018, Nice (France).
(3) Finck, N., et al. (Invited oral presentation) "Steel corrosion and actinides retention by Fe-corrosion phases under anaerobic saline conditions". 7th Workshop of the BMWi joint project GRaZ, 9-10 April 2019, Saarbrucken (Germany).
(4) Morelová, N., et al. "Studies on Fe corrosion in brine systems". ABC-Salt (VI) Workshop on Actinide-Brine-Chemistry, 25-26 June 2019, Karlsruhe (Germany).
(5) Vozarová, N., et al. "Corrosion of ductile iron under saline and elevated temperature conditions". EuroCorr 2019, 9-13 September 2019, Sevilla (Spain).
(6) Finck, N., et al. "Stainless steel corrosion under anaerobic, highly saline and elevated temperature conditions". 7th international workshop on long-term prediction of corrosion damage in nuclear waste repositories, 19-21 November 2019, Nancy (France).
(7) Cakir-Wuttke, P., Finck, N. "Electrochemical investigations of steel corrosion under saline media". EuroCorr 2020, September 6-10 2020, Brussels (Belgium).

Poster bei wissenschaftlichen Konferenzen und Workshops

(1) Polly, R., et al. „Incorporation of radionuclides in green rust". STC 2018 - 54th Symposium on Theoretical Chemistry, 17-20 September 2018, Halle (Germany).
(2) Polly, R., et al. "Incorporation of radionuclides in hydroxycarbonate and hydroxychloride green rust". 10th Triennial Congress of the International Society for Theoretical Chemical Physics (ISTCP 2019), 11-17 July 2019, Tromso (Norway).
(3) Polly, R., et al. "Density Functional Theory study on the incorporation of radionuclides in hydroxycarbonate and hydroxychloride green rust". 17th International Conference on the Chemistry and Migration Behavior of Actinides and Fission Products in the Geosphere, 15-20 September 2019, Kyoto (Japan).

INE Scientific Working Documents
ISSN 2701-262X

www.kit.edu